# Multi-Degree-of-Freedom Electromagnetic Actuator Implemented as a Spinal Segment


Sigrid Aadnesgaard

Dissertation submitted for the degree of
Master of Science in Electrical Engineering
Faculty of Engineering and the Built Environment
Department of Electrical Engineering
University of Cape Town

**November 14, 2025**

# Declaration

1. I know the meaning of plagiarism and declare that all the work in the document, save for that which is properly acknowledged, is my own. This dissertation has been submitted to the Turnitin module and I confirm that my supervisor has seen my report and any concerns revealed by such have been resolved with my supervisor.
2. I know that plagiarism is wrong. Plagiarism is to use another's work and pretend that it is one's own.
3. I have used the IEEE convention for citation and referencing. Each contribution to, and quotation in, this report from the work(s) of other people has been attributed, and has been cited and referenced.
4. This report is my own work.
5. I have not allowed, and will not allow, anyone to copy my work with the intention of passing it off as their own work or part thereof.

Signature: Signed by candidate

Sigrid Aadnesgaard

**November 14, 2025**

# Acknowledgments

Gogo, thank you for gifting me our incredible family. Everything I do and achieve is owed to you. Uzohlala njalo usezinhliziyweni zethu. I would also like to thank my supervisor, Sampath Jayalath, who has inspired and encourage my engineering journey.

# Abstract

Quadruped and humanoid robots are increasingly integrated into daily life, contributing to applications ranging from hazardous exploration to manufacturing and domestic assistance. While advancements in agility, efficiency, and adaptability have been achieved, the flexibility of robotic spines remains a significant limitation. The inclusion of flexibility in robotic spines is a feature that is often overlooked, resulting in robots with rigid structures, limited degrees of freedom (DOF), and complex control mechanisms. Traditional actuation methods in quadruped and humanoid spines rely on bulky, redundant systems with multiple motors and tendons, where actuator design and optimisation are rarely prioritised. This thesis explores multi-degree-of-freedom (MDOF) actuators, focusing on their application in an electromagnetic spinal segment. Electromagnetic actuators offer a promising alternative to traditional actuators as they enable bidirectional movement directly on the end effector, reducing the number of required actuators and removing the need for wires and tendons. A novel Double Helix (DH) actuator is proposed to facilitate MDOFs from a single structure. Despite the DH achieving two DOFs, its integration into a spinal actuator was replaced by a linear solenoid electromagnetic plunger that offers a quick response, high force, ease of control, and configurable stroke lengths. This thesis details the design and optimisation methodology for the linear solenoid plunger, highlighting its potential for more efficient actuation. The system achieves enhanced stability and increased DOF by combining the linear actuators into a parallel configuration. The resulting spinal segment is a compliant six-legged parallel actuator capable of six DOF. The parallel system demonstrates its feasibility and potential for enhancing robotic movement by reducing actuators and tendons, improving flexibility and eliminating complex control methods. The thesis highlights the importance of the design methodology of electromagnetic robots and robots alike, reducing their complexity and improving their adaptability and modularity. The resulting structure achieves six DOF in the form of a parallel manipulator, with potential applications as a spinal segment in both quadruped and humanoid robots.

Video Abstract


Table 1: Implemented EM actuator Movement compared to MATLAB Simulink Model

| **Movement** | **Implemented** | **MATLAB** |
|---|---|---|
| Vertical Translation | Vertical Translation1,Translation2 | Vertical Translation1,Translation2 |
| Lateral Bending | Bending, Bending2 | Bending |
| Flexion/Extension | Extension/Flexion | Extension |
| Rotation | Rotation1, Rotation2 | Rotation |
| Bending & Rotation | Rotation & Lateral Bending | Rotation & Lateral Bending |
| Lateral Translation | Lateral Translation1 , Lateral Translation2 | Lateral Translation |
| Complex Movement | Multiple Sequenced Movements. | Multiple Sequenced Movements |
| Prototype 1 | The First Prototype | - |

# Contents

**List of Figures** vii

**List of Tables** x

**1 Introduction** 1
- 1.1 Background and Context . . . 1
- 1.2 Problem Statement and Research Questions . . . 2
- 1.3 Scope and Objectives . . . 3
- 1.4 Achievements and Research Contribution . . . 4
- 1.5 Overview of Dissertation . . . 5

**2 Literature Review: Actuators and Spinal Manipulators** 6
- 2.1 Introduction to Robotic Actuators . . . 6
- 2.2 Bio-inspired Robotic Design . . . 7
- 2.3 The Spinal Structure of Humans and Animals . . . 8
- 2.4 Spinal Actuation in Robots . . . 9
- 2.5 Quadruped Spinal Motion . . . 9
  - 2.5.1 Quadruped Robots: State of the Art . . . 10
- 2.6 Humanoid Robots . . . 12
  - 2.6.1 Actuator Types and DOF in Humanoid Spines . . . 14
  - 2.6.2 Range of Motion (ROM) of Humanoid Spines . . . 16
  - 2.6.3 Design and Modeling of Humanoid Spines . . . 17
  - 2.6.4 Control of Humanoid Spines . . . 17
- 2.7 Conclusion . . . 18

**3 Linear Actuator Design Review** 19
- 3.1 Actuation Methods . . . 19
  - 3.1.1 Electromagnetic Linear Actuation . . . 20
- 3.2 Design and Optimisation . . . 20
  - 3.2.1 Effect of Temperature . . . 21
- 3.3 Design Considerations . . . 22
  - 3.3.1 Magnetic Materials . . . 23
  - 3.3.2 Electromagnetic Forces . . . 23
- 3.4 Conclusion . . . 24

**4 Double Helix-Based Actuator for 2-Degree-of-Freedom Motion** 25
- 4.1 Introduction . . . 25
- 4.2 Double Helix Actuator Design . . . 27

4.2.1 Geometry . . . 27
4.2.2 Magnetic field . . . 28
4.2.3 Actuator Design . . . 28
4.3 Simulation of DH Actuator . . . 29
4.3.1 Magnetic Field Simulations . . . 30
4.3.2 Forces . . . 31
4.4 Optimisation and Simulation Results . . . 32
4.4.1 Sensitivity Analysis . . . 32
4.4.2 Optimisation . . . 32
4.5 Implementation and Experimental Results . . . 33
4.5.1 Force Measurement Experimental Setup . . . 33
4.5.2 Thermal Analysis . . . 35
4.6 Discussion and Conclusion . . . 36

**5 Linear Electromagnetic Actuator: Solenoid Plunger 38**
5.1 Design and Optimisation of a Solenoid Plunger . . . 38
5.1.1 S1-3: Mechanical Design . . . 40
5.2 S4: Analysis of Electromagnetic Force . . . 41
5.2.1 Theoretical Analysis . . . 41
5.2.2 S4: FEA Analysis . . . 44
5.3 S5: Variable Selection . . . 45
5.3.1 Solenoid Coils . . . 45
5.3.2 Magnet Plunger . . . 46
5.4 Optimisation Simulation Results . . . 47
5.4.1 S6: Sensitivity Analysis . . . 47
5.4.2 S7: Optimisation Analysis . . . 49
5.4.3 S8: Thermal Simulations . . . 52
5.5 S9-S10: Design Comparison and Selection . . . 52
5.6 S11: Solenoid-Plunger Implementation and Experimental Results . . . 54
5.6.1 Power Circuit . . . 55
5.7 System Testing . . . 56
5.7.1 Heat Generated . . . 56
5.7.2 Force . . . 59
5.7.3 Weight . . . 61
5.8 LEMA: Solenoid Plunger Conclusion . . . 61

**6 Electromagnetic (EM) Spinal Segment Actuator 62**
6.1 6 DOF Parallel Actuators . . . 62
6.2 EM Spinal Segment Actuator Design . . . 64
6.2.1 Structural Design . . . 65
6.3 System Dynamic Equation . . . 67
6.3.1 Actuator Leg Position an Angle . . . 69
6.4 EM Spinal Segment Implementation and Testing . . . 72
6.5 Results: Platform Movement . . . 72

6.5.1 Rotation Results . . . 73
6.5.2 Lateral Bending (Tilt) Results . . . 74
6.5.3 6 Degree-of-Freedom (DOF) Results . . . 74
6.6 Matlab-Simulink Simulation and Closed-Loop Control . . . 77
6.6.1 MATLAB-Simulink Simulations . . . 80
6.6.2 Lateral Bending . . . 81
6.6.3 Flexion/Extension . . . 82
6.6.4 Rotational Movement . . . 83
6.6.5 Lateral Translation . . . 84
6.7 Conclusion . . . 85
6.8 Commercial Comparison . . . 87

**7 Conclusions, Research Contributions and Future Recommendations 88**

**Bibliography 92**

**A Appendix: Matlab Code 101**

**B Appendix: AWG Table 104**

**C Appendix: Arduino Code for Platform Movement 105**

**D Appendix: Inverse Dynamic Modelling of 6 DOF parallel actuator 110**

**E Ethics Approval 115**

**F AI Contributions 116**

# List of Figures


2.1 Spinal Movement . . . 8
2.2 6 DOF: rotation and translation of a single vertebra (image adapted [1]) . . . 8
2.3 (a) MIT Cheetah. (b) Kitty. (c) Fanari. (d) Bobcat. (e) Renny. (f) Cheetah-Cub-S. (g) Quasi-Quadruped. (h) Salamander. (i) Nekobot. . . . 11
2.4 Summary of Humanoid and Spine Robot Images . . . 14

3.1 The relationship between the conductivity of copper and temperature [2] . . . 22

4.1 The DH coil structure: (a) The outer tightly wound coil tilted at an angle $\phi$, and (b) the inner coil oppositely tilted at $-\phi$. $I_o$ in (a) and $I_i$ in (b) represent the current in the inner and outer coil, respectively. . . . 27
4.2 The DH coil structure: (a) Rectangular Coil (b) Elliptical Coil . . . 29
4.3 The DH coil Parameter Diagram . . . 29
4.4 Magnetic fields of the elliptical and rectangular coil with and without a steel core . . . 31
4.5 Force per Magnet Distance at Various Tilt Angles for Rectangular and Elliptical Coil Shapes . . . 31
4.6 DH Pareto Plot: Optimised Designs . . . 33
4.7 DH Practical Setup with Dual Range Force Sensor . . . 33
4.8 60° and 45° DH measured (M) and simulated (S) force comparison . . . 34
4.9 Thermal analysis results from thermal camera separately (TCS), simulation separately (SS) and thermal camera together (TCT) and simulations together (ST). The range of temperatures for each row is indicated by the thermal colour bar. . . . 35
4.10 Temperature and Resistance of the Inner and Outer coil. . . . 36

5.1 EM Actuator Design Methodology . . . 40
5.2 Single Solenoid Design: 1 - PLA Connector, 2 - Steel Universal Joint, 3 - Steel Nut - 4 - Magnet, 5 - PLA Bobbin, 6 - Copper Solenoid . . . 41
5.3 Solenoid Plunger and Magnetic Field Diagram: 1 - Magnet, 2 - Solenoid, 3 - PLA Magnet Stopper, 4 - PLA Bobbin . . . 42
5.4 Solenoid-Plunger Simulation Diagram and Magnetic Field . . . 44
5.5 Declared Variables Diagram . . . 45
5.6 Force over Air Gap increase . . . 46
5.7 Force per Magnet Length and Position . . . 47
5.8 Sensitivity Results . . . 48
5.9 Optimisation Methodology Flowchart . . . 49
5.10 Pareto Optimisation Results. Figure Titles: Objective Pareto Plot. Figure x-axis title: Objective Magnetic Force Y Direction. Figure y axis labels: Objective Volume of Copper Cylinders . . . 50

5.11 Optimised Solenoid Plunger Simulation Visual . . . 51
5.12 Thermal Analysis . . . 52
5.13 Design Comparison . . . 53
5.14 Pareto Plot Solution for 0.6mm Wire . . . 54
5.15 Solenoid-Plunger Implementation . . . 55
5.16 Driving Circuit for a Pair of Solenoid Plungers . . . 56
5.17 Thermal Imager and Icepak Thermal Images . . . 57
5.18 Measure and Simulated Thermal Results . . . 58
5.19 Force Testing Experimental Setup . . . 59
5.20 Force Over Magnet Stroke: 0.92 A . . . 59
5.21 Force over Magnet Stroke: 1.4 A . . . 60
5.22 Force Over Magnet Stroke: 1.8 A . . . 60
5.23 Force Over Magnet Stroke: 2 A . . . 60

6.1 Joint Types [3] . . . 63
6.2 UPU parallel System [4] . . . 63
6.3 6 DOF Stewart Platforms: (a) Piezoelectric, (b) Pneumatic, (c) Hydraulic. . . . 64
6.4 Assembly Drawing . . . 65
6.5 Plunger Extension and Plate Rotation . . . 66
6.6 Top View of Solenoid Extension and Plate Rotation . . . 66
6.7 Connector adjustments . . . 67
6.8 Free Body Diagram: Full Version . . . 68
6.9 Free Body Diagram: Simplified Version . . . 68
6.10 Horizontal and Vertical Displacement of the Platform at Different Solenoid-Plunger Angles 71
6.11 Rotational Angle and Tilt Angle of the Platform at Different Solenoid-Plunger Angles 71
6.12 Driving Circuit for a Pair of Solenoid Plungers . . . 72
6.13 Rotational Actuation Numbered Diagram: Solenoids 1 to 6. . . . 73
6.14 Measured and Analytical Results for Rotation of the Top Plate . . . 73
6.15 Measured and Analytical Results for the Bending of the Top Plate in 3 DOF . . . 74
6.16 Images of various states of the robot: (a) Resting; (b) CW; (c) CCW; (d)Vertical Translation; (e) CW Superposition; (f) CCW Superposition. . . . 75
6.17 Images of various states of the robot: (a) Tilt A: Bending; (b) Tilt B:Bending ; (c) Tilt C: Flexion/Extension; (d) Lateral Translation 1; (e) Lateral Translation 2 . . . 76
6.18 Simulink Platform . . . 78
6.19 Inverse Kinematics and Dynamics . . . 78
6.20 PID Controller . . . 79
6.21 Vertical Translation Step Response . . . 79
6.22 Z_displacement of the Top Platform . . . 80
6.23 Force Corresponding to the Z_displacement for Each Leg . . . 80
6.24 Leg Position Error . . . 81
6.25 Lateral Bending Force per Leg Over Time . . . 82
6.26 Lateral Bending Leg Position Over Time . . . 82
6.27 Flexion/Extension Force per Leg Over Time . . . 83
6.28 Flexion/Extension Leg Position Over Time . . . 83

6.29 CW and CCW Force per Leg Over Time . . . . . 84
6.30 CW and CCW Leg Position Over Time . . . . . 84
6.31 Lateral Translation Force Per Leg Over Time . . . . . 85
6.32 Lateral Translation Leg Position Over Time . . . . . 85

A.1 Platform Dynamics Matlab Code . . . . . 102

B.1 AWG Table . . . . . 104

D.1 (a) Two Euler angles of the limb (b) Free body diagram of a typical limb [5] . . . . . 111

# List of Tables


1 Implemented EM actuator Movement compared to MATLAB Simulink Model . . . . . iii

2.1 ROM of the Thoracic and Lumbar Spine [1] . . . . . 9
2.2 Summary of Quadruped Robots . . . . . 10
2.3 Summary of Humanoid and Spine Robots . . . . . 13
2.4 Summary of Humanoid Spine ROM . . . . . 16

3.1 Actuation Method Comparison . . . . . 19
3.2 Magnet Property Comparison [6] . . . . . 23

4.1 Magnetic Actuation Base and Systems . . . . . 25
4.2 Magnetic Field Distribution . . . . . 27
4.3 Variable Specifications and Optimizations . . . . . 30
4.4 Sensitivity Analysis Results . . . . . 32

5.1 Declared Variables . . . . . 45
5.2 Simulation Variable Ranges . . . . . 48
5.3 Top 10 Optimal Configurations . . . . . 50
5.4 Design Placement per Category and Final Position . . . . . 53
5.5 Coil Temperature Measurements . . . . . 57
5.6 Mass of System Element . . . . . 61

6.1 Vertical and Horizontal, Rotational and Tilt Displacement of the Top Platform . . . . 70
6.2 Implemented EM actuator Movement compared to MATLAB Simulink Model . . . . . 86
6.3 Comparison of Custom Solenoid Plunger with Commercial Linear Actuators . . . . . 87

# Chapter 1

# Introduction

## 1.1 Background and Context

Robots have been designed to perform complex and precise tasks to meet the increasing demand for productivity and efficiency in fields such as automation, manufacturing, agriculture and interactive services [7]. These robots' significant role requires accuracy, adaptability, safety and reliability [8]. Among these robots, humanoids and quadrupeds stand out as they begin to integrate with and replace the human workforce [4] [9] [7]. To meet the requirements of these roles, robots need to achieve the versatility and range of motion seen in humans [10] [9]. However, this is accompanied by complexities in control and actuator dynamics [8]. Due to the intricacies of mimicking human motion, many quadruped and humanoid robots suffer from limited versatility due to constraints in their degrees of freedom (DOF) and the complexities involved in controlling these movements [11] [12]. The key component enabling and restricting the movement of these robots is the spine [4]. The spine is identified as the engine for motion and is responsible for the smooth, agile and adaptive movement seen in humans and animals [13]. However, many of the robots designed do not incorporate a flexible spine, which limits the robot's movement and application environment [7]. In most humanoids and quadrupeds, the leg actuation dominates their movement, with the spine modelled as a rigid or passive element [14] [12]. However, in recent years, researchers have focused on a flexible spine's contribution and noted improvements in energy efficiency, range of motion, and fluidity, highlighting the benefits of its inclusion [15]. From this, the spine is identified as a crucial element within these robots that enables and restricts movement and control. Therefore, robotic spines' design becomes an optimisation between increasing degrees of freedom and reducing the complexity of its control.

Other than the spine, the robot's actuation is another aspect which enables their movement and differentiates designs from one another [15]. Most are actuated and controlled by motors that pull tendons to coordinate movement; these motors are limited to a single directional one DOF, necessitating two motors per DOF [12] [7] [16]. While effective in achieving the desired movement in robotic spines, the motors limited DOF drastically increases the number of actuators required for these movements, subsequently adding weight and complexity to the system [8] [17]. Increasing actuators requires precise control algorithms to ensure cohesiveness, often resulting in bulky systems designed to achieve specific movements [11].

Additionally, the configuration of the actuators within humanoid and quadruped robots contributes to the design complexities [4]. The actuators are typically arranged in serial, parallel or hybrid structures. Despite serial structures offering a wide range of motion and simplicity, parallel and hybrid structures outperform the serial designs due to their high stiffness and accurate positioning, which are desirable

in robotic spines [18].

From the drawbacks and limitations of actuators currently used in spinal robots, electromagnetism is identified as a promising alternative [15] [19]. Electromagnetic actuators, such as solenoids, have the ability to control movement in two directions and create displacement directly on the end effector, removing the need for tendons or wires [20] [19] [21]. Reducing the number of actuators in the system and simplifying the complexity of the control whilst maintaining the available DOF would ensure a highly functional and implementable robotic spine [22].

The following characteristics have been identified as crucial design elements and requirements for effective and efficient spinal robots:

1. System capable of a minimum of 6 DOF
2. Capable of segment Control
3. Optimised force-to-weight ratio
4. Thermal management
5. Adjustable and Replaceable
6. Simple control

By analysing current robotic spines' advantages and disadvantages and drawing inspiration from nature, an electromagnetic spinal manipulator capable of implementation as a spinal segment is investigated.

## 1.2 Problem Statement and Research Questions

In literature, the design of robotic spines focuses on achieving specific movements that isolate the system's implementation [22]. Further, many of the systems designed are bulky and complex, requiring complex additional components and immense computing power [22]. As shown in Table 2.2 and Table 2.3, which summarise some existing designs of quadruped and humanoid robots, each segment of the spine has a maximum of 3 DOF and relies on interlinked segments to realise a greater range of motion. Within the design of the spinal systems, the actuator controlling the movement is typically not optimised; instead, existing actuators are selected and used [22]. The lack of actuator and configuration optimisation leads to movement and system adaptability inefficiencies [7] [23].

The literature further highlights the absence of electromagnetism as a form of actuation in spinal robots. Electromagnetism has the potential to simplify the design of spinal robots and, therefore, overcome some limitations associated with other actuators. The optimisation of the individual actuator would lead to a highly functional design, resulting in a system with high performance, space conservation and low power and control requirements [23] [22].

From this, the research questions answered in this thesis are:

1. What are the features, advantages and disadvantages of various quadruped and humanoid spinal designs proposed in the literature?
2. What role does the spine play in enabling movement in robots?

3. How has biology influenced the design of spinal robots, and what characteristics of natural spines have been successfully mimicked?
4. What are the key factors ensuring high performance in a spinal system?
5. Is electromagnetism a beneficial method of actuating spinal robots?
6. What are the factors influencing the operation of an electromagnetic actuator?
7. What role does optimisation play in the performance of an electromagnetic system?
8. What actuator configuration is most suitable for spinal designs?

## 1.3 Scope and Objectives

In the field of humanoid development, a wide variety of actuation methods successfully reproduce the movement of the mimicked creature [15] [24]. Most of these require complex and expensive equipment, restricting them to controlled settings. Electromagnetism provides solutions to these limitations. Therefore, this study's objective is to utilise electromagnetism's adaptability to achieve multiple degrees of freedom with simplicity and efficiency. While investigating the advantages and disadvantages associated with other forms of actuation.

The main problems investigated throughout the thesis are the factors influencing the system's DOF, with a focus on actuation. To optimise the actuator, the magnetic field, the actuation force, and the robot's weight are identified as critical design considerations. Further, the project highlights the complications of excitation, actuator configuration, and the limitations of existing designs.

This thesis aims to explore the use of electromagnetic actuation in developing a 6 DOF actuator capable of implementation as a segment in spinal robots. Further, it seeks to use animal spines' evolutionary characteristics as inspiration and electromagnetism's benefits to develop a system capable of spinal-like movement.

The following was conducted to meet the objectives elaborated on above:

1. Literature review on current spinal actuators in both humanoid and quadruped robots.
2. Investigation of suitable electromagnetic actuators.
3. Design of FEA simulation to characterise the behaviour of electromagnetic actuation within the design.
4. Design of power electronics to minimise the complexity of the system control.
5. Actuator Thermal Analysis and Optimisation.
6. Physical implementation of the spinal segment to validate simulations.
7. Comprehensive testing of DOF available in the system.

The limitations and elements out of the scope of the project are elaborated on below:

1. Implementation of closed-loop control with sensor feedback.

2. Integration of the spinal segment into a full spine.

3. Integration of the spinal system into a robot.

The thesis aims to explore the DOF achievable through electromagnetic actuation through simplicity. Therefore, including closed-loop control is out of the project's scope. Including closed-loop control with sensor feedback would require sensors and adjustable power sources on each actuator, increasing the complexity of the system and the control strategy. The thesis demonstrates that the desired movements can be controlled through open-loop control.

## 1.4 Achievements and Research Contribution

This thesis's research focuses on developing and optimising electromagnetic actuators capable of being implemented as spinal segments in robots, specifically focusing on multi-degree-of-freedom actuators and systems.

A key contribution is the systematic design and optimisation of the developed actuators. Analytical and simulation tools such as FEA, sensitivity analysis, and multi-objective optimisation enabled the refinement of the actuators' performance. Finally, a thermal analysis ensured the designs achieved thermal management. Actuator optimisation is often not prioritised during robotic development, leading to designs that lack thermal and power management. The advantages of the design and optimisation methodology are demonstrated in the novel Double-Helix and the linear solenoid plunger actuators, where multi-objective optimisation is achieved. The optimised Double-Helix (DH) actuator successfully demonstrated the ability to generate 2 DOF using a single coil, offering an alternative to single-axis coil systems with 1 DOF.

The solenoid plunger actuator was introduced to address the system requirements for the spinal segment actuator and was designed to achieve 3 DOF. The solenoid plunger utilised its versatile design and the benefits of electromagnetism to produce a linear actuator capable of configurable stroke lengths, enabling movement directly on the end effector. The solenoid plunger highlights another research contribution: actuator movement replaces the requirement of tendons and wires to enable movement in spinal segments. The solenoid plunger proved to be an efficient, scalable, and compact system enabled by optimising key factors like current, wire diameter, and the dimensions of the solenoid and magnet.

The research extended the solenoid plunger into a parallel Stewart configuration to develop an electromagnetic actuator for a spinal segment. The parallel actuator achieved 6 DOF by simply controlling the solenoid coil current. The design integrates the advantages of electromagnetic actuation with the stability and precision of parallel mechanisms, allowing for a large range of motion in multiple planes. The development of the electromagnetic spinal segment contributes to research on humanoid and quadruped spines, where electromagnetism is overlooked.

The thesis introduces a unique approach to producing MDOF spinal segments in robotics by designing and optimising electromagnetic actuators. The resulting structures provide a simple, efficient alternative to traditional actuators, with applications in humanoid and quadruped spines.

## 1.5 Overview of Dissertation

Following the introduction, Chapter 2 reviews the literature on actuators used in spinal manipulators. This literature review delves into the significant aspects of multi-degrees of freedom actuators within various robots and focuses on their advantages, applications, and various actuation methods. It elaborates on the ideal movement of spines in animals and humans and demonstrates how natural movements have been replicated in robotics. The chapter analyses and compares various robotic spines of quadrupeds and humanoids, providing insight into the design considerations that resulted in successful robots. It further highlights various actuation methods, configurations and their potential complications. A key aspect discussed in the chapter is the limitation of degrees of freedom available to some spinal robots and the complexity of control, emphasising the balance required in the design to achieve both. Chapter 2 outlines the key design considerations and implementation methods, forming a framework for developing the spinal segment actuator.

Thereafter, Chapter 3 delves further into the actuation of these robotic spines, focusing on linear actuators. The review examines electromagnetism as a form of actuation and explores its use in a spinal segment actuator. The chapter reviews the advantages and disadvantages associated with common actuation methods. It highlights electromagnetic actuation as an overlooked actuator that could solve the issue of increasing degrees of freedom whilst maintaining simple control. From this, the chapter elaborates on design considerations and emphasises that system actuators must be optimised.

A novel double-helix actuator is proposed to create an MDOF manipulator. Chapter 4 showcases a Double-Helix-Based actuator capable of two degrees of freedom. It highlights the actuation capabilities of a single actuator in two degrees of freedom and the potential of electromagnetism. It concludes that despite not being implementable in a spinal actuator, the Double-Helix demonstrates that multiple degrees of freedom can be achieved by a single actuator with a simple design.

A linear electromagnetic actuator is proposed in Chapter 5 to serve as the final actuator for the spinal segment system. The chapter covers the solenoid plunger's in-depth design and optimisation methodology and its implementation and testing. The methodology describes the analyses of the electromagnetic force and the aim of maximising the force generated whilst minimising the volume. Simulations in ANSYS Maxwell are used to verify these calculations and enable the selection of optimised variables. This is followed by Chapter 6, which uses the solenoid plunger in Chapter 5. In this chapter, a 6 DOF-compliant spinal segment combining Solenoid Plungers with a parallel mechanism is designed. The optimised actuator is dynamically modelled and implemented into the spinal segment system, followed by testing and experimental validation.

# Chapter 2

# Literature Review: Actuators and Spinal Manipulators

## 2.1 Introduction to Robotic Actuators

The field of robotics continues to evolve, with its change driven by technological innovations and advancements in manufacturing processes [7]. Robots and technical machines are used in various fields, from manufacturing and agriculture to medicine and research [25] [26]. These machines are designed to perform complex tasks, increase production and reduce reliance on human labour [8] [10]. Their growing prevalence is evidenced by the increase in robots used in search and rescue operations, dangerous investigations, automation, and agriculture [27] [14].

Interactive robots, in particular, are becoming part of everyday life, underscoring the increasing expectation for machines that can seamlessly replace or engage with humans [28]. Robots' current use and potential have stimulated the demand for developing high-precision robots capable of fine motion and multi-degrees-of-freedom (MDOF) [29]. Robots that replace or enhance human tasks require the dexterity, accuracy, and motion control that resemble human abilities. Replicating this is associated with numerous control and actuation challenges, resulting in current robots facing limitations in precision and the extent of their range of motion [30] [31] [12]. Addressing these limitations requires a careful balance. Expanding the degrees of freedom (DOF) enhances the robot's range and mimics human motion more closely but introduces significant challenges in system control and complexity [11] [7]. On the other hand, robots with limited DOF lack versatility, and their task availability is constrained [10]. Consequently, the design of high-precision robots represents a trade-off between increased DOF and complexity.

The movements achieved by robots are enabled by their actuation method and the actuator's configuration [32]. Most conventional actuators are designed for linear or rotary motion, which, while adequate for specific tasks, lack the flexibility for complex, multidirectional applications [18]. This limitation becomes particularly significant in robots requiring MDOF motion, such as humanoid, quadruped, hand, and gripper robots, where fine-tuned, precise movements in multiple planes are essential [30]. The lack of MDOFs necessitates using numerous actuators in a single joint or mechanism, increasing the system complexity, weight, power consumption, and operational workspace [16].

A particular field of interest is the development of humanoid robots, which are expected to perform numerous complex tasks [10]. To effectively integrate into environments occupied by humans, these robots require task versatility whilst prioritising adaptability and safety [8]. These characteristics

are crucial as they enable them to perform mundane tasks, manufacturing, and exploration in unsafe environments for human workers [27].

While attempting to replicate humans' complex motions in humanoids, many researchers look to nature for inspiration [9]. An ideal human body has variable flexibility, redundant MDOF, and mechanically elastic high-power muscles [8]. The flexibility provides safety and support while the redundant joints enable various movements. Reviewing animals' bodily structures, which emulate the requirements of robots, offers valuable information on the pivotal structures that will allow their dynamic and efficient movement [33].

## 2.2 Bio-inspired Robotic Design

Natural selection has enabled organisms to move with precision, efficiency, and control. This has inspired humans and prompted their efforts to replicate these complex and well-optimized systems [34]. Consequently, bio-inspired robots have become increasingly popular [35]. Examples are quadrupeds and humanoid robots, which often reflect nature by mimicking the physical properties of the animal's body, resulting in more natural and fluid movements [36] [37]. However, replicating the human body poses enormous control problems, and therefore, the design of these robots is usually simplified [12]. Typically, industrial and service robots are heavy and rigid, which limits their flexibility and adaptability, requiring powerful motors to control their joints [12].

A common source of stiffness in humanoid and quadruped robots is the design of the torso [38]. A flexible torso enables high load capacity, flexibility and large working space; however, most research on humanoid and quadrupeds revolves around robotic limbs [10] [9]. Despite this, recent humanoid developers have incorporated flexible spines to increase adaptability, DOF, range of motion and task availability, improving the flexibility of previous designs [10] [8]. Many humanoid robot spines gain flexibility by mimicking the human musculoskeletal system, utilising artificial muscles or tendons to control vertebral column motion [8].

Adding a flexible spine in humanoid and quadruped robots can save 25% of the total energy consumption compared to a rigid spine. Further, a controllable flexible spine improves the range of motion by 16%, enabling greater flexibility and motion variability [15]. By exploring and implementing bio-inspired robots' energy efficiency characteristics and increased degrees of freedom, some limitations associated with rigid robots have been overcome [39]. However, it is the actuators within the systems that control the movement of the spine, in which most of the proposed actuators do not achieve the force generation, strain output, frequency, power density, ease of control and repeatability as natural muscles [23].

To develop a functional spine for humanoid robots that facilitates fast and accurate movement, it is essential to examine the spine of humans and other animals to determine the key structures and design considerations [30] [9]. Looking to nature for inspiration, the cheetah stands out as a remarkable mammal for replication. The speed and agility of a cheetah are attributed to its highly flexible and adaptable spine, providing a key source of inspiration [33] [24]. The developments of robotic spines extend to quadruped robots, which serve a similar purpose to humanoid robots. Thus, analysing these designs enhances developers' ability to create highly adaptable spines for humanoid robots.

## 2.3 The Spinal Structure of Humans and Animals

Developing robotic spines requires an understanding of the fundamental principles of human and animal spines [33] [22]. The spine consists of the thoracic, lumbar, cervical and sacral regions [1]. The lumbar and thoracic segments are primarily responsible for the movement of the spine. The thoracic spine is limited by a ligament system and rib cage, enabling rotation. While the lumbar spine has a broader range of motion, allowing for more significant flexion and extension but limited rotation [22] [13]. The lumbar spine is an important element when replicating spinal movement as it bears the most weight and allows for the most significant amount of motion [13]. Ligaments supporting the spine control the range of motion of a joint and stabilise the bone alignment [9].

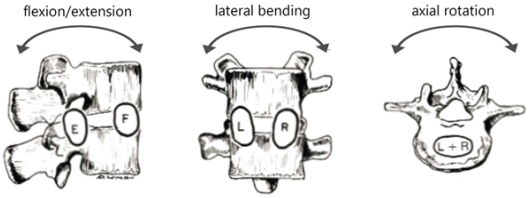


(a) Vertebrae Movement: flexion/extension, lateral bending, axial rotation [13]

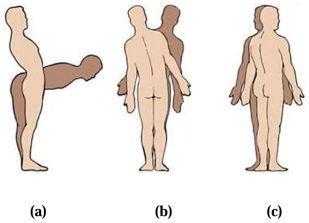


(b) Spinal Movement: (a) Flexion/Extension, (b) Bending, (c) Torsion [10]

Figure 2.1: Spinal Movement

Figure 2.1 illustrates the basic motions of the spine and vertebrae. As shown in Figures 2.1a and 2.1b, flexion is the forward bending about the perpendicular axis, and extension is the backward bending. Lateral bending correlates to tilting side to side, and axial rotation or torsion is the movement of the vertebrae around the perpendicular axis [13]. Spinal movements are the cumulative results of inter-vertebral movements, which move individually and about one another. In which most vertebrae have 6 DOF: three translations and three rotations [1]. Figure 2.2 shows the typical movement of a single vertebra it in 6 DOF.

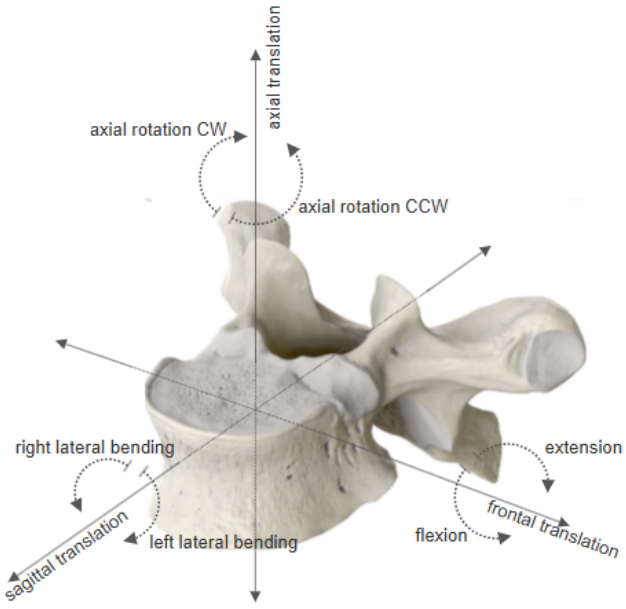


Figure 2.2: 6 DOF: rotation and translation of a single vertebra (image adapted [1])

The spine's structural diversity and movement capabilities vary across species, showing adaptations to each animal's lifestyle and orientation [13]. This variability demonstrates the spine's role in accommodating a range of dynamic movements. The range of motion (ROM) of the different spine sections, lumbar and thoracic, are summarised in Table 2.1

Table 2.1: ROM of the Thoracic and Lumbar Spine [1]

| **ROM** | **Flexion/Extension** | **Lateral Bending** | **Rotation** |
|---|---|---|---|
| **Thoracic Spine** | 26°, 22° | 30° | 47° |
| **Lumbar Spine** | 65°, 31° | 30° | 15.3° |

Table 2.1 highlights the contributions of each section of the spine, where the thoracic spine contributes largely to rotation and the lumbar to flexion and extension. In the design of humanoid robot spines, achieving complex spinal motions, particularly torsion involves challenges [40]. Torsion consists of the rotation of the central column, whilst the base of the spine remains stationary, a motion that rigid robots replicate by rotation from the hip or moving to turn around. However, including a more flexible spine allows for more dynamic movements, such as rotation with increased speed and agility [40].

## 2.4 Spinal Actuation in Robots

This section conducts a thorough analysis of spinal designs found in both quadrupeds and humanoid robots. The investigation aims to identify gaps in the literature on the ability of spinal structures to achieve MDOF and, subsequently, the actuators used. Specific attention is placed on the actuators within these systems and their ability to replicate the complex, natural movement of a biological spine with simple control. Examining and comparing the diverse spine structures reveals the advantages and disadvantages associated with various actuators and design methodologies.

## 2.5 Quadruped Spinal Motion

Millions of years of evolution have perfected the structure of the cheetah spine to endure high speeds, fast turns, and dramatic stops. The cheetah's agility is associated with high functionality and efficiency [33] [22]. The spine, which is responsible for these characteristics, has become a source of inspiration in the design of quadruped robot spines [41]. The Cheetahs' flexible spine allows for considerable bending, which enhances stride length and gait performance [41]. This spinal structure is designed to allow for slight vertical movement of the center of mass, minor body pitching, and extensive spinal flexion, achieving these movements by transferring energy efficiently [24]. The spine's ability to alternate between extended and contracted 'U' shapes during strides and its sigmoidal curve maximises speed and manoeuvrability [41].

Each vertebra in the spine has high degrees of freedom, and the effective control of different sections of the spine enables various movements. This sectional control is crucial for the bending actions that result in the cheetah's dynamic movements [42]. The successful movement and flexibility of the cheetah spine highlight the importance of each section of the spine being capable of MDOF and that these sections must be easily controlled. The ability of the spine to contract and extend, resulting in the forelimb and hind-limb movement, necessitates a minimum of 2 DOF [22]. This simplified approach is

used in most robot designs where the complex body structure of a desired animal is extracted, and the robot is designed to realise a specific function. This eliminates the potential multi-functionality the body could adopt in different situations [22]. Most quadruped robots have a stiff or under-actuated spine that limits the robot's mobility, resulting in the robot relying heavily on leg actuation [31]. Due to this, most research has gone into the movement of quadruped legs, ignoring the integral role the spine plays [43].

The movement of cheetahs demonstrates the critical characteristics within the spine that result in fast, agile and energy-efficient movements, which are desirable in quadruped robots. Recent advancements have shown that a flexible spinal structure is crucial for improving overall mobility as effective locomotion is initiated by the spine and followed by motion in the limbs [31] [13]. Integrating spinal flexibility into quadruped robots enhances running performance, steering and posture, demonstrating the critical role that spinal dynamics plays in animal locomotion and robot design alike.

### 2.5.1 Quadruped Robots: State of the Art

Recent advances in actuators and modelling technologies have dramatically improved the mobility of quadruped robots [42]. Traditionally, quadruped robots rely on stiff bodies and compliant legs, which limit speed, manoeuvrability, and adaptability compared to their biological counterparts [31] [13]. Table 2.2 highlights recent advances in quadruped robots with different spinal configurations, including rigid, passive and actuated spines. Table 2.2 explores feline and reptilian quadruped robots, their actuation and design methodology. The DOF shown in the table is the DOF per segment of the spine. Likewise, the number of motors or tendons used is highlighted in brackets.

Table 2.2: Summary of Quadruped Robots

| Ref | Name | Actuation | Weight | DOF | Modelling | Control | Therm. |
|---|---|---|---|---|---|---|---|
| [24] (a) | MIT Cheetah Robot | Motors<br>Cables | 33 kg | 3 | Mechanical<br>Gait Analysis | Feedback control | ✓ |
| [44] (b) | Kitty | Motors<br>Tendons (4) | 1.4 kg | 2 | Information based | PC motor driven | × |
| [11] (c) | Fanari | Spring-based (8) | 1.2 kg | 2 | Webots | Passive spine | × |
| [38] (d) | Bobcat | NA(Hinge joint) | - | 1 | Lagrange<br>Stochastic optimisation | None | × |
| [32](e) | Renny | Pneumatic<br>Artificial Muscles | 1.85 kg | 1 | Modal | Manually adjust | × |
| [14] (f) | Cheetah-Cub-S | Servo-motors<br>cables | 1160 g | 1 | Single track model | Pattern Generator | × |
| [42] (g) | Quasi Quadruped | Pneumatic | 3.99 kg | 1 | Forward kinematics | Feed-forward | × |
| [45] (h) | Salamander | DC motors (10)<br>Servo motors | - | 1 | Central pattern generators | - | - |
| [46] (i) | Nekobot | Servo motors<br>Spring damper | 753 g | 1 | - | Sensory feedback | ✓ |

Legend: () - Number of Individual item, Temp. - Temperature Analysis, ✓- Present, ×-Absent

Figure 2.3 shows the figures of the quadrupeds mentioned in Table 2.2

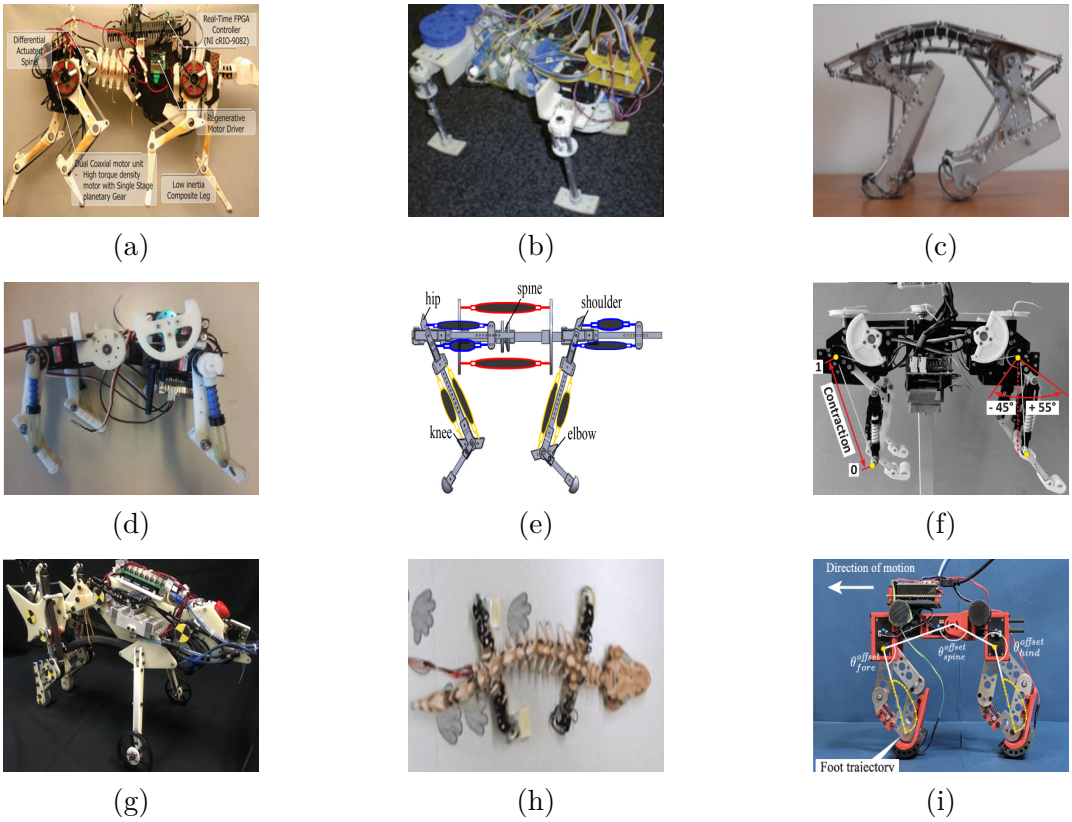


(a) (b) (c) (d) (e) (f) (g) (h) (i)

Figure 2.3: (a) MIT Cheetah. (b) Kitty. (c) Fanari. (d) Bobcat. (e) Renny. (f) Cheetah-Cub-S. (g) Quasi-Quadruped. (h) Salamander. (i) Nekobot.

Some robots, as shown in Table 2.2, have adopted aspects of the cheetah's spine, such as the MIT Cheetah Robot and Cheetah-Cub-S [24] [14]. By incorporating flexible spines, quadruped robots enhance their efficiency and agility. The MIT cheetah is an example as it uses differential cabling to actuate the spine, linking leg motions to spinal movements, which increase stride length and enable high-speed adjustments [24]. Like most quadruped robots, the MIT Cheetah uses high torque-density motors producing three DOF in the spine [43] [24]. The Cheetah-Cub-S also uses motors but prioritises simplicity with 1 DOF [14]. However, the simple system of Cheetah-Cub-S demonstrates that including a flexible spine, with simple control, dramatically increases the robot's mobility [14].

Spinal structures can vary, ranging from multiple joints and links, as seen in MIT Cheetah and Cheetah-Cub-S, to a single joint seen in Bobcat in Table 2.2 [38] [42]. Single-joint spines cannot curve, which limits the range of motion available and subsequently relies on hip and foot movement [13]. In contrast, a multi-joint spine, with large bending, requires the actuation and coordination of each joint quickly and precisely. Multi-joint actuation is typically achieved through cables that are driven by numerous actuators, as seen in Kitty, MIT Cheetah, Renny and Cheetah-Cub-S [44] [24] [32] [14] [42]. Renny [32] and Quasi Quad [47] are examples of quadrupeds that utilise cable actuation through pneumatically driven artificial muscles. In both systems, the robot improved its agility due to its ability to switch between different movement modes through the control of spinal flexibility [43]. Despite pneumatic-driven actuation providing control flexibility, the actuation method lacks the precision of motorised systems [48]. The challenges of robotic spine design lie in balancing flexibility and stability. Where spines with MDOF joints enable better coordination of galloping and bounding gaits, but in turn increase complexity [31]. Systems like Kitty [44], which incorporate compliant spines with multiple

degrees of freedom, show that locomotion can be achieved primarily through spinal movement, reducing the need for leg actuation but increasing spinal complexity [44]. Kitty is another quadruped which utilises four motors and tendons to achieve 2 DOF as shown in Table 2.2.

The complexities associated with MDOF do not need to be directly controlled, as demonstrated by Fanari [11] and Bobcat [38]. Fanari, a passive quadruped robot with a non-actuated spine consisting of 8 springs to gallop down a slope, produces the same DOF as Kitty without motor control [11]. Fanari demonstrates that the bounding gait entirely depends on the spine characteristics of robots. Similarly, Bobcat demonstrates the effectiveness of a passive spine, where decreasing the spinal stiffness increases the locomotion speed and flexibility [38]. However, the movement created by passive spines cannot be controlled and, therefore, lacks repeatability and versatility [11].

Quadruped robots have advanced in the last decade, where high torque density actuators and elastic elements allow the robots to be agile and robust [24]. Understanding the body structure of animals provides valuable insights on ways to increase functions in the robot without increasing the number of body modules [22]. The contrary is seen in robots that exhibit many tendons and motors with limited directionality and flexibility. Robots which realise a specific function require additional functional modules, such as additional motors, for every functional extension, making the system suffer inherent bulkiness [22]. Incorporating compliant spines into quadruped robots offers energy efficiency and manoeuvrability advantages, as compliant spines enable storing and releasing energy during locomotion [24] [38]. However, challenges remain in integrating these designs with actuators, maintaining control over complex spinal movements, and managing the increased DOF that flexible spines introduce. Similar characteristics are seen in humanoid spines. Some examples exhibit flexible spines with numerous motors and tendons, which increase DOF and complexity. In contrast, others offer a simpler, more rigid spine with fewer DOF [10].

## 2.6 Humanoid Robots

Humanoid robot development is an area that holds an eminent position in innovation and technology. As jobs become more demanding and skilled labour becomes scarce in industrialised countries, the involvement of robots in day-to-day life has increased [49]. Humanoid robots are machined to resemble humans driven by mechanical movements, functions and algorithms [7]. Humanoid robot development has increasingly focused on improving fluid and natural movement, particularly regarding the spine's flexibility and control. The human spine's multi-joint, viscoelastic structure with variable flexibility allows for a wide range of movements, including flexion, extension, and torsion, while absorbing shocks and mechanical impacts [10]. In humanoid robots, implementing a flexible spine structure is crucial for achieving the DOFs of humans. However, most robots have rigid torsos, so their mobility is limited and unnatural [9]. There are two main approaches for humanoid spines: multi-joint structures with 5-10 joints with variable flexibility and structures with one joint with low elasticity and high stiffness [10].

A multi-joint spine that enables each joint to move individually lessens the maximum torque required during motion compared to only using the hip of the crotch joint [50]. However, the multiple joints increase complexity, with numerous actuators and sensors. The replication of movement in the roll, yaw and pitch axis is highly beneficial for humanoid robots as it resembles the movement of a natural spine the best [10]. The thoracic part of a human spine can achieve 26° flexion, 22° extension, 30°

lateral bending, and 47° axial rotation, with each joint having 5 or 6 DOF [1] [40] [8]. Table 2.3 shows examples of humanoid robot spines, their DOF, actuation, and design and modelling approach. The DOF shown in the table is the DOF per segment of the spine, and in brackets, the DOF of the entire spine. Likewise, the number of motors or tendons used is highlighted in brackets.

Table 2.3: Summary of Humanoid and Spine Robots

| Ref | Name | Actuation | Weight | DOF | Modelling | Control | Temp. |
|---|---|---|---|---|---|---|---|
| [10] (a) | Sara | DC Motors<br>Permanent Magnets | 7.2 kg | 2 (6) | Kinematic<br>FEA | Gears<br>DC Motors | × |
| [50](b) | Kenta | Motors (40)<br>Tendons (40) | 19 kg | 3 (30) | CAD, geometric | Tension sensors | × |
| [8] | Kenji | Motors (30)<br>Tendons (30) | 21 kg | 3 (30) | Rotary encoders | Distributed Controller | × |
| [40] [48] (c) | Kotaro | DC Motors (16)<br>Tendons (16) | 20 kg | 3 (15) | Kinematic | Sensory feedback | ✓ |
| [40] (d) | Kojiro | AC Motors (15)<br>Tendons (24) | 45 kg | 3(12) | Kinematic | Sensor feedback | ✓ |
| [40] (e) | Kenzoh | Motor, Spring unit<br>Tendons (26) | - | 9 | Mechanical | Sensor Feedback | ✓ |
| [51] [16] (f) | Elastic diabolo | Stepper motor, jacks | - | 2 | Numerical, Kinematic | Inverse Geometric | × |
| [12](g) | ECCE1 | DC motors<br>Cables | - | 2 | CAD, Corba | Sensor Feedback | × |
| [7] (h) | Block Spine | Motors | - | 3 | CAD, Kinematic | Microcontroller | × |
| [9] [52](i) | ERMIS | Pulley<br>wires | - | 3 | FEA, CAD | - | × |
| [23](j) | Socket Joint | TCP muscles | - | 3 | Analytical | Thermal control | ✓ |
| [17] [15](k) | EMS | Solenoids<br>Springs | 310 g (6) | 1 | Analytical,FEA | PI controller | ✓ |
| [49](l) | Spine Man | SMA Springs | - | 3 | Experimental | Thermal | ✓ |

Legend: EMS - Electromagnetic Spine, TCP- Twisted and coiled polymer muscles, SMA-Shape Memory Alloy, FEA - Finite Element Analysis, Temp. - Temperature Analysis, ✓- Present, ×-Absent.

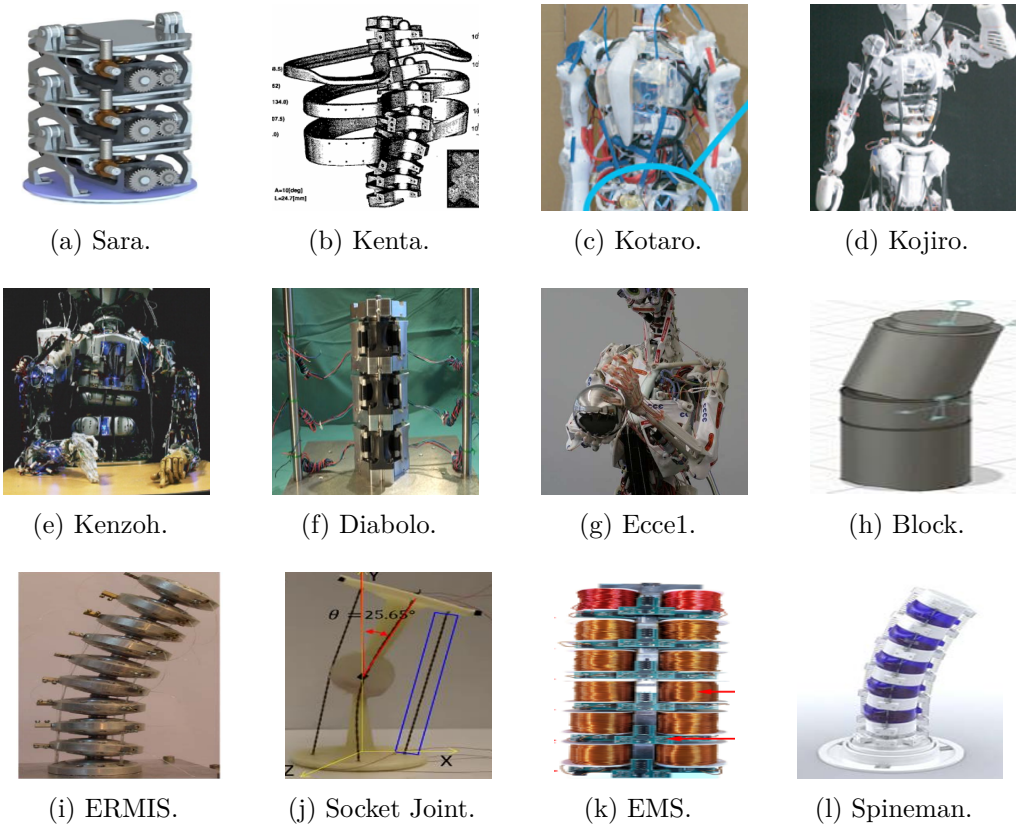


(a) Sara. (b) Kenta. (c) Kotaro. (d) Kojiro.

(e) Kenzoh. (f) Diabolo. (g) Ecce1. (h) Block.

(i) ERMIS. (j) Socket Joint. (k) EMS. (l) Spineman.

Figure 2.4: Summary of Humanoid and Spine Robot Images

Table 2.3 provides an overview of the state-of-the-art spinal designs for humanoid robots. Each example's DOF, actuation method, modelling and optimisation are compared and analysed to determine the most advantageous design characteristics. The examples used in Table 2.3 are associated with their image shown in Figure 2.4.

### 2.6.1 Actuator Types and DOF in Humanoid Spines

Most humanoid robots employ DC or AC motors to actuate spine joints, as shown in Table 2.3. The motors are often connected to tendons, cables, pulleys or artificial muscles that attempt to replicate the musculoskeletal structure of a human [10] [8] [40] [12] [10] [50] [8] [7] [9] [23]. The actuator systems are generally paired with elastic components, such as springs or silicone rubber elements, which add compliance to the system, making it better at handling mechanical shocks; this is seen in robots like Kenta, Kotaro, Kenji, Kenzoh, ERMIS and Kojiro. They employ a tendon-driven system in combination with motors to move their joints. These designs aim to emulate the flexibility of the human spine but often face challenges in control due to the large number of actuators [7].

For example, Kenta utilises 10 ball and socket joints driven by 40 muscles, requiring 40 motors to move each joint in 3 DOF [50]. Each motor controls the tension and movement of individual joints, contributing to highly redundant degrees of freedom. However, this redundancy comes with drawbacks. Having numerous actuators increases the complexity of the control system and the robot's overall weight, which can result in slow response and the need for more powerful motors [12]. Additionally, these systems often struggle with back drivability, making them inefficient when interacting with external forces [23] [15]. Kenji [8], Kotaro [40], and Kenzoh have similar structures that have been

improved per iteration. As demonstrated in Table 2.3, these humanoid spines make use of many motors and tendons, resulting in large systems as illustrated in Figure 2.4: 2.4b, 2.4c, 2.4d and 2.4e.

An ideal actuator can perform more than one motion, is energy efficient, and is adaptable [8]. Regarding motors, the contraction of the motor connected to a tendon requires a complementary motor to draw the structure back to its original position, demonstrating that two motors are required per DOF [49]. This is seen in wire or tendon-driven musculoskeletal robots such as Kenta, ECCE1, Kotaro, Kenzoh and Kojiro, where one motor for every cable can only pull [16]. Therefore, (N+1) motors are needed in the system to control N degrees of freedom [49].

Sara is an example of a humanoid robot spine that uses motors without tendons. Sara achieves a flexion of 10° per segment and a torsion of 15° per segment. Sara's actuation consists of DC motors combined with gears to drive one of three joints. Each joint has 2 DOF, contributing to 6 DOF of the whole spine [10], illustrated in figure 2.4a. Sara's spinal joints can only move in 2 DOF, limiting the overall range of the spine and the diversity of the robot's movement.

Other actuation methods include springs, Shape Memory Alloys (SMA), Twisted and Coiled Polymer (TCP) artificial muscles, pneumatic muscles, and dielectric actuators [23] [49]. The spinal structure, Socket Joint in Table 2.3 utilises a ball and socket joint with TCP tendons that are actuated through resistive heating. This technique enables movement in 3 DOF. However, the structure illustrated in figure 2.4j lacks rigidity and cannot support a high payload [43].

Electromechanical actuators, on the other hand, are rarely implemented as spinal actuators in both humanoid and quadruped robots. The Electromagnetic Spine (EMS) example in Table 2.3 can only achieve 1 DOF, lateral bending. However, the simple structure benefits from low power consumption and high output force [17]. The actuator consists of solenoids and an E-shaped core, which moves as independent solenoids are excited. Despite the lack of range of motion, the EMS spine demonstrates that movement can be achieved through the actuator alone, removing the need for tendons or wires. The EMS spine illustrated in Figure 2.4k reflects the relationship between complexity and DOF, where the simple structure is limited to 1 DOF.

The DOF of a humanoid spine correlates to the number of actuators in a balance between complexity and functionality. Robots like Kenta and Kenji have 30 DOF in the spine, enabling more human-like movements, while simpler designs may only have 3 DOF [40] [9]. MDOF allows for a range of motions, including bending, twisting, and flexion, at the cost of increasing the number of actuators.

The primary drawback of using many actuators is difficulty in control and mechanical complexity [46]. Robots that employ numerous motors must synchronise each actuator with the others to produce smooth, coordinated movements, which requires sophisticated algorithms and control systems [46]. Furthermore, tendons driven by motors rely on tendon length control, where each length is controlled based on calculated trajectories. This increases complexities in producing precise joint control due to the elongation of tendon wires and tendon path intersection [40]. In addition, the large number of actuators adds to the robot's mass, potentially reducing power efficiency and agility [8]. Multiple actuators' power consumption and heat can result in suboptimal operating conditions, mainly if the cooling system is insufficient [24]. Table 2.3 presents a summary of humanoid spine robots that either addressed thermal effects from the actuators or included a thermal analysis. Notably, only half of these

robots considered the heat produced and its impact on the robot's functionality, with these examples being a form of electromagnetic actuation.

Traditional rigid robot actuation results in stiff movements that are not conducive to tasks requiring flexibility [11]; however, increasing the flexibility requires more power and integrated control systems. Therefore, designing and modelling humanoid spinal actuators becomes a trade-off between complexity and task availability. Where actuators both enable and restrict the robot's potential DOF and overall functionality [8].

### 2.6.2 Range of Motion (ROM) of Humanoid Spines

Table 2.4 summarises the ROM of most of the humanoid spines in Table 2.3 according to their flexion and extension, lateral bending and rotation. The ROM per segment is provided, with the ROM of the entire spine stipulated in brackets; a dash (-) represents that the information was not explicitly mentioned, and an (×) represents no movement in that DOF.

Table 2.4: Summary of Humanoid Spine ROM

| Ref | Name | Flexion/Extension | Bending | Rotation |
|---|---|---|---|---|
| [10] | Sara | - | 10° (30°) | 15° (45°) |
| [53] [54] | Kenta | 10° (135°) | 10° (45°) | 10° |
| [40] [48] | Kotaro | 10° (50°) | 10° (50°) | - |
| [40] | Kojiro | 90° (including hip) | - | - |
| [55] | Kenzoh | 9° (45°) | 8° (40°) | 6° (30° ) |
| [51] [16] | Elastic diabolo | 30° | 30° | passive |
| [9] [52] | ERMIS | 13° (120°) | 13° (120°) | × |
| [23] | Socket Joint | 25° | 25° | 22.5° |
| [17] [15] | EMS | × | 9.16° | × |
| [49] | Spine Man | 17° (100°) | 17° (100°) | passive |

Legend: () = ROM of the entire spine, without brackets = ROM of one section, - , not explicitly mentioned in literature, ×-Absent.

By correlating Table 2.4 and Table 2.3, which details the humanoid DOF and actuation mechanisms, a relationship between the two emerges. Sara exhibits a lateral bending of 10° per segment, resulting in a total bend of 30° and rotational movement of 15° per segment with 45° in total. However, it lacks flexion and extension, which is consistent with its 2 DOF per segment [10]. Kenta has a large cumulative flexion and extension but limited rotation, 10°, with each segment enabling 10° requiring numerous segments to achieve the total 135° extension and 45° bending [53]. The large ROM is attributed to its high DOF (30 in total), controlled by 40 motors and tendons, enabling high flexion and constraining rotation. Similarly, Kotaro achieves high overall bending and flexion but limited rotation, with fewer DOF (15) [23]. Kenta, Kotaro, and Kojiro utilise multiple segments to achieve a greater range of motion (ROM), which necessitates additional actuators and tendons, where the ROM is associated with DOF and more motors [54] [40]. The Socket Joint is seen to have a consistent ROM across the categories, with fewer tendons and sections, as seen in Figure 2.4j, enabled by a

well-distributed 3 DOF actuator [23]. Others, like Elastic Diabolo, have passive ROM, where the movement in that direction cannot be actively controlled [16].

Overall Table 2.4 indicates higher DOF correlates with greater ROM, particularly in flexion, extension and bending. With 30 DOF, Kenta produced the highest flexion, whilst robots with fewer DOF, EMS, exhibit limited movement with 1 DOF [15]. Further, the DOF is also associated with rotation, where rotation is generally present, either actively controlled or passively, in robots with 3 DOF per segment, such as Socket Joint and Kenzoh. Increasing the DOF typically increases the ROM but not necessarily uniform ROM across all axes. The limitations in ROM in the rotation axis result from design choices, actuation methods, and structural constraints.

### 2.6.3 Design and Modeling of Humanoid Spines

The structural design of the spine in humanoid robots typically consists of serial, parallel, and hybrid structures. Serial structures like the one used in Kenta, Block, Sara, Diabolo, and ERMIS rely on a chain of individual joints connected by tendons or elastic materials [50] [7] [23] [9] [49]. Parallel structures, EMS, Socket Joint and Spineman, employ multi-joint linkages to increase flexibility while improving stiffness [15] [51] [10]. Hybrid structures, including Kotaro, Kojiro, Kenji, Kenzoh and ECCE1, use a combination of serial joints, tendons, and motors parallel to the central column [40] [8]. Table 2.3 highlights a crucial point: the DOFs that spines achieve are more significant in the designs that utilise a parallel or hybrid structure due to the multidimensional point of control and actuator positioning.

The complexity of the spinal structures, their movement and force requirements are typically characterised using forward kinematic, Lagrange, stochastic optimisation, and other modelling techniques [40] [16] [51] [9]. The spinal systems are typically modelled using tools such as Finite Element Analysis (FEA) or multi-body dynamic simulations to optimise the structural integrity and flexibility [10] [50] [15]. Modelling the spine's movement through numerical and analytical methods enables accurate feedback for control and verification of design requirements, forming an integral element in developing functional humanoid robots.

### 2.6.4 Control of Humanoid Spines

Replicating human movement, particularly the movement of the spine, poses many control problems due to its complexity in structure and the large number of actuators to control [40]. This places limitations on the interactions the robot can engage in [12]. Traditional control methods often rely on closed-loop control through sensory feedback and inverse kinematics, but these approaches are limited when dealing with highly redundant systems [15] [49]. Further complications arise from acquiring system information, where the relationship between actuator operation and the resulting sensory information changes rapidly, contrasting with the response of the control algorithm [8]. These issues are primarily related to structures which require numerous actuators and tendons. To overcome these challenges, researchers have explored distributed control systems that divide the control tasks among multiple subsystems, improving response time and coordination between joints. More advanced control algorithms, such as those used in Kenji, aim to provide adaptive control by adjusting the mechanical stiffness of each joint [8]. These algorithms can modify the robot's posture and movement in real-time, allowing for safer and more efficient interactions with the environment.

## 2.7 Conclusion

Balancing flexibility and control is the key complication in designing a humanoid robot spine. While increasing the number of DOF makes the robot more versatile, it also makes the control system more complex and introduces issues related to power consumption, weight, and synchronisation [8]. Furthermore, the mechanical complexity of these designs often makes them less reliable in real-world applications, where robustness and durability are critical.

Despite these challenges, flexible spines offer significant benefits. A compliant spine allows robots to absorb shocks, reducing the risk of damage when interacting with humans or navigating complex environments [51] [12]. It also enables more natural movements, improving the robot's ability to perform tasks that require agility and precision [7].

The development of humanoid robot spines continues to evolve, with ongoing research exploring better ways to model, actuate, and control these complex structures. While current designs face challenges, particularly with the high number of actuators and the complexity of control, the potential for creating robots that move and interact more like humans is promising, with designs focusing on simplifying actuation systems, improving control algorithms, and achieving better energy efficiency [15] [10].

The review of humanoid and quadruped spines and their actuation methods highlights their design's versatility and complexity. It demonstrates the benefits of mimicking biological systems to optimise designs to produce energy-efficient, adaptable robots. Despite the design challenges elaborated on above, the field of humanoid robots shows promising advances in many disciplines. The insights from examples and previous research have guided the methodology in developing a humanoid spinal actuator.

Designing a spinal actuator capable of replicating the movement of a human spine requires motion capabilities in 6 DOF, with an additional benefit of increased DOF of each spinal segment. However, many of the spines discussed in Table 2.3 and 2.2 do not achieve as many DOF per segment, and furthermore the range of motion is limited per segment requiring numerous segments to increase the ROM. Despite many designs achieving numerous DOF of the entire spinal structure, most DOF are not actively controlled but rather enabled passively. This paper aims to produce a spinal actuator that produces 6 DOF per spine segment. Within the design of humanoid and quadruped robots, the actuator involved is the crucial element which determines the functionality and effectiveness of the robot; careful design and optimisation of the individual actuator need to be performed before the design of the integrated system. Chapter 3 highlights the advantages and disadvantages of standard linear actuators and the potential of Electromagnetic Actuation (EMA) as a powerful linear actuator for use in humanoid spines.

# Chapter 3

# Linear Actuator Design Review

## 3.1 Actuation Methods

Numerous humanoid and quadruped spine robots have been developed, and the factor that differentiates them is the actuation method, their degrees of freedom, and their flexibility. Most are actuated with motors, with some designs utilising Shape Memory Alloys (SMA), pneumatic, hydraulic and electromagnetic actuation [56] [37] [39] [57]. Each method poses unique challenges, where the actuation method selected depends on the robot's implementation and application requirements [58]. Essential features to consider when choosing a method of actuation are size, output power, weight and desired deformation, as these will determine the performance and limitations of the robot. Table 3.1 compares various actuation methods and their advantages and disadvantages.

Table 3.1: Actuation Method Comparison

| **Actuation Type** | **Advantages** | **Disadvantages** |
|---|---|---|
| **Shape Memory Alloys** | Simple structure<br>Reasonable power | Low speed, Slow response<br>Prone to hysteresis [37] [56] |
| **Pneumatic/Hydraulic** | Improved deformation<br>Fast response | Complex equipment setup [56]<br>Intricate designs |
| **Motor Driven** | On board energy component<br>Independent, High power | Increased weight, One DOF<br>Limited life cycle [59] |
| **Electromagnetic** | Fast Response, Simple control law<br>Low cost, light-weight<br>scalable, Variable deformations | Heating<br>Loss of electrical energy [57] |

Table 3.1 highlights the various trade-offs accompanying each form of actuation. A common limitation is that actuators, in general, can only control one mode of direction in robots [60]. Increasing the number of actuators or additional control sources can enable more degrees of freedom but simultaneously increases its complexity [60]. This is evident in motor-tendon driven and SMA actuators, which require additional structures, such as tendons or artificial muscles, to enable their actuation [17]. Further complications, such as insufficient compactness associated with hydraulic and pneumatic actuators' reduce the robots' scalability and implementation environment [60] [34]. Actuators enabling displacements in two directions (back and forth) in the same plane are advantageous as they reduce the required actuators and simplify the system control. Examples are pneumatic, hydraulic and electromagnetic actuators which can produce displacement in two directions along a plane with an adjustable stroke length. This capability distinguishes these actuators from tendons driven by motors,

which can only create motion in one direction.

Electromagnetism as a method of actuating different sizes and types of robots has gained interest in recent years due to its ability to create deformations with simple control [57] [61]. However, the use of motor-driven, pneumatic and hydraulic actuators overshadows the exploration of electromagnetics in humanoid and quadruped development, as emphasised in Section 2.1 Table 2.3 and Table 2.2. Despite this, the lightweight, low cost and simple design of electromagnetic actuators provide a promising solution to the drawbacks of additional structures and complex control mechanisms associated with other actuators. Their ability to control their magnetic field to produce complex deformations without requiring expensive equipment allows the robot to be scaled to any size [62] [19].

### 3.1.1 Electromagnetic Linear Actuation

Electromagnetic actuation (EMA) typically consists of electromagnetic coils and permanent magnets [61] [63]. EMA offers the advantages of fast response, simple control, low manufacturing costs, and large displacements [20] [63]. Within EMA, the solenoid is widely used due to their ability to create current-dependent magnetic fields, allowing easy control of the force generated [20]. The conventional linear solenoid actuator consists of a long loop of wire wrapped around a metallic core (plunger), which produces a magnetic field and force to generate a linear motion of the core when current is applied [21]. These systems are often called voice coil actuators or solenoid plungers [19]. These actuators facilitate bi-directional motions and can easily be controlled by the input current, a property that sets them apart from other actuation types [21] [63].

Solenoid plunger and linear electromagnetic actuators (LEMAs) are readily available and have been widely used to generate rectilinear and turning motions, often through pairs of solenoids by generating thrust directly on the end effector with high dynamic performance and reliability [20] [63]. Electric motors also offer bi-directional motion that is easily controlled by input current. However, solenoids have been assumed to have several drawbacks, including overheating, which decreases power availability and results in lower driving forces [64]. Therefore, their optimisation and thermal management are crucial [21]. To increase the output force of these actuators, the current in the coil and the number of turns in the solenoid invariably increase [62]. With this, the size, mass and heat dissipated from the actuator rise accordingly. [17] To improve the force output while reducing the system's volume, the coil's and the magnet's structural parameters need to be optimised [19].

## 3.2 Design and Optimisation

Regardless of the actuation method, the involvement of multiple DOFs in robots is accompanied by unprecedented challenges [65] [24]. Translating a mechanical design into a robot includes determining the design objectives, variables, and constraints [9] [65]. Objectives in moving robots cannot always be modelled, as some designs require adaptability to their environments, which necessitates large computing power. The geometry, material, and actuation determine the mechanical behaviour of the robot, and their infinite variability creates a large design space that can be explored. To identify the most effective design, optimisation tools are required to guide the designer [65]. The complexity of designing robots is due to the overlap between design variables, where actuation is restricted and enabled by material and geometry [19] [8]. Therefore, integrated optimisation methods are the most

effective [65].

To achieve co-optimisation, simulation and analytical solutions are required [65]. The analytical results are often compared to FEA simulations in software such as ANSYS, COMSOL, Simulation Open Framework Architecture (SOFA) and Matlab Simulink [19] [65] [38]. Standard optimisation models within the software used are Non-Dominated Sorting Genetic Algorithm-II (NSGA-II), sequential optimisation method (SOM), and dimension reduction optimisation method (DROM) [19].

In EMA, the dynamic analysis of the overall system requires the solution of a coupled problem consisting of electromagnetic fields, electronic circuits, and mechanical motion of the actuator [66]. Decoupled solutions separate the magnetic field and electric circuit from the mechanical problem. However, this approach does not fully evaluate the relationship between the input and desired output [66]. The dynamic and kinematic models of the electromagnetic system are established through Lorentz force law and electromagnetic field theory to obtain the functional relationship between the force and current [63]. These models use numerical and FEA methods to solve nonlinear systems, while analytical models describe the quantitative relationship between multiple independent and dependent variables [66]. Both methods are essential in optimising the parameters and the relationship between variables represented in the system [63]. Therefore, when modelling and analysing electromagnetically actuated designs, FEA and analytical methods are used to supplement one another [15].

### 3.2.1 Effect of Temperature

Table 2.3 and Table 2.2 highlight that some actuator design methods do not consider the effect of temperature. However, temperature analysis is essential when dealing with electromagnetic actuators, as they are prone to heating and are thermally limited [62] [67].

When current flows through a conductor, heat is generated due to electrical friction and is directly proportional to the watts lost in the conductor [64]. The resistance of a conductor changes with its temperature, where the ratio between the temperature rise and the rise in resistance is the temperature coefficient, coppers' is 0.00388 at $20°C$, showing the resistance will increase for each degree [64]. Figure 3.1 shows the relationship between the rise in temperature and the conductivity of copper, clearly demonstrating that the wire's properties diminish with the increase in temperature [2].

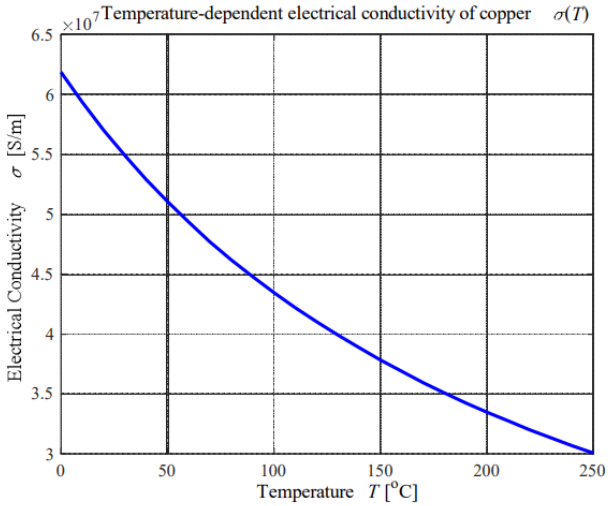


Figure 3.1: The relationship between the conductivity of copper and temperature [2]

The performance of electromagnetic coils decreases with the temperature rise, affecting the functionality of the actuator [67]. The heat generated from the conductive copper coil depends on the current, the resistance and the time in which the current flows, per the Joule-Lenz law [60]. The increase in temperature affects the material properties of the copper winding, resulting in a decrease in its conductivity and damage to the insulation of the wire [2]. Therefore, it is essential in applications that require high or continuous current that thermal effects are managed.

The coil configuration and the effect of temperature are evident considerations in the design process of electromagnetic robots. However, to optimise these robots further, design variables and their correlations need to be determined and analysed [65].

## 3.3 Design Considerations

Electromagnetic robots rely on the generation of a magnetic field to produce motion [63]. Factors influencing the strength of the magnetic field include the electromagnetic structures' wire dimensions, current capacity and core material [68]. Each variable is associated with inevitable trade-offs that must be considered throughout optimisation.

The magnetic field is directly proportional to the current in the wire, where higher currents produce stronger fields [39] [57]. However, the ampere capacity of copper wire sets the limit for the safe transfer of electrical current [69]. High currents for extended periods cause overheating; therefore, the wire size and resulting current must be chosen according to the American Wire Gauge (AWG) standard [70].

Equation 3.1 shows that the magnetic field in the centre of a solenoid is dependent on the current through the coils, $I$, the number of turns, $N$, the overall length, $l$, and the permeability of free space, $\mu_0$ [39].

$$B = \frac{\mu_0 \cdot I \cdot N}{l} \tag{3.1}$$

Therefore, Equation 3.1 demonstrates that the current limitations due to wire size and resistance can be compensated by increasing the number of turns in the coil [71].

### 3.3.1 Magnetic Materials

Most electromagnetic systems include magnetic or ferromagnetic material within the design of the actuator in the form of a core or a moving magnet [57] [60] [37]. Permanent magnet (PM) integration in electromagnetic robots is widely used as a mechanism for movement [57] [60] [37]. In some robotic applications, soft magnetic materials such as iron and nickel are used [68]. These materials have high permeability and low coercivity, and they are easily magnetised by external fields. Others use hard magnetic materials, such as neodymium iron boron magnets (NdFeB), which have lower permeability and higher coercivity and provide stable, long-lasting permanent magnets [68].

Ferrite and neodymium magnets are commonly used in robotics, automation and electronics [72]. Neodymium magnets are particularly popular as they have the most significant power-to-weight ratio among permanent magnets (PMs) [73]. Table 3.2 compares the highest quality neodymium and ferrite magnet properties.

Table 3.2: Magnet Property Comparison [6]

| **Property** | **Neodymium N52** | **Ferrite Y40** |
|---|---|---|
| **Magnetic Field Strength (Tesla)** | 1.4 | 0.5-1 |
| **Coercive Force Hcb** ($kA/m$) | >= 796 | 354 |
| **Operating Temperature** | 80° | 180° |
| **Max. energy product BH** ($kJ/m3$) | 398-422 | 37.5-41.8 |
| **Remanence Br** ($mT$) | 1430-1480 | 440-460 |

Neodymium magnets have high coercivity (resistance to demagnetisation), maximum energy product and remanence (strength of magnetic field), making them suitable for electromagnetic actuation [72] [19]. However, they have a lower operating temperature than ferrite magnets [72]. Neodymium magnets are graded in strength from N30 to N52, with higher numbers indicating stronger magnets. The interactions between magnetic materials and electromagnetic coils generate the forces and torques used to create motion in electromagnetic robots [68].

### 3.3.2 Electromagnetic Forces

To effectively control an electromagnetically actuated robot, the characterisation and understanding of the magnetic fields within the robot is essential [68]. In applications that rely on a moving coil or magnet actuation, the coil current controls the forces that enable their movement. Control is often achieved by alternating the current direction, which switches the electromagnet's polarity. This results in the PM repelling alternating ends of the solenoid, producing the actuator movement [57] [34].

In solenoid-magnets systems, two forces are exerted on the solenoid - one is the electromagnetic force induced by the magnetic field inside the solenoid when current flows. The other is the magnetic force caused by a PM plunger [20]. The resultant force by the solenoid depends on the length, diameter, air gap, coil turns, applied current, and the type of PM [21] [20]. The electromagnetic force from the solenoid actuator is proportional to the change in inductance of the coil with respect to the change in the position of the PM plunger and the current flowing through the coils [21] [20]. Therefore, the solenoid's electromagnetic force depends on the solenoid's position, and the plunger [19].

## 3.4 Conclusion

The primary objective of this dissertation is to design a 6 DOF robotic actuator for potential use as a segment in humanoid spinal robots. EMA has been identified as the actuation method for the design. The review of linear actuators highlights the importance of the design of EMA and the optimisation of the variables influencing the force and heat produced. Given the complexities associated with dynamic movement in robotic systems, the individual actuators must be optimised before proceeding with the overall system design. The desired actuator should be able to control motion in multiple directions, be lightweight, have simple control, be capable of scalability and produce a high output force. To create an actuator with the desired characteristics, a novel 2-degree-of-freedom Double Helix Actuator is explored. The DH actuator is initially analysed on a smaller scale, with the primary objective being to explore the potential of generating MDOF from a single coil in order to assess its effectiveness as an actuator.

# Chapter 4

# Double Helix-Based Actuator for 2-Degree-of-Freedom Motion

## 4.1 Introduction

Robotics is an evolving technology with applications in industrial automation, agriculture, and medicine [74] [75] [76]. Among the various actuation methods, electromagnetic systems that wirelessly control robots and micro-robots have gained considerable interest [77]. Magnetic fields are powerful tools for the remote actuation and control of magnetic devices, particularly in medicine and bioengineering, due to the strong permeability of magnetic fields in tissue at low frequencies [78] [79] [80] [81] [77]. This makes them a relatively harmless and effective approach to wirelessly controlling robots without built-in energy sources [75] [80]. Magnetically driven micrometer-to-millimeter-scale robots exhibit great potential in drug delivery, minimally invasive surgery, microfluidic tools, and micro-factories, with ongoing efforts directed at designing devices with multiple independently controllable degrees of freedom (DOF) [78].

Most electromagnetic systems are designed with coil structures or permanent magnets as their base and are arranged around the workspace to direct a magnetic agent or micro-robot [79] [80]. Table 4.1 presents electromagnetic actuation systems, highlighting their base structure, degrees of freedom, magnetic field direction, and arrangements for specific applications.

Table 4.1: Magnetic Actuation Base and Systems

| Type | DOF | Field | System | Application | References |
|---|---|---|---|---|---|
| Solenoid | 1 | A | Helmholtz | Medical | [82] [83] [84] |
| | | A | Maxwell | Medical | [82] [84] |
| | | A | Electromagnet | Control, Medical | [78] [79] [80] [83] [85] |
| Saddle | 1 | P | Parallel | Microrobot, Medical | [86] [74] |
| Toroid | 1 | C | - | Medical, Dampers | [87] [88] |
| Helical | 1 | P | - | Gripper, Medical | [89] [88] |
| PM | 1 | - | Linear | Medical | [90] |
| | | - | Halbach | Medical | [78] [77] [81] |

Legend: DOF: degrees of freedom, A represents the field along the axis of the coils, P is perpendicular to the axis of the coil, and C denotes a circular field.

Solenoid-based electromagnetic systems are widely used due to their ability to generate current-dependent magnetic fields, providing safety and controllability, making them ideal for fast and accurate movements [77]. Solenoids can operate individually or with cores, producing an electromagnet with stronger fields. Combining multiple electromagnets can create distributed fields with increased DOF [81] [79].

Common solenoid-based systems, such as Helmholtz and Maxwell coils, utilise paired coil configurations, producing a magnetic field along the coils' axis, enabling one DOF. Helmholtz and Maxwell's coils produce uniform magnetic fields; however, they require larger spaces due to their paired configuration and offer limited directionality due to the DOFs per pair [82] [75] [84]. These coils have low spatial efficiency and are restricted to operating within the coil's workspace [77]. They rely on using multiple coil pairs around the workspace, which are rotated and actuated to create a magnetic field in a specific direction. Therefore, Maxwell and Helmholtz's coils are often combined to achieve more control and field directionality [77]. As highlighted in Table 4.1, the solenoid is a versatile base supporting various configurations and applications.

In contrast, saddle coils consist of a pair of coils that produce an approximately uniform magnetic field perpendicular to the coil axis [77]. When arranged with two coil pairs, they can produce magnetic fields in both vertical and perpendicular directions, offering greater space efficiency and lower energy requirements than Helmholtz and Maxwell pairs [77] [74].

Permanent magnets are another key base for electromagnetic actuation, generating strong magnetic fields that depend on their shape, size, and orientation, as shown in Table I [77]. They do not require a power source, which is advantageous as this reduces overheating and energy consumption [76]. However, since the magnetic field cannot be turned off, manipulating robots relies on the magnet's movement [81].

Halbach, Helmholtz, Maxwell, and saddle coil configurations utilise the fundamental principles of solenoids or permanent magnets to produce magnetic fields capable of actuating an agent. These configurations achieve more DOF only when their base structure is paired, combined or rotated, necessitating multiple magnets or solenoid pairs for multi-axis agent control. This requirement represents a significant drawback of these structures, increasing their spatial occupation and limiting the workspace for the agent [79] [91].

Given the limitations of traditional magnetic actuation systems highlighted in Table 4.1, the double helix (DH) structure presents a compelling actuator alternative. Unlike conventional solenoids and permanent magnets, the DH configuration can produce a magnetic field that is parallel or perpendicular to the coil axis, enabling dynamic control of the magnetic field in multiple directions and facilitating two DOF [92]. This unique characteristic enables controlled actuation of magnets, providing greater flexibility and functionality in robotic applications. Furthermore, the DH structure is versatile and can consist of rectangular, elliptical or circular coils. The elliptical coil has a greater minimum bend radius and more accurate dipole fields [93] [92]. The flexible design can be modulated and extended to produce multipoles by nesting multiple coil pairs, increasing their DOF for robotic manipulation [92] [94]. Additionally, the simple structure makes it cost-effective and yields highly efficient compact devices for a given power output, capable of generating large Lorentz forces [93] [92] [95] [96]. The strength of the magnetic field can be enhanced by adding more turns and layers, resulting in a uniform dipole field with a larger area of influence in the aperture [97].

Despite the advantages mentioned above and wide use of DH coils in the fields of nuclear magnetisation [86], particle accelerators [94] [92], beam steering [98], and superconducting dipoles [93], their application as an actuator has not been explored. Thus, this chapter proposes the DH as an actuator and explores its various operating ranges, focusing on producing magnetic fields capable of actuating small magnets in multiple directions. From this, the contributions of this chapter are

- The design and investigation of the DH configuration as an actuator for magnetic devices.
- Exploration of the magnetic field produced by rectangular and elliptical coils.
- Simulation and experimental validation of the DH actuation system aimed at achieving multidirectional motion of magnetic materials.
- Optimisation of coil configuration and thermal analysis.

## 4.2 Double Helix Actuator Design

### 4.2.1 Geometry

The DH coil consists of two solenoids with oppositely tilted windings to the vertical axis, $B_z$, as shown in Figure 4.1. One solenoid is situated within the other, and due to the tilt angle, $\phi$, they generate both longitudinal (solenoid) and perpendicular (dipole) magnetic fields depending on the current direction in each coil. Figure 4.1 illustrates the windings in the outer and inner coils (Figure 4.1a and 4.1b respectively).

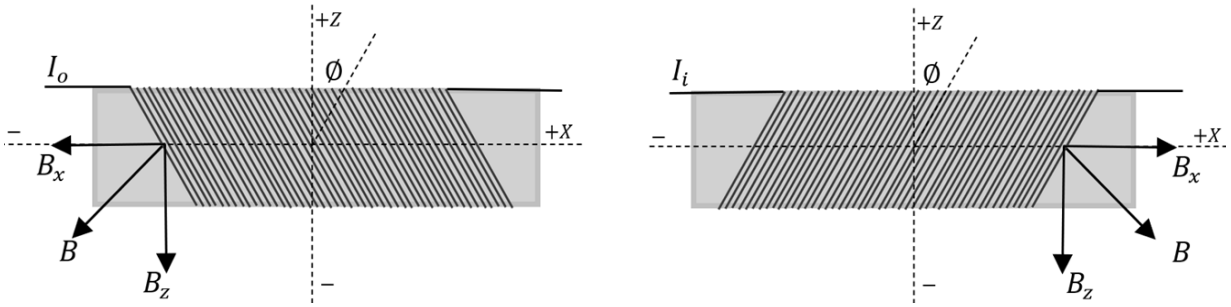


(a) Outer Coil (b) Inner Coil

Figure 4.1: The DH coil structure: (a) The outer tightly wound coil tilted at an angle $\phi$, and (b) the inner coil oppositely tilted at $-\phi$. $I_o$ in (a) and $I_i$ in (b) represent the current in the inner and outer coil, respectively.

The current direction and magnetic field characteristics are summarised in Table 4.2, which shows the magnetic field direction created by various combinations of currents.

Table 4.2: Magnetic Field Distribution

| **Currents** | $I_i+$ | $I_i-$ |
|---|---|---|
| $I_o+$ | $B_x+$ | $B_z-$ |
| $I_o-$ | $B_z+$ | $B_x-$ |

From Table 4.2 when the coils are superimposed concentrically and driven with current in opposite directions; the solenoid field, $B_x$, cancels and then dipole field, $B_z$, adds, resulting in a magnetic field

in the positive or negative $B_z$ direction. However, if the coils are driven with current in the same direction, the resulting magnetic field will be a solenoid field in the positive or negative $B_x$ direction.

### 4.2.2 Magnetic field

Figure 4.1 illustrates that the layers of the DH coil consist of tilted solenoids. Consequently, the magnetic field strength of the DH can be computed based on the solenoid field equations. The magnetic field depends on the conductor width and the tilt angle [93]. The conductor width determines the turn spacing, affecting the length, width, and coil pitch. For a conductor with a width $d$ and angle $\phi$, the density of turns per meter along the solenoid axis is given by $\sin \varnothing/d$, while the density along the azimuthal direction is $\cos \varnothing/d$ [93]. By decomposing the magnetic field contributions from each loop, the magnetic flux density per unit current can be determined for both the solenoid and dipole fields, as expressed in Equations 4.1 and 4.2 respectively [86].

$$X_x = \frac{u_0 \cos\varnothing}{d} \tag{4.1}$$

$$X_z = \frac{u_0 \sin\varnothing}{2d} \tag{4.2}$$

When the two coils are fed the same currents in opposite directions, the solenoid fields cancel, while the dipole fields are reinforced. The solenoid transfer function of the outer coil will be opposite to the inner coil, $X_{xi} = -X_{xo}$, while the dipole transfer function remains constant $X_{zi} = X_{zo}$. The resulting dipole magnetic field is characterised by magnetic flux density $B_z$ , and current, $I$, as shown in Equation 4.3 [86] [93].

$$B_z = \frac{u_0 I}{d} sin(\varnothing) \tag{4.3}$$

The cancellation of the solenoid field component by concentric coils with opposite current flow is accomplished if the axial turn spacing is the same in each layer with the same number of turns [92].

This section focuses on examining the field lines created by different tilt angles, the inclusion of steel cores, and the current magnitude and direction. Thereafter, the coil configuration is optimised to produce sufficient force to move a small magnetic block in the horizontal and vertical directions.

### 4.2.3 Actuator Design

Design requirements have been identified to verify the performance of the DH as an actuator. (1) The DH must produce sufficient force to move a small magnetic block. (2) The force direction must be controllable by the current. (3) The DH must be able to induce four directions of motion on the magnet. Based on the design requirements, a DH coil is developed. To produce a bidirectional force on the magnetic block, the magnetic fields should be capable of producing the following properties. (1) Vertical field in both directions, with near zero horizontal fields, (2) horizontal field in both directions, with near zero vertical fields. With the primary goal of maximising the force generated in the dipole field. The field strength and direction of rectangular and elliptical-shaped DH coils were simulated and compared in ANSYS. The rectangular and elliptical DH consists of an inner and outer coil in a rectangular and elliptical shape shown in Figure 4.2.

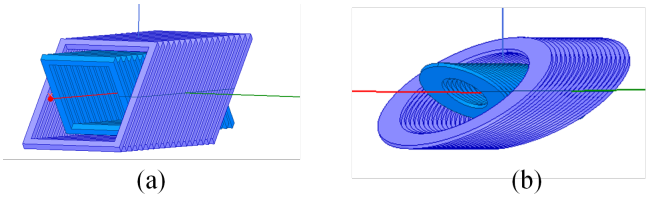

(a) (b)

Figure 4.2: The DH coil structure: (a) Rectangular Coil (b) Elliptical Coil

## 4.3 Simulation of DH Actuator

Modelling the DH actuator was conducted using ANSYS Maxwell in Magnetostatic mode. The simulations aimed to determine the magnetic field strength and direction with varying tilt angles and different current direction combinations on a rectangular and elliptical coil. Further simulations analyse the effect of including a steel core and lastly the force experienced by a magnetic block. The objective of the simulations was to determine the optimal geometry to achieve bidirectional movement of the permanent magnet block, therefore validating the DH as an actuator. Figure 4.3 shows the variables and structures within the DH, the inner and outer coils, the steel core, and the magnet. The variables referred to are defined in Table 4.3.

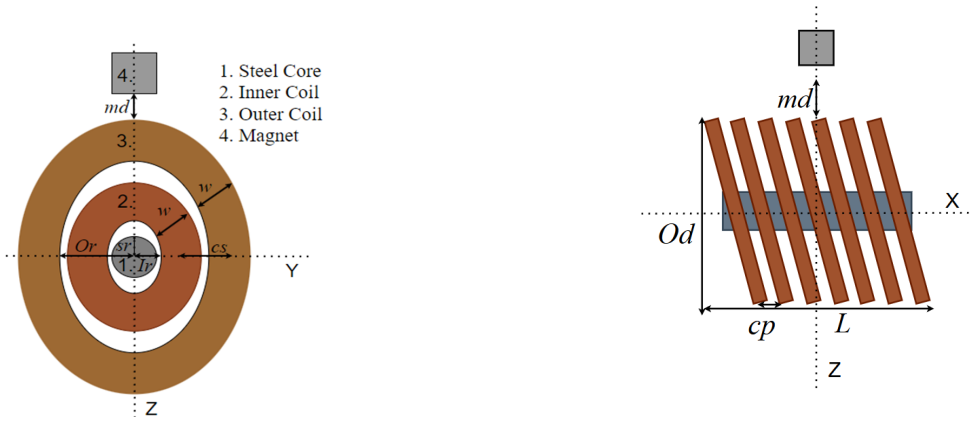


(a) X-axis View (b) Y-axis View

Figure 4.3: The DH coil Parameter Diagram

Table 4.3: Variable Specifications and Optimizations

| **Parameters** | **Range** | **Optimised 60°** | **45°** |
|---|---|---|---|
| Magnet(xsize_mm) | 5-10 | 10 | 10 |
| Magnet(ysize_mm) | 5-10 | 9 | 10 |
| Wire Width (w_mm) | 6-10 | 9.2 | 10 |
| Coil Separation (cs_mm) | 6-18 | 13 | 11 |
| Coil Angle ($\phi$°) | 0-60 | 60 | 45 |
| Inner Radius (Ir_mm) | 5-10 | 7 | 4.5 |
| Outer Radius (Or_mm) | Ir+w+3 | 19.2 | 16 |
| Coil Pitch (cp_mm) | 2-5 | 3.4 | 2.4 |
| Magnet Distance (md_mm) | 0-20 | 5 | 5 |
| Steel Radius (sr_mm) | 0.5-5 | 2.5 | 0 |
| Current ($I_i$, $I_o$ A) | 5-40 | 30 | 30 |
| Force (N) | >0 | 0.48 | 0.3 |
| Length (mm) | <130 | 117 | 70 |

### 4.3.1 Magnetic Field Simulations

Simulations were conducted to observe the behaviour of the magnetic field of the DH coil at different angles with opposite currents in each coil. The simulations revealed that a magnetic field perpendicular to the coil axis is generated. This field is at its strongest when the coil's windings are tending to 60°. This occurs due to the cancellation of the magnetic fields along the coil's axis (X-axis), allowing the perpendicular field to dominate. The simulations demonstrate that the DH coil can produce a vertical magnetic field with near-zero solenoid field interference.

The main objective was to enhance the force in the dipole region, which in turn decreases the force in the solenoid direction due to the tilt angle. A steel core was introduced to amplify the solenoid field. Simulations were conducted to observe and compare the magnetic field strength generated by the rectangular and elliptical coils and the effect of including a steel core. Figure 4.4 illustrates that both rectangular and elliptical DH coils produce similar magnetic field strengths when no core is present. However, when a steel core was introduced, the elliptical DH coil generated a stronger magnetic field than the rectangular coil. Additionally, the simulations revealed that in both coil types, magnetic field strength increases with the tilt angle, confirming that solenoid fields are cancelled at 0° tilt and dipole fields are progressively added as the angle increases when the current is driven in opposite directions in the inner and outer winding.

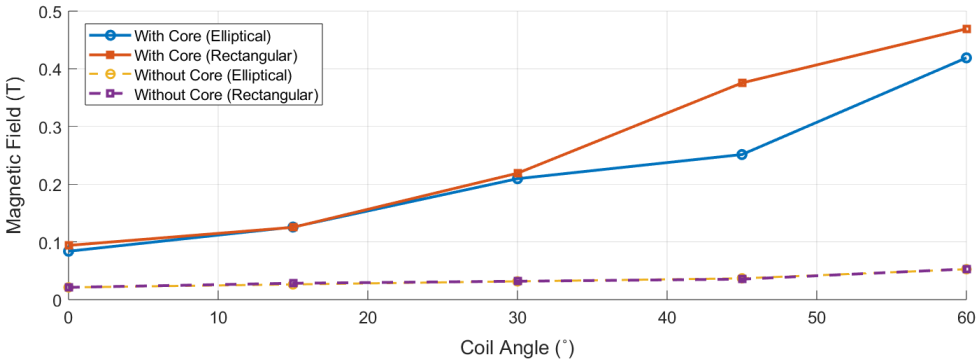


Figure 4.4: Magnetic fields of the elliptical and rectangular coil with and without a steel core

### 4.3.2 Forces

The primary objective of this section is to investigate the force generated in the dipole direction, as the force in the solenoid direction is easily obtained. Simulations were conducted to determine the force exerted on a permanent magnet block in the dipole (Z) direction for both rectangular and elliptical DH coils at various tilt angles.

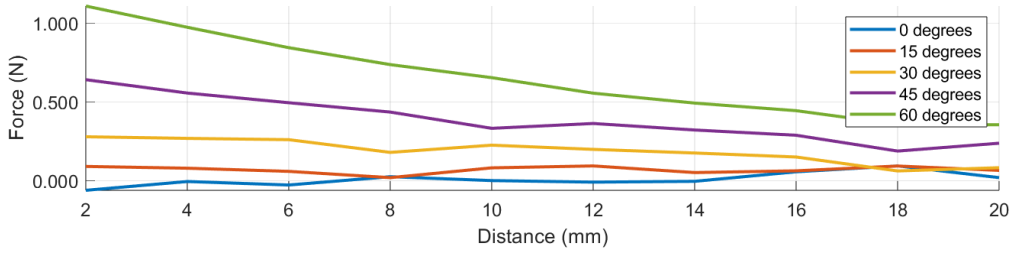


(a) Rectangular

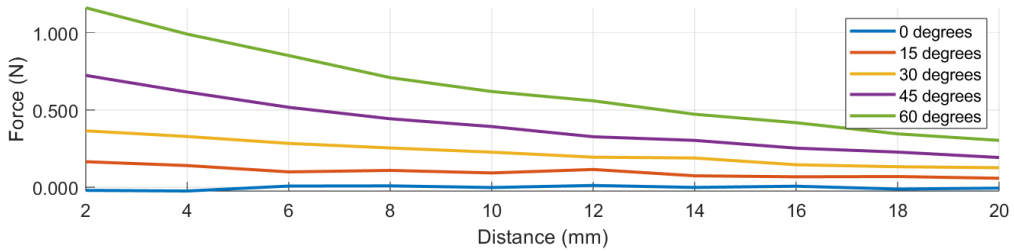


(b) Elliptical

Figure 4.5: Force per Magnet Distance at Various Tilt Angles for Rectangular and Elliptical Coil Shapes

Figure 4.5 indicates that the force exerted on the permanent magnetic block in the dipole direction decreases as the magnet block moves further from the coil, $m_d$. Furthermore, the force exerted on the block increases as the coil angle increases for both DH coils. Notably, the force at the 60° tilt angle is considerably larger than at other angles. Due to the elliptical DH coil configuration producing a greater and smoother force in the dipole direction, this coil was selected for optimisation and implementation.

## 4.4 Optimisation and Simulation Results

Optimisation of the DH coil design involved a sensitivity analysis followed by optimisation using an evolutionary algorithm in ANSYS Workbench.

### 4.4.1 Sensitivity Analysis

The sensitivity analysis aimed to identify the design variables that most significantly impacted the force exerted on the magnet in both the dipole and solenoid directions. Simulations were run with opposite current directions for the dipole field and the same direction for the solenoid field. The design variables shown in Table 4.3 were used in the sensitivity and optimisation analysis with their respective ranges. Table 4.3 summarises the parameters of the optimised 60-degree DH and a comparative non-optimised 45-degree DH coil. Table 4.4 summarises the sensitivity analysis results for the DH coil configuration for the X and Z directions.

Table 4.4: Sensitivity Analysis Results

| **Magnet (%)** | | | | | **Coil (%)** | | | | |
|---|---|---|---|---|---|---|---|---|---|
| **F** | **Z** | **X** | **md** | **Ir** | $deg°$ | **cs** | $I_i$ | $I_o$ | **sr** |
| Z | 0.8 | 12.9 | 6.1 | 1.5 | 40.1 | 12.7 | 4 | 41.3 | - |
| X | 11.9 | 10.5 | 16.8 | 7.8 | 1 | - | 3.1 | 11.3 | 37.3 |

The sensitivity analysis showed that for the Z-axis (dipole direction), the outer coil current has the most significant impact on the force applied to the magnet block, contributing 41.3%, followed by the coil angle, $\phi$, 40.1%, and the magnet size in the x direction, X, 12.9%. The reliance on the coil angle for the dipole force is primarily due to the cancellation of the magnetic fields in the solenoid direction and their reinforcement in the dipole direction. As the coil tilt angle increases, the magnetic field in the dipole region strengthens, reducing the need for cancellation along the X direction. In contrast, the force in the X-axis (solenoid direction) is primarily influenced by the steel radius at 37.3%, the distance between the magnet and the DH, 16.8%, followed by the magnet size and the outer coil current.

### 4.4.2 Optimisation

The optimisation of the DH configuration was performed as a multi-objective optimisation, focusing on maximising the force on the magnet while minimising the volume of the DH coil, which is critical for reducing the volume, weight, and cost of the actuator.

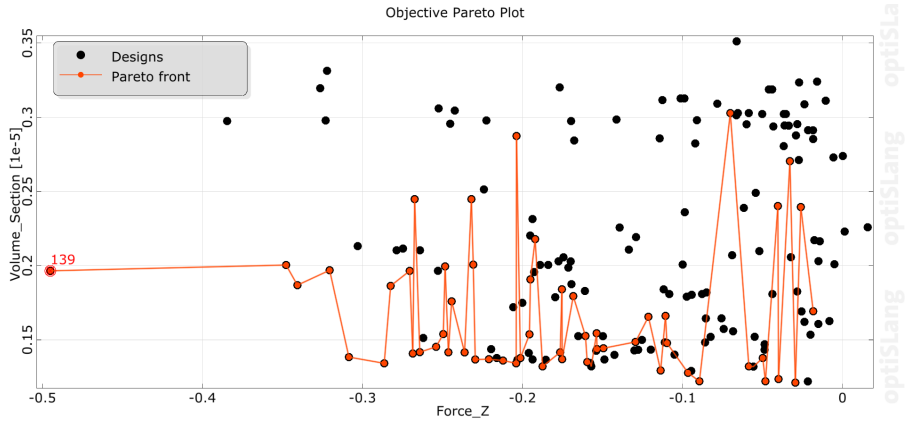


Figure 4.6: DH Pareto Plot: Optimised Designs

Figure 4.6 illustrates the optimisation results in the form of a Pareto plot, which highlights the trade-off between force and volume. Since the primary objective was to maximise the force in the dipole direction, the design that generated the highest force was selected for implementation. This approach ensures that the design delivers the desired magnetic performance and maintains a compact form. Table 4.3 summarises the variables associated with this design.

## 4.5 Implementation and Experimental Results

### 4.5.1 Force Measurement Experimental Setup

The non-optimized model (45-degree coil) and the optimised model (60-degree) coil were implemented and compared. Table 4.3 summarises the coils' dimensions. The coils were wound with 800 turns of 0.45 mm wire and held at their respective angles by 3D-printed PLA plastic frames. The magnet type was ND42. The force exerted on the magnet block was measured experimentally to validate the simulations. Figure 4.7 shows the experimental setup for the force measurement. A dual-range force sensor measured the force exerted on the magnet in both directions at various distances.

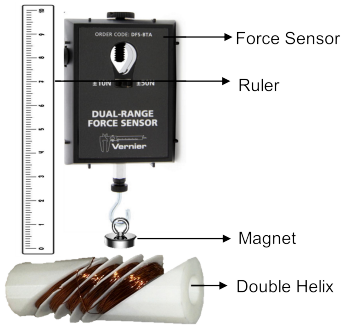


Figure 4.7: DH Practical Setup with Dual Range Force Sensor

Figure 4.8 shows the results of the simulated and experimentally measured forces for both DH coil configurations. Figure 4.8 shows the force exerted on the permanent magnet by the 60° DH coil with a core where the simulated and measured forces were comparable in the Z (dipole direction).

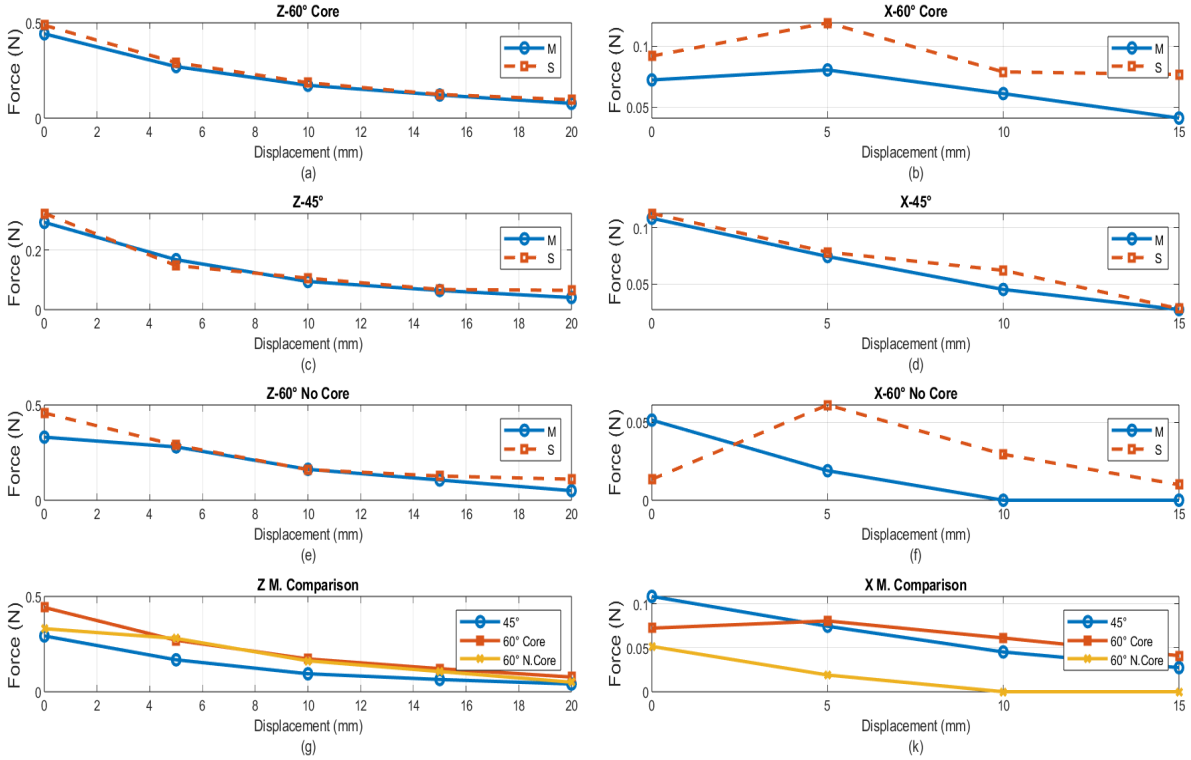


Figure 4.8: 60° and 45° DH measured (M) and simulated (S) force comparison

However, there was some deviation in the X (solenoid direction), where the simulations predicted higher forces than were measured, as shown in Figure 4.8 (b). As expected, the solenoid force is significantly lower than that in the dipole direction since the design was optimised for the maximum force in the dipole field. The discrepancy between measured and simulated forces likely arises because the simulation assumes an ideal distribution of the winding and core within the solenoid field. In practice, the windings may not interact effectively with each other and the core. Despite the same number of turns being used in each coil, slight variations in the turn distribution can affect the cancellation or addition of magnetic fields in practice, an outcome that is avoided in simulations.

It is important to note that when the core is removed from the 60° coil, the solenoid's field force is significantly reduced, as illustrated in Figure 4.8 (b) and (f). This observation indicates that the force generated by the 60° DH in the solenoid direction is primarily due to the cores permeability, which confirms the sensitivity analysis results. The discrepancies between the simulated and measured results without a core can be attributed to the force sensor's resolution limit of 0.01 N. Nevertheless, the results validate the sensitivity results, which showed that the solenoid force is highly dependent on the steel core's radius, while the core has little impact on the dipole force. This is further demonstrated by the comparison between measured and simulated forces in the 60° DH Figure 4.8 (a) core and (e) no core, where there was no significant difference in forces.

In contrast, the 45° DH coil produces lower forces in the dipole direction than the 60° DH coil and stronger solenoid forces. This suggests that the 45° coil with no core generates solenoid forces more effectively than the 60° coil. This is expected as the magnetic field in the solenoid direction is more concentrated at 45° than 60°. However, including the steel core in the 60° compensates, increasing the solenoid field by 0.08N. Figure 4.8 (g and h) shows the measured forces in the Z and X directions of all three coil versions, highlighting that the 60° coil outperforms the 45° coil in the Z direction, and only

with a core becomes comparable in the X direction at 5mm magnet displacement.

### 4.5.2 Thermal Analysis

Thermal analysis was conducted in ANSYS Icepak to evaluate the thermal resistive loss of the DH coil at various currents (0.2A,0.4A and 0.6A) for both the inner and outer coils, both separately and combined. The simulation results were validated against experimental data, which involved removing the core and monitoring the temperature changes at each current level over five minutes. The experiment was repeated with the inner coil placed inside the outer coil, indicating the thermal contribution of each coil individually and additionally. Temperature measurements were taken using a thermal gun and Testo Thermal Imager.

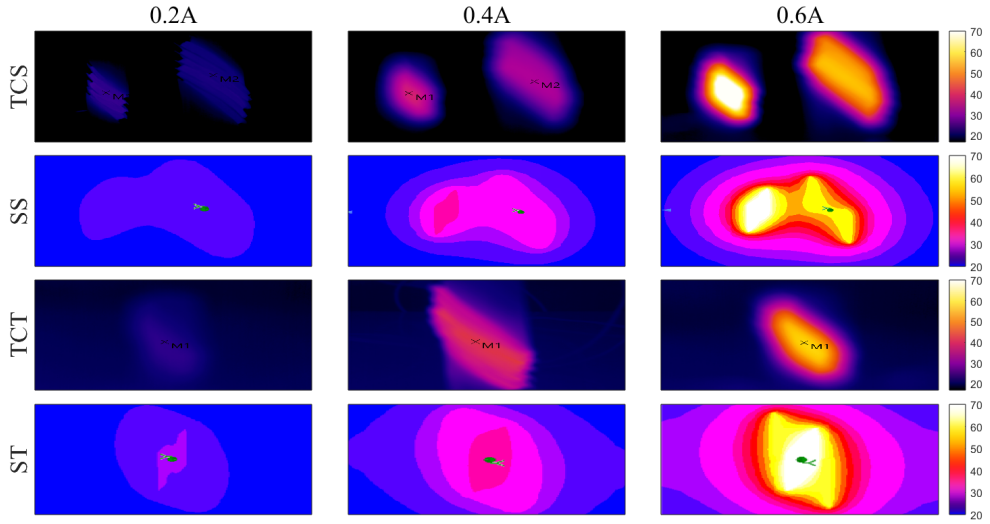


Figure 4.9: Thermal analysis results from thermal camera separately (TCS), simulation separately (SS) and thermal camera together (TCT) and simulations together (ST). The range of temperatures for each row is indicated by the thermal colour bar.

As the temperature of the coils increases, their resistance increases, necessitating adjustments in the applied voltage to maintain the target current. This relationship between the resistance and temperature was documented, providing insights into the impact of thermal behaviour on the resistance. Figure 4.9 illustrates the temperature variation of each coil after five minutes of testing. The experimental results show that the inner coil reaches the highest temperature at 76°C for 0.6 A, followed by the combined coils, 62°C, and finally, the outer coil at 60°C. This trend can be attributed to the inner coil operating at the same current as the outer coil but confined within a smaller volume, leading to greater heat accumulation due to less ventilation.

In contrast, the outer coil, with its larger inner radius, dissipates heat more effectively. For the combined coil, experimental temperature measurements were influenced by the outer coil. The placement of the inner coil inside the larger coil obscures its temperature from the thermal camera. Consequently, the temperature readings from the outer coil dominate the combined experimental measurements. The thermal simulations closely match the thermal camera results throughout the current levels, with the simulations calculating the inner coil at 70°C for 0.6 A, and the outer coil at 57°C. However, the simulations accounted for the inner coils' temperature contribution in the combined setup, resulting in a higher combined temperature than the experimental results, at 65°C.

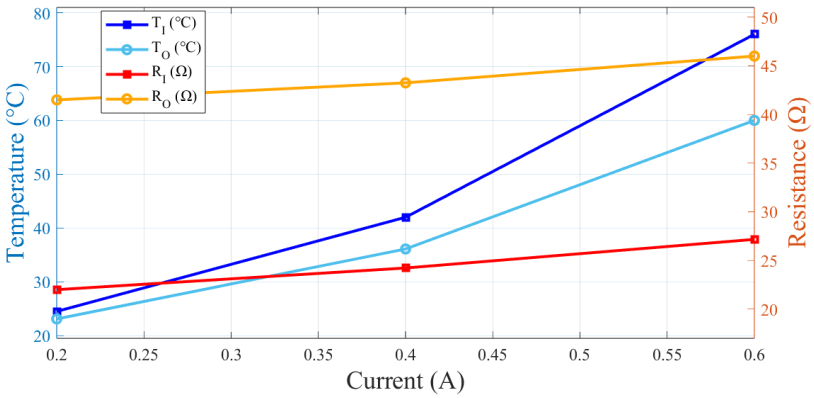


Figure 4.10: Temperature and Resistance of the Inner and Outer coil.

Figure 4.10 shows the simultaneous increase of the temperature and resistance over the five-minute test period. This correlation shows the role that resistance plays in temperature increase, highlighting its importance in the thermal management of electromagnetic actuators. The temperature increase in the coils is a critical validation for electromagnetic actuators that is often overlooked. Notably, the thermal results indicate that the coil does not experience overheating , which is crucial for the longevity of the coil system.

## 4.6 Discussion and Conclusion

The DH produces sufficient force to move a small magnetic block in four directions, with the force direction being controllable by the current, therefore achieving the design requirements and proving the effectiveness of the DH as a potential actuator. The sensitivity analysis revealed that the outer coil current and tilt angle had the most significant impact on the dipole force. In contrast, the solenoid force was highly dependent on the steel core's radius, which was supported by the simulation and the experimental results. The force measurements demonstrated that the DH's tilt angle significantly influences the resulting force, particularly in the dipole direction. As the tilt angle increased, the solenoid force strength weakened, but this reduction was compensated by including a steel core. The 60° tilt angle proved to be the optimal configuration, generating a stronger dipole force than the 45° coil. The force exerted on the magnet block in the dipole and solenoid direction were both affected by the distance of the magnet to the coil; this suggests the control of magnetic material needs to occur near the DH configuration. Despite the slight discrepancy in the simulation and experimental force results due to manufacturing variations and sensor limitations, the cancellation of the solenoid field component by pairs of complementary concentric coils with the opposite current flow was accomplished. The thermal analysis highlighted the importance of adequate ventilation in maintaining coil performance. These results emphasise incorporating thermal management strategies in future DH coil designs to ensure operational longevity.

This section demonstrates the effectiveness of the DH coil as a versatile actuator capable of multidirectional actuation with two DOFs, marking a significant improvement over traditional single-axis coil systems. The DH design optimises volume reduction and force to enable magnetic manipulation from a compact design. Simulations and experimental results confirm that the 60° DH generates a force in four directions by controlling the current direction. The DH actuator's ability to produce both vertical and horizontal magnetic fields makes it an ideal actuator for wireless control of magnetic devices.

Magnetic actuation continues to reveal potential use cases and improvement, providing increased DOF from more compact coil designs.

Despite the DH actuator providing forces in two directions, its application as a spinal actuator was not implemented. This is due to the DH providing a limited displacement of the magnet and the requirement for proximity of the magnet for strong forces. The use of electromagnetism, however, was highlighted as an effective method of achieving fast and accurate movement, with the directionality of displacement adjustable. The overall spinal segment system needs to achieve 6 DOF. Therefore, the individual structure must maximise its DOF to ensure that 6 DOF is capable when combined. The spinal actuator requires a large displacement or stroke length. Therefore, the design of an electromagnetic solenoid plunger was been explored.

# Chapter 5

# Linear Electromagnetic Actuator: Solenoid Plunger

Linear solenoid electromagnetic actuators are used in a range of applications due to their ability to provide precise linear motion through simple control mechanisms [19]. Their movement is achieved through the extension and contraction of a permanent magnet within a solenoid coil, and is controlled by the direction and amplitude of current. The simple, compact design and fast response make them suitable for applications requiring efficient and adaptation movement. However electromagnetic actuators are prone to heating, and therefore their optimisation is imperative [65]. The critical variables contributing to the performance of the actuator are the coils current, the number of turns, the dimensions of the solenoid, the material properties of the magnet and effective thermal management.

Due to the inherent simplicity of the linear solenoid plunger, the system can be easily scaled, ensuring it can be integrated into larger systems. In addition, the modularity of the linear solenoid actuator makes them particularly suited for applications requiring multiple actuators working coherently, such as in a robotic spinal segment.

## 5.1 Design and Optimisation of a Solenoid Plunger

The literature in Section 3.1.1 highlighted the benefits of solenoid plungers or voice coils as a form of electromagnetic actuation [20] [63] [57] [19]. The combinations of fast response, high force-to-volume ratio, and configurable stroke length make this actuator ideal for a linear actuator capable of implementation in a parallel spinal system.

The system requirements (SR) have been identified as follows:

SR.1 EM System capable of three degrees of freedom.

SR.2 Sufficient stroke length for vertical movement (>Plunger Length).

SR.3 System capable of modulation.

SR.4 System capable of scalability.

SR.5 System capable of connection in a parallel configuration.

SR.6 Sufficient force (maximising force) to support its weight and an additional load.

SR.7 Minimising Volume.

SR.8 System capable of longevity.

SR.9 Low power requirements.

SR.10 Thermal Management.

SR.1 requires that the linear actuator be capable of 3DOF. This requirement ensures that the system has a sufficient range of motion to achieve the basic movement within a spine: extension and rotation. SR.2 stems from SR.1, the ability of the plunger to extend enables the vertical movement of the actuator, which facilitates another DOF in the spinal structure. Furthermore, due to the extension of the plunger being the movement that would enable rotation and bending, with the length of the stroke being the limiting factor, the length is required to exceed the length of the plunger. This ensures maximum bending and rotational angles are achieved. To integrate the system into the 6 DOF spinal actuator, the actuator requires adaptability and controllability, SR.3, ensures that the system is capable of this modulation. In addition, SR.4 considers that the actuator system would need various force and size specifications, providing scalability. SR.5 summarises SR.3 and SR.4 and makes sure that the actuator is capable of implementation in a parallel configuration, that is, the spinal manipulator. SR.6 and SR.7 are attributed to the optimisation and design of the actuator, ensuring that the maximum force is produced and is able to overcome its weight whilst minimising the volume and, therefore, the weight of the system. The two conflicting objectives play a crucial role in the design of the system, ensuring that its performance is optimal and efficient, which are desirable characteristics in spinal robot actuators. Other characteristics, such as longevity SR.8 and low power requirements SR.9, enhance the system's performance, feasibility and durability. The final requirement SR.10, thermal management, is an overlooked element in the design of actuators and is essential to EM actuators as they are prone to heating. SR.8, SR.9, and SR.10 demonstrate the capabilities of EM actuators and provide validations for their suitability as spinal actuators. From these SR; the system would ensure high performance, low cost, durability and lifespan.

Once a thorough analysis of the literature had been conducted, the overall design and mechanics of the system were established based on the system requirements. Figure 5.1 shows a flow chart of the steps (S1-S11) taken in the design of the linear electromagnetic solenoid plunger.

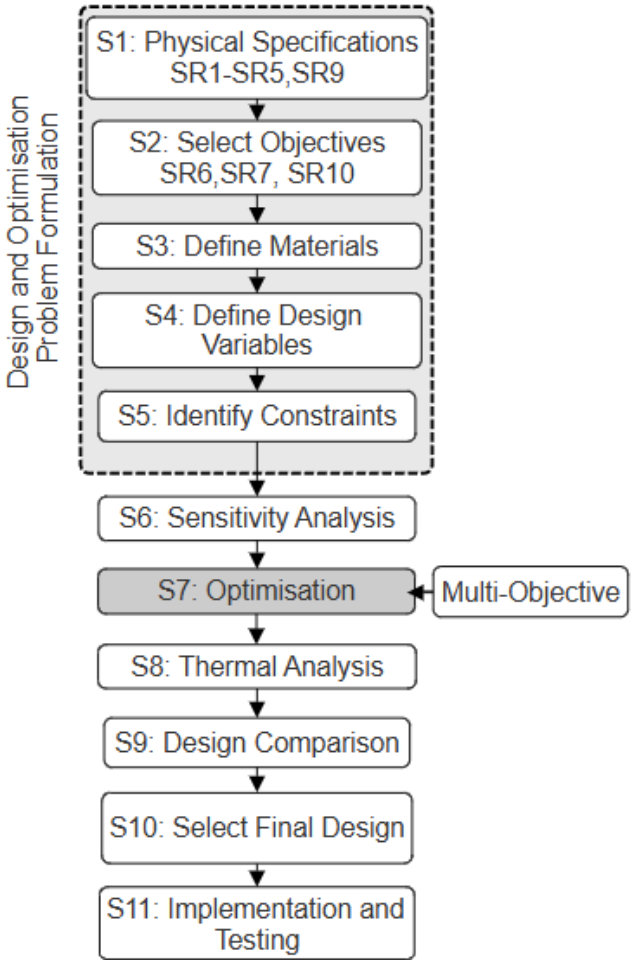


Figure 5.1: EM Actuator Design Methodology

The steps (S1-S5) in Figure 5.1 initiate the design and optimisation problem formulation and use the SR as references. Each step is elaborated on in the following sections.

### 5.1.1 S1-3: Mechanical Design

The mechanical design of the solenoid plunger elaborates on S1-S3 of the design and optimisation problem formulation shown in the flowchart in Figure 5.1. The design is based on the System Requirements listed in section 5.1. The solenoid plunger system consists of three main parts: the magnet-plunger system, the solenoid, and the connectors, which attach the solenoid base and the magnet end to a base and top platform, respectively. Each solenoid plunger requires movement capabilities in 3 DOF.

Figure 5.2a shows a fully assembled solenoid plunger system, which is deconstructed into parts shown in Figure 5.2b. The permanent magnet's end and the solenoid's base are attached to a universal joint connector as shown in fig 5.2b Part 1. Connecting two universal joints with steel bolts enables the movement of the solenoid in 2 DOF, roll and pitch. A PLA bobbin binds the solenoid illustrated in 5.2b Part 5; this bobbin ensures that the coil winding remains compact. The permanent magnet lies within the solenoid and is prevented from extending further than the solenoid bobbin length by a PLA plastic stopper attached to the base of the magnet. The magnet can extend or contract, producing another DOF. The top universal joints have the same functionality as the base connector.

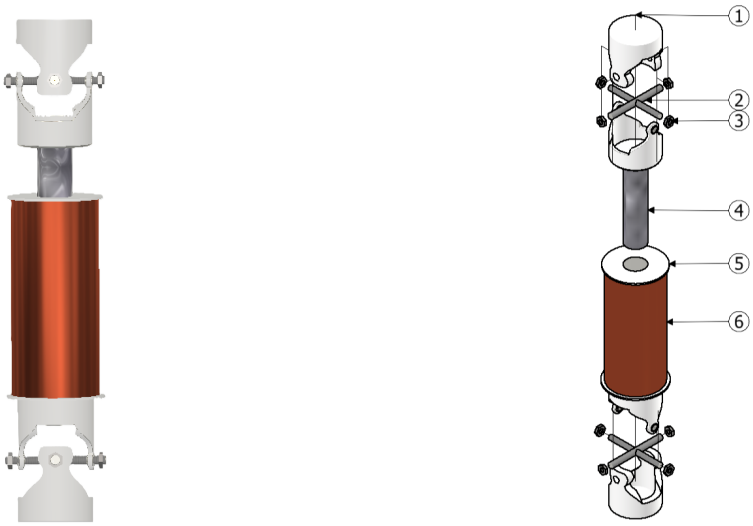


(a) Single Solenoid Visual

(b) Single Solenoid Parts

Figure 5.2: Single Solenoid Design: 1 - PLA Connector, 2 - Steel Universal Joint, 3 - Steel Nut - 4 - Magnet, 5 - PLA Bobbin, 6 - Copper Solenoid

A neodymium magnet is chosen as the plunger material (Part 4), with a copper solenoid surrounding it (Part 6). A strong adhesive glue binds The PLA connectors to the solenoid and permanent magnet. 1 mm steel nuts (Part 3) attached to the steel universal joint (Part 2) ensure the system's rigidity, while the buffer created by the PLA connectors prevents magnetic interference with the permanent magnet. The magnet is housed within a PLA support sleeve (not shown in figure 5.2). A clearance fit between the sleeve and the solenoid and a silicone lubricant coating on the sleeve enables the magnet to move freely without friction.

The literature in Section 3.2 highlighted the importance of analysing the dynamics and electromagnetic force within the system in the design procedure [65]. The numerical analysis of the forces involved verifies the system's requirement to overcome the magnet's weight and indicates the maximum loads that can be added. The analysis further highlights design parameters within the system that contribute the most to maximising force and minimising the volume.

## 5.2 S4: Analysis of Electromagnetic Force

The electromagnetic force generated by the solenoid plunger system is required to overcome the weight of the magnet and an applied load. The variables contributing to the system's force and volume are analysed using theoretical calculations, Finite Element Analysis (FEA) simulations, and optimisation algorithms.

### 5.2.1 Theoretical Analysis

Two forces are exerted in the plunger system: the electromagnetic force induced by the magnetic field inside the solenoid when current flows and the magnetic force caused by a permanent magnet plunger. Figure 5.3 and the following equations analyse the combined force produced by the solenoid and the plunger.

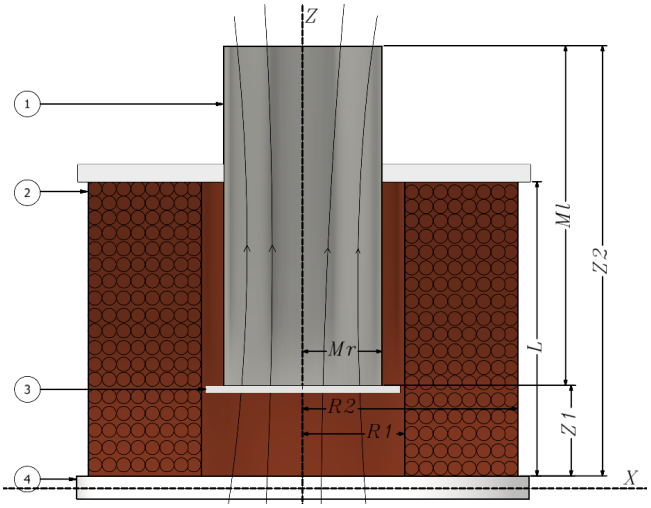


Figure 5.3: Solenoid Plunger and Magnetic Field Diagram: 1 - Magnet, 2 - Solenoid, 3 - PLA Magnet Stopper, 4 - PLA Bobbin

In Figure 5.3, $z_1$ and $z_2$ represent the lower and upper end of the magnet along the Z-axis. $R1$ and $R2$ indicate the outer and inner radius of the solenoid, $L$ is the length of the solenoid, $Ml$ is the length of the magnet, and Mr is the magnet's radius.

For the following equations, $B_0$ represents the magnetic induction of the magnet. $B_{z2}$ and $B_{z1}$ represent the magnetic field contributions of the coil on the upper and lower surfaces of the magnet.

The axial electromagnetic field can be calculated by adapting the Biot-Savart Law as shown in equation 5.1 [19].

$$F_{B_z} = \frac{B_0 n^2 I}{2} \int_0^{Mr} \int_{R_1}^{R_2} \int_0^{2\pi} \int_0^{L} (M_r R^2 - M_r^2 R \sin\theta)[\frac{1}{r(z_1)^3} - \frac{1}{r(z_2)^3}]\, dz\, d\theta\, dR\, dM_r \tag{5.1}$$

Equation 5.1 shows that the electromagnetic force is proportional to the magnetic induction of the magnet and the input current of the solenoid. From this, it is assumed that the magnet induction is the same across each magnet cross-section, eliminating the quadruple integral. The assumption simplifies equation 5.1 into equation 5.2.

$$F_{B_z} = \frac{B_0 n^2 I \pi M_r^2}{2}[\phi_B(z_1) - \phi_B(z_2)] \tag{5.2}$$

Where $\phi_B$ is the magnetic field interaction between the upper and lower surface of the magnet, equation 5.3 shows $\phi_B$, where $z$ is the height of the upper or lower surfaces of the magnet relative to the base of the solenoid, and $L$ is the length of the solenoid.

$$\phi B(z) = z \ln\left(\frac{R_2 + \sqrt{R_2^2 + z^2}}{R_1 + \sqrt{R_1^2 + z^2}}\right) + (L - z) \ln\left(\frac{R_2 + \sqrt{R_2^2 + (L-z)^2}}{R_1 + \sqrt{R_1^2 + (L-z)^2}}\right) \tag{5.3}$$

From the equations 5.3 and 5.2, the parameters affecting the force on the magnet can be identified. The electromagnetic force from the solenoid actuator is proportional to the change in inductance of the coil

with respect to the change in the position of the Permanent Magnet (PM) plunger as well as the current flowing through the coils [21] [20]. The solenoid force, therefore, depends on the design parameters of both the solenoid and PM, which include the inner and outer diameter of the solenoid, the number of turns, the airgap, solenoid length, input current, permanent magnet length and radius, its initial displacement in the solenoid and the remanence. Equation 5.1 further highlights the importance of the current in the coil, as it is proportional to the electromagnetic force. The voltage applied and the coil's resistance determines its current, where higher currents result in larger forces, effectively increasing the magnet's travel speed. The parameters discussed need to be optimised to maximise the force per volume of the plunger system. The solenoid plunger force must overcome the magnet's weight and enable the plunger's linear motion.

Equation 5.3 and 5.2 form the analytical solutions for the solenoid and magnet system. The analytical solutions identify the parameters affecting the force and volume of the system; however, when used in isolation, they cannot optimise the configuration of the solenoid and PM. Therefore, they supplement and verify Finite Element Analysis (FEA) optimisations in the simulation software ANSYS Maxwell.

The solenoid plunger actuator generates axial force through the interaction between the magnetic field produced by the solenoid coil and the permanent magnet plunger. The magnetic field intensity within the solenoid can be approximated using Ampère's Law:

$$B = \mu H = \mu \frac{NI}{l_m}, \tag{5.4}$$

where $N$ is the number of turns, $I$ is the coil current, $l_m$ is the effective magnetic path length, and $\mu$ is the magnetic permeability of the magnetic circuit. The electromagnetic force can be expressed using the magnetic co-energy method:

$$F = \frac{dW_c}{dx}, \tag{5.5}$$

where $W_c$ is the magnetic co-energy and $x$ is the plunger's displacement. For an axisymmetric structure with a uniform air gap, the force is given by:

$$F = \frac{B^2 A}{2\mu_0}, \tag{5.6}$$

where $A$ is the effective flux cross-sectional area and $\mu_0$ is the permeability of free space. Substituting for $B$ yields:

$$F = \frac{\mu^2 (NI)^2 A}{2\mu_0 l_m^2}. \tag{5.7}$$

This expression indicates that the force increases quadratically with both current and coil turns, and decreases with increasing magnetic path length. Therefore, the air gap length, magnet geometry, and bobbin dimensions are important variables in determining optimal actuator performance. These relationships informed the initial design bounds prior to finite element simulation and optimisation.

### 5.2.2 S4: FEA Analysis

Adding FEA simulations to the solenoid plunger analysis enhances its validity and enables the navigation of the design variable's trade-offs. The FEA simulations were conducted in Ansys Maxwell Electronics Magnetostatic mode for the solenoid forces and Transient mode for time-dependent simulations.

From Equation 5.1, the current can be identified as one optimisation parameter. The current in the coil is dependent on the wire diameter and follows the AWG table shown in Figure B.1 in the Appendix. Due to the wire diameter determining the maximum permissible current before overheating and the resulting solenoid volume, its selection was analysed first. The wire diameter and the resulting current are fixed variables in the FEA simulations and correspond to the resulting turns, solenoid diameter, solenoid length, magnet diameter, magnet length and force produced. To reduce the design space and determine the optimal parameter configuration of the solenoid plunger, a wire diameter and corresponding current were isolated and selected.

Six wire diameters and their associated currents are simulated and optimised to determine the most suitable wire. The top four designs for each wire diameter are then compared against one another according to their maximum force, average force over the magnet stroke length, force to volume and thermal analysis. The objective comparison indicates which wire diameters produce the highest force per volume over the stroke length of the magnet whilst dissipating heat effectively. These objectives adhere to the design requirements of thermal management, maximising force, minimising volume and producing a stroke length.

The wire diameters 0.153 mm, 0.2 mm, 0.335 mm, 0.45 mm, 0.56 mm, and 0.6 mm wire are chosen for optimisation based on availability and standard sizes. The wire width was also limited by the ease of winding, in which 0.6 mm was deemed the limit. A sensitivity and optimisation analysis in ANSYS Workbench is conducted for each wire diameter, with the goal of the simulations being to determine which wire diameter and variable combination would be the most optimal for the actuator design. Each wire diameter was simulated with the same simulation parameters over the same ranges, with the sole difference being the wire diameter and the corresponding current.

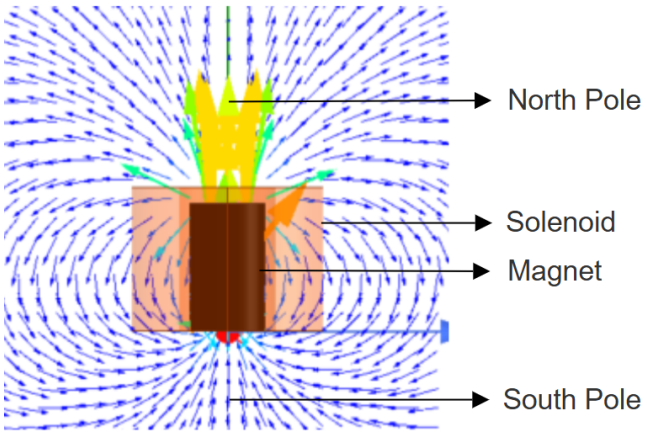


Figure 5.4: Solenoid-Plunger Simulation Diagram and Magnetic Field

Figure 5.4 shows the complete solenoid plunger model with the variables of each component highlighted in Figure 5.3. The solenoid was modelled as a solid cylinder to reduce the simulation time, while mesh refinements were included to improve the accuracy of the results.

Before optimising the wire diameter of the solenoid, variables within the solenoid and PM that contribute to the volume and force produced need to be restricted to achieve the design requirements. Based on the desired size of the complete assembly, the width and length of the solenoid were limited to 50mm, with a body width of 35mm, respectively.

## 5.3 S5: Variable Selection

To optimise each variable, their ranges were restricted. The following sections highlight the steps to determine these restrictions and consider each variable's trade-offs. The variable selection initiates step four and five (S4 and S5) in the flowchart shown in Figure 5.1.

### 5.3.1 Solenoid Coils

The literature in Section 3.1.1 highlighted the complications involved in increasing the magnetic field while minimising the overall size and weight of the system [19]. Increasing the number of turns in the solenoid compensated for the limitations of the current due to wire size. However, the increase in solenoid turns increased the solenoid's length or width, increasing the volume.

Table 5.1: Declared Variables

| **Variable** | **Equation** |
|---|---|
| **Turns/Layer** | $lengthsolenoid/coilwidth$ |
| **Coil Width** | $layers \times wirediameter$ |
| **Solenoid Length** | $(\frac{turns}{Layers}) \times wirediameter$ |
| **Outer Radius** | $coilwidth + InnerRadius$ |
| **Total Face Current** | $current \times turns$ |
| **Magnet Radius** | $InnerRadius - 2mm$ |

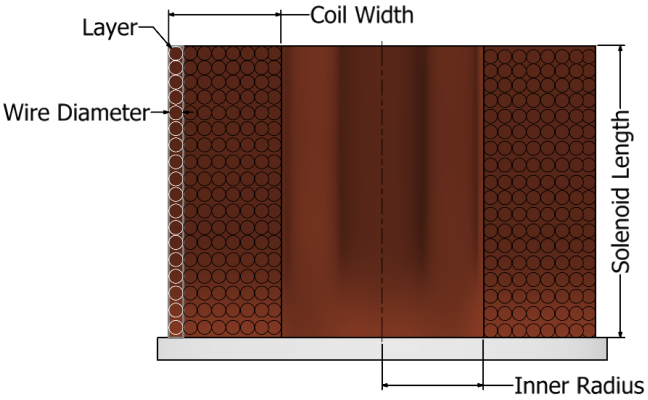


Figure 5.5: Declared Variables Diagram

The variables in table 5.1 allowed the specifications of the designs to be described, which guided the design comparison and prototype building process. The layers referred to are the radial layers of turns forming the solenoid width, while the turns determine the height of the solenoid. These variables are used in conjunction to limit the overall height of the solenoid.

Therefore, the solenoid's length needs to be limited to optimise the force per unit volume. The length of the solenoid was limited to 50 mm due to manufacturing limits, and relative proportion to a spinal segment. The length of the solenoid was further limited based on the theoretical analysis, enabling the platform to achieve the design deflection angles without perpetually increasing in size. The restriction of the solenoid length aimed to increase the force-per-cross-section ratio, where compact coils produce a more concentrated force. Due to the length restriction, the increase in the number of turns was implemented in the form of layers. To calculate and compare the volume of the solenoids concerning

their layers and wire diameters, additional variables were declared and are shown in table 5.1.

The solenoid's inner radius will determine the PM's radius and the air gap formed between the two. A parametric simulation was conducted to observe this relationship where the magnet's radius was kept constant, and the inner radius of the solenoid increased. Figure 5.6 shows the force as the air gap between the magnet and the solenoid increases.

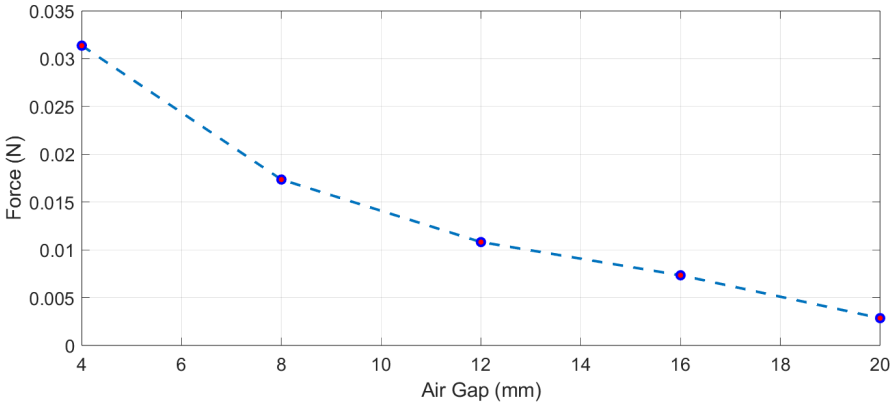


Figure 5.6: Force over Air Gap increase

Figure 5.6 shows that the airgap creates a reluctance to the magnetic field, decreasing the force on the magnet as the gap increases. The increase in the air gap further contributed to the rise in the solenoid's diameter. Therefore, the magnet's radius depends on the air gap and the solenoid's inner radius. As seen in Table 5.1, the magnet's radius is set to 2 mm smaller than the inner radius of the solenoid, ensuring that the air gap between the two is minimised.

The goal of defining the variables in Table 5.1 was to identify an optimal multi-layer geometry for the coil design that met the design requirements.

### 5.3.2 Magnet Plunger

With the radius restriction of the PM determined, its length restriction remains. The magnet's dimensions were simulated through a parametric sweep to assess the effect of increasing its length, which needs to be limited. The equations in Subsection 5.2 highlighted that the distance of the magnet from the base solenoid will also have an effect on its force produced and, therefore, was simulated to determine the most optimal starting position to achieve a maximum stroke length. The permanent magnet used in the design simulations is a Neodymium Magnet (NdFeB52).

The parametric simulation results to determine the magnet length and starting position restrictions are shown in figure 5.7.

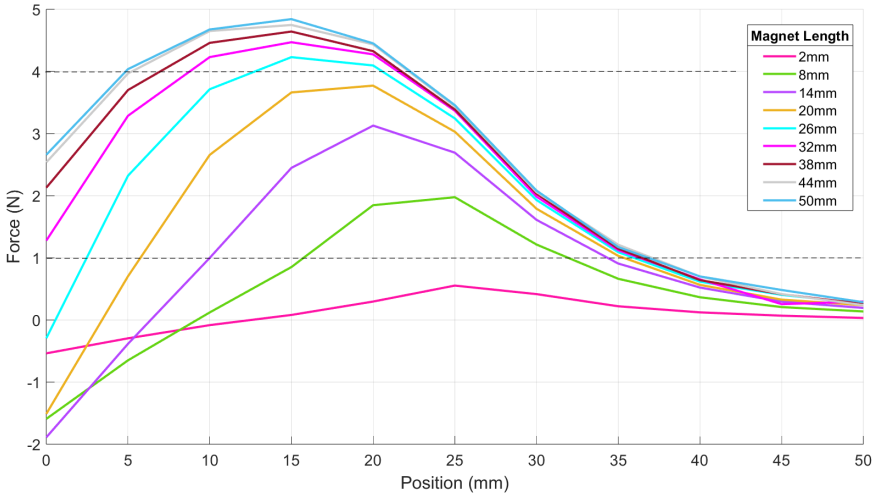


Figure 5.7: Force per Magnet Length and Position

Figure 5.7 shows that the longer magnets produce greater forces; however, they are accompanied by greater volume and, therefore, weight. On the other hand, the smaller magnets with lengths of 2 mm and 8 mm only produce a force in the positive direction when positioned at 7 mm within the solenoid; therefore, they do not achieve the desired stroke length. It is evident that longer magnets produce positive forces from the base of the magnet and have a sufficient stroke. The magnets with lengths 32 mm, 44 mm and 50 mm produce positive forces before the base of the solenoid, which suggests that their position can be shifted to start before the solenoid base, extending their stroke further. Therefore, by comparing the extreme cases and interpolating other magnet lengths, the magnet length was limited to a minimum and maximum length of 4mm and 32mm, respectively. Their starting positions correspond to the position where the force crosses the dotted 1N line in Figure 5.7.

The parameter restrictions enable the specifications of variables to be declared in the ANSYS Sensitivity and Optimisation analysis.

## 5.4 Optimisation Simulation Results

The parametric simulations and the declared variables are inputs to a Sensitivity and Optimisation analysis in ANSYS Workbench. A structured multi-stage optimisation approach was adopted. First, a sensitivity analysis was performed to identify the influence of each geometric and electrical parameter on actuator force and mass. This ensured that the optimisation process was guided by analytical results rather than unrestricted parameter exploration. Subsequently, a multi-objective optimisation using an evolutionary algorithm evaluation was conducted to maximise force output and minimise actuator mass. The resulting Pareto-optimal configurations represent the set of best feasible actuator designs.

### 5.4.1 S6: Sensitivity Analysis

The parameter ranges presented in Table 5.2 were defined based on constraints, electromagnetic material properties, and thermal considerations. The coil wire diameter limits were determined using the American Wire Gauge (AWG) standard and the bobbin slot width to ensure manufacturable winding. The maximum current range was constrained according to expected resistive heating under

continuous operation, ensuring that the coil temperature does not exceed the 75°C thermal limit. Magnet dimensions were selected based on commercially available NdFeB N35 while ensuring that the magnet remains above its coercivity threshold. Therefore, the parameter ranges represent a physically and thermally suitable range of the design.

The system variables and corresponding restrictions are summarised in table 5.2. These ranges are the limitations for the Sensitivity and Optimisation analysis forming step 6 in the design methodology flowchart shown in Figure 5.1.

Table 5.2: Simulation Variable Ranges

| **Variable** | **Range** |
|---|---|
| **Number of turns** | 200-1200 |
| **Current (A)** | 0.056-0.92 |
| **Layers** | 5-30 |
| **Wire Diameter (mm)** | 0.153-0.9 |
| **Magnet Height(mm)** | 4-32 |
| **Inner Radius(mm)** | 3-14 |
| **Magnet Radius(mm)** | 1-8 |
| **Magnet distance(mm)** | >1N position |
| **Solenoid Diameter** | <40 |
| **Solenoid Length** | <35 |
| **Force (N)** | >Mg |

Figure 5.8 shows the results from the Sensitivity Analysis, highlighting the effect each variable has on the design parameters as a percentage indicated by the colour map.

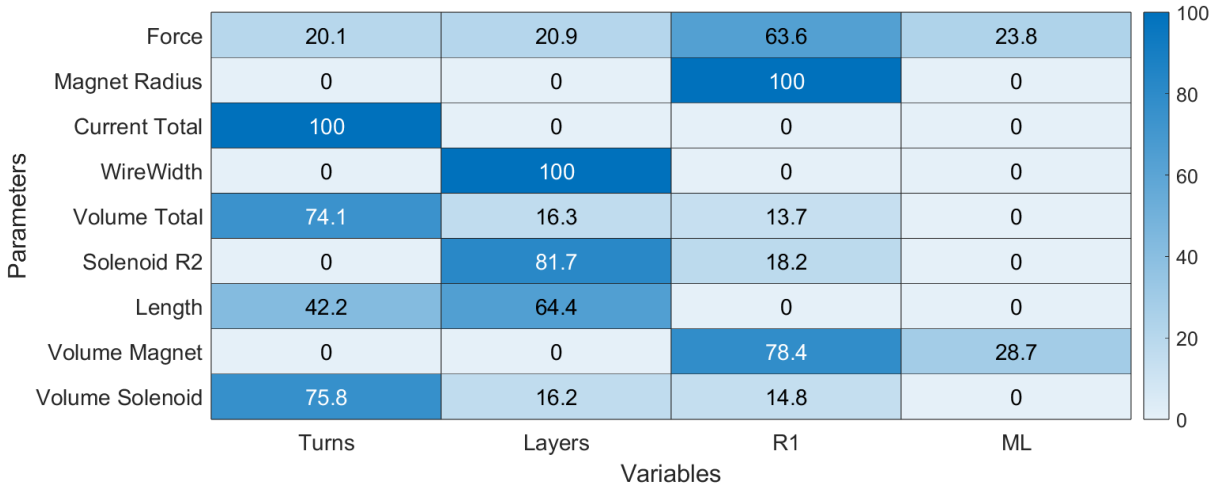


Figure 5.8: Sensitivity Results

From Figure 5.8, it is evident that the variables contributing the most to the design objectives of maximising the force is the inner radius of the solenoid, R1 at 63.6% followed by the magnet Length, ML, 23.8%, the layers, 20.9%, and turns 20.1%. The inner radius of the solenoid directly correlates to the magnet radius, illustrating that these variables should be prioritised. The contribution of the

magnet radius and length corresponds to the analytical solutions of the force on the magnet. As seen in Equation 5.1, the magnet's radius is directly proportional to the force produced, and the force depends on the position of the magnet relative to the solenoid base, which relates to its length as seen in Equation 5.3. This correlation highlights how the analytical solutions, despite giving valuable insight into the most important design variables, cannot quantify their contributions as a percentage. Similarly, their contribution confirms the relationship observed in the analytical solutions, Equation 5.1, where the number of turns is directly proportional to the force on the magnet and the current linear. The Turns and Layers, which contribute evenly to the force produced, dominate the volume contribution. This is expected as the turns and layers increase the solenoid length and width, respectively, effectively increasing the volume. The turns and layers are related to the total face current, which shows that coil current impacts the force generated. Finally, the magnet contributes the least to the volume at 13.7%.

The Sensitivity results show the complex relationship each variable has with the objectives. Due to the number of variables used and their varying contributions, an Optimisation analysis was conducted to determine the best combinations.

### 5.4.2 S7: Optimisation Analysis

The analytical analysis shows that the force that the magnet experiences is highly dependent on the position of the magnet within the solenoid. At the same time, the stroke depends on both the magnet's height and the solenoid's length. To achieve a sustained force capable of lifting the magnet out of the solenoid, creating a vertical displacement, the geometry of the plunger needs to be optimised. The optimisation methodology follows the flowchart in Figure 5.9.

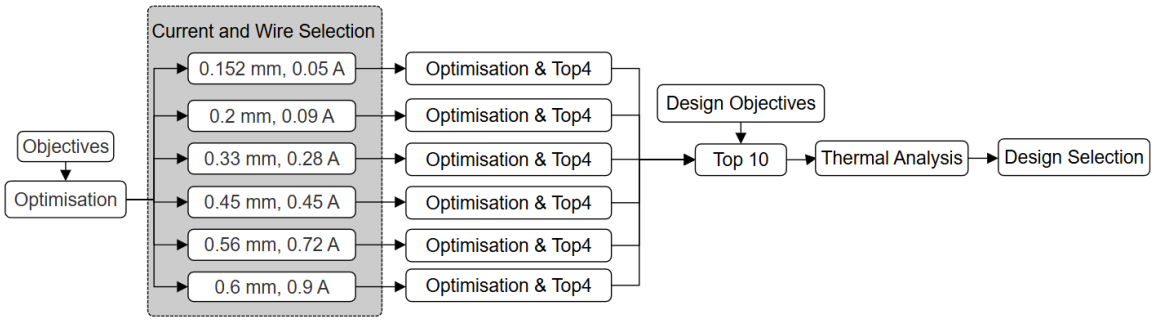


Figure 5.9: Optimisation Methodology Flowchart

Figure 5.9 shows that each wire and current combination undergoes an optimisation; this is due to the specifications of current capacity and wire diameter specifications, where setting the current and the wire diameter as fixed variables in the simulation prevents wires with incorrect current being output as optimal designs.

Optimisation is achieved through simulations in ANSYS Workbench using OptiSLang. The objectives are to maximise the force on the magnet while minimising the volume of the components. OptiSLang enables multi-objective optimisation, which leads to a set of Pareto optimal solutions. The Pareto Plot highlights the optimal designs that satisfy the conflicting objectives and allows the best designs to be selected. The optimisation results for over 200 designs per wire diameter are shown in the Pareto curves in figure 5.10.

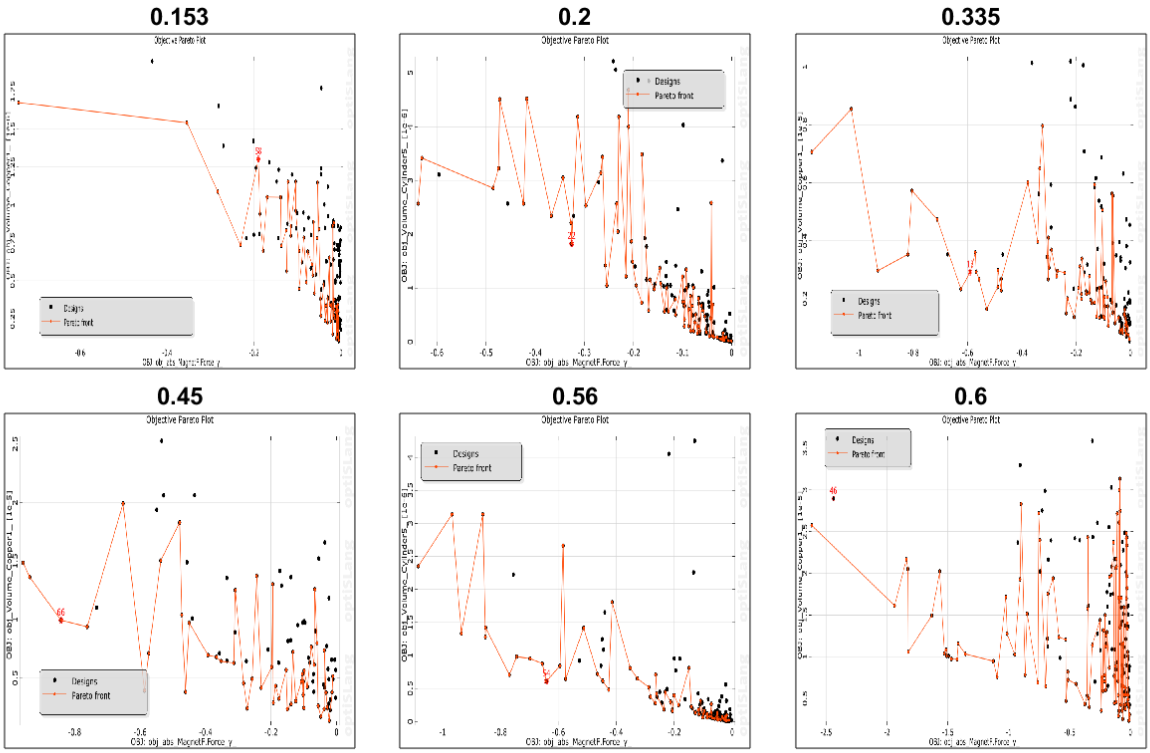


Figure 5.10: Pareto Optimisation Results. Figure Titles: Objective Pareto Plot. Figure x-axis title: Objective Magnetic Force Y Direction. Figure y axis labels: Objective Volume of Copper Cylinders

From the Pareto results in Figure 5.10, the designs per wire diameter were investigated. The top 4 designs that produced the highest force were selected per wire diameter, resulting in 24 top designs. The top 24 designs were then narrowed to a top 10 based on their force-to-volume ratio. The top 10 designs are summarised in Table 5.3. The designs that produced the largest force per wire width were chosen because the force was the main objective in the optimisation process, followed by the volume, which was used to reduce the number of designs for selection. The top 10 designs were then compared against one another based on their average force over the magnet's stroke length, thermal management, maximum force, and force to total volume. The configurations are labelled 1 to 10 (C1-C10) in Table 5.3.

Table 5.3: Top 10 Optimal Configurations

| **Parameter** | **C1** | **C2** | **C3** | **C4** | **C5** | **C6** | **C7** | **C8** | **C9** | **C10** |
|---|---|---|---|---|---|---|---|---|---|---|
| W.D(mm) | 0.6 | 0.6 | 0.56 | 0.56 | 0.45 | 0.45 | 0.335 | 0.335 | 0.2 | 0.153 |
| I.r(mm) | 8.96 | 9.8 | 9.05 | 7.31 | 9.59 | 7.13 | 8.78 | 7.70 | 9.08 | 9.21 |
| I(A) | 0.92 | 0.92 | 0.729 | 0.729 | 0.457 | 0.457 | 0.288 | 0.288 | 0.091 | 0.056 |
| Layer | 12.08 | 13 | 14.40 | 10.93 | 22.86 | 30.00 | 22.23 | 16.54 | 27.59 | 14.24 |
| M.H(mm) | 15 | 24 | 15 | 30 | 18 | 25 | 23 | 27 | 16 | 18 |
| Turns | 602 | 477 | 979 | 231 | 209 | 562 | 649 | 397 | 1200 | 1106 |
| V.Cop $cm^3$ | 17.153 | 19.6 | 25.24 | 4.73 | 3.92 | 9.94 | 5.73 | 2.94 | 3.52 | 1.68 |
| V.mag $cm^3$ | 2.43 | 3.6 | 2.30 | 2.66 | 3.35 | 2.04 | 3.44 | 2.81 | 1.011 | 2.27 |
| Length (mm) | 29.9 | 27 | 38.1 | 11.9 | 4.1 | 8.4 | 9.8 | 8.0 | 8.7 | 11.9 |
| O.R (mm) | 16.2 | 17.6 | 17.1 | 13.4 | 19.9 | 20.6 | 16.2 | 13.2 | 14.6 | 11.4 |

| Parameter | 1 | 2 | 3 | 4 | 5 | 6 | 7 | 8 | 9 | 10 |
|---|---|---|---|---|---|---|---|---|---|---|
| C.W (mm) | 7.2 | 8.7 | 8.1 | 6.1 | 10.3 | 13.5 | 7.4 | 5.5 | 5.5 | 2.2 |
| I.Total (A) | 554 | 438 | 713 | 168 | 95 | 257 | 187 | 114 | 109 | 61 |
| C.D (mm) | 32.4 | 35.2 | 34.2 | 26.9 | 39.8 | 41.3 | 32.5 | 26.5 | 29.2 | 22.8 |
| M.R (mm) | 7 | 7 | 7 | 5.3 | 7.6 | 5.1 | 6.8 | 5.7 | 7.1 | 7.2 |
| Fmax (N) | 1.82 | 1.93 | 1.84 | 0.79 | 0.64 | 0.96 | 1.28 | 0.69 | 0.77 | 0.45 |
| Favg (N) | 0.81 | 0.97 | 0.82 | 0.29 | 0.23 | 0.34 | 0.47 | 0.23 | 0.23 | 0.15 |
| F2Sol ($N/cm^3E^2$) | 10.62 | 9.81 | 7.27 | 16.7 | 16.5 | 9.67 | 22.37 | 23.5 | 21.5 | 26.67 |
| F2Mag ($N/cm^3E^2$) | 74.39 | 52.24 | 79.51 | 29.85 | 19.3 | 46.99 | 36.9 | 24.6 | 75.67 | 19.64 |
| T.Vol $cm^3$ | 19.57 | 23.4 | 27.59 | 7.36 | 7.26 | 11.96 | 9.17 | 5.74 | 4.56 | 3.92 |
| F2T.Vol ($N/cm^3E^2$) | 9.29 | 8.25 | 6.65 | 10.73 | 8.80 | 8.02 | 13.92 | 12.03 | 16.76 | 11.31 |
| Temp $°C$ | 49.6 | 37 | 45.7 | 39.2 | 36.4 | 38.7 | 43 | 39.8 | 36 | 33 |

Table 5.3 highlights the parameters of each solenoid plunger design. The average force over the magnet stroke length is measured from when the force on the magnet reaches a positive 1 N and is recorded for 45 mm. This enables various configurations to showcase their exerted forces over the desired stroke length, enabling accurate selection of the optimal configuration. The Fmax on the other hand is the highest force over the stroke length. F2Sol is the force per volume of the solenoid, F2Mag is the force per volume of the magnet, and F2T is the force per total volume. These parameters identify how the volume of both the solenoid and the magnet contributes to the force-to-volume ratio, demonstrating that in some designs, the magnet volume contributes a larger percentage than the solenoid volume. The visual representation of each solenoid plunger configuration 1 through 10 is illustrated in Figure 5.11 with the magnets modeled as black cylinders and the solenoid as transparent orange cylinders to ensure the magnets visibility.

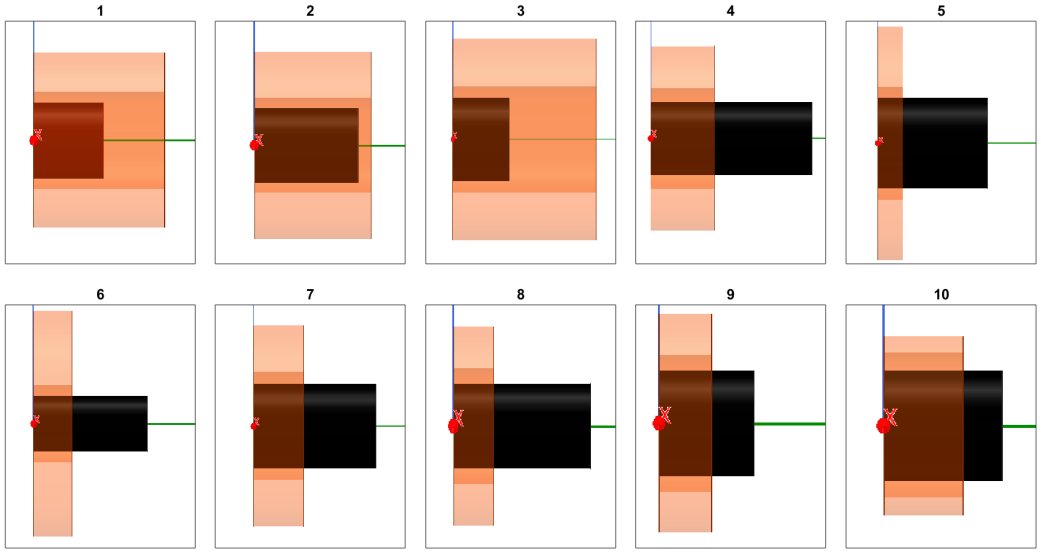


Figure 5.11: Optimised Solenoid Plunger Simulation Visual

Figure 5.11 depicts the variability in the optimal designs, showcasing designs with varying magnet and solenoid lengths and widths. The variability in the design enables comparison and demonstrates how

the optimisation algorithm identifies combinations of variables that would not have been investigated through trial and error. To evaluate each design and select the most suitable configuration for the solenoid plunger, a thermal analysis was conducted for the top 10 designs.

### 5.4.3 S8: Thermal Simulations

The literature in Section 3.2.1 highlighted that temperature analysis for electromagnetic actuators is necessary due to their tendency to lose energy through heat [62] [67]. Thermal analysis was conducted in Ansys Icepak to analyse the rise in temperature and heat distribution of the implemented designs. The simulation models were four-way coupled with Icepak to generate thermal images indicating the heat generated by each design. The coils were excited with their corresponding current for 10 minutes. The thermal analysis provided an additional component which allowed the designs to be compared. It also indicated the duration that the current could be run before the heat produced affected the system's functionality.

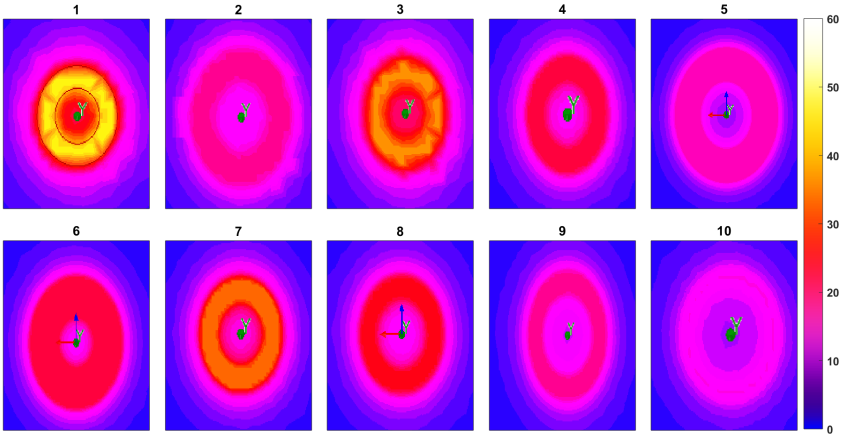


Figure 5.12: Thermal Analysis

Figure 5.12 shows the temperature of each coil design after 10 minutes. The design temperatures are displayed on the colour bar, ranging from 20°C to 60°C; the maximum temperature of each design is included in Table 5.3. Configuration 1 can be seen as generating the most heat at 49.6°C with a total volume of 19.57 $cm^3$ and a total current of 554 A, while configuration 7 reaches 43°C with a total volume of 9.17 $cm^3$ and current of 187 A. Therefore, the thermal analysis highlights that the temperature is not only a function of the current through the coils but also relates to the geometric configuration, further emphasising the requirement for multi-objective optimisation and design comparison.

## 5.5 S9-S10: Design Comparison and Selection

The sensitivity and optimisation analysis is crucial in reducing the design space through design objectives, enabling their comparison. The top 10 designs were ranked according to placement in the following categories: Force to Volume, Maximum Force (Force Max), Average Force (Force (avg)), and Temperature, where 1 represents first place and 10 represents last place. Figure 5.13 shows the results of each configuration per selection category.

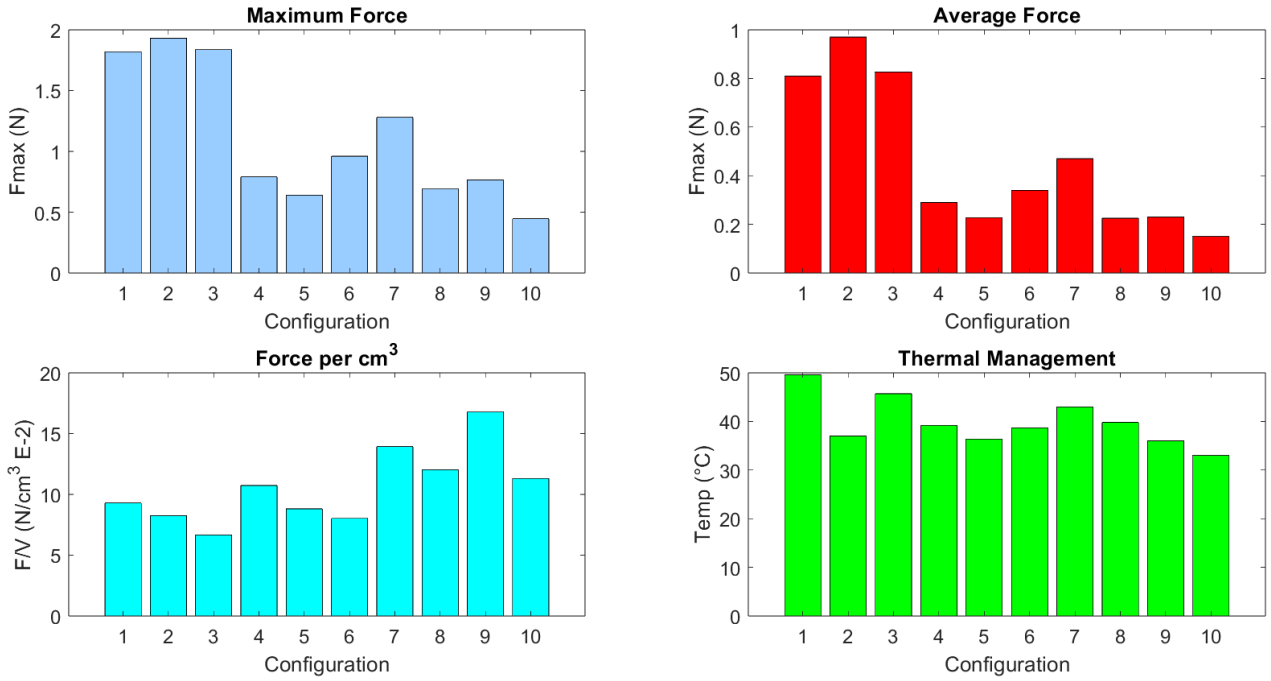


Figure 5.13: Design Comparison

Figure 5.13 highlights that configuration 2 achieved the highest Maximum and Average force. A trend can be seen where configurations with higher currents and larger wire diameter achieve greater forces. However, due to the larger wire diameters, their volumes increase, decreasing their Force to Volume. The thermal management bar graph shows the maximum temperature each configuration reached after 10 minutes; since lower temperatures are desired, it can be seen that configuration 10 outperforms the other configurations regarding thermal management.

Table 5.4: Design Placement per Category and Final Position

| Configuration | F(Max) | F(Avg) | F/V | Temp. | Sum | Final Placement |
|---|---|---|---|---|---|---|
| 1 | 3 | 3 | 6 | 10 | 22 | 4 |
| 2 | 1 | 1 | 8 | 4 | 14 | 1 |
| 3 | 2 | 2 | 10 | 9 | 23 | 5 |
| 4 | 6 | 6 | 5 | 6 | 23 | 6 |
| 5 | 9 | 8 | 7 | 3 | 27 | 9 |
| 6 | 5 | 5 | 9 | 5 | 24 | 7 |
| 7 | 4 | 4 | 2 | 8 | 18 | 3 |
| 8 | 8 | 9 | 3 | 7 | 27 | 10 |
| 9 | 7 | 7 | 1 | 2 | 17 | 2 |
| 10 | 10 | 10 | 4 | 1 | 25 | 8 |

Table 5.4 ranks the designs in Figure 5.13 from highest to lowest for the Maximum Force, Average Force, Force per $cm^3$, and from lowest to highest in the Thermal Management. Therefore, the sum of the scores indicates the configuration's performance over all four categories; the design with the smallest sum, thus, allocated a final placement of 1. From Table 5.4, it is evident that configuration 2 outperformed the other configurations across the categories, leading to its selection for implementation.

Figure 5.13 highlights that configuration 2 outperformed the other designs as it produced the lowest sum. The ranking categories represent the design objectives of maximising force and minimising volume whilst preventing overheating. From the rankings, it is clear that Configuration 2 performs the best on average, suggesting it is the most optimal choice for implementation based on the objective. The configuration parameters are summarised in Table 5.3 (C2). The selection of configuration 2 confirms that system requirement SR.7 Minimising Volume, and SR.6 Maximising force was achieved.

Figure 5.14 shows the Pareto plot where the top 4 designs for the 0.6 mm wire were initially selected. The Pareto plots highlight how the design selection process eliminated numerous configurations from the design space, resulting in selecting one design that best suited the objectives.

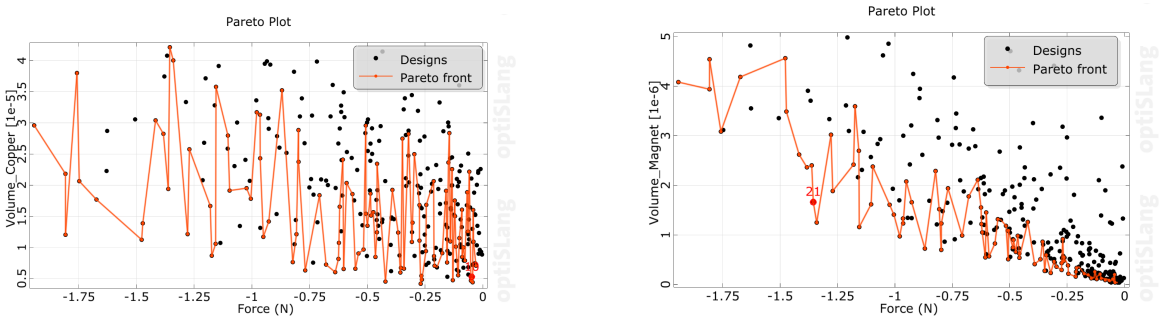


(a) Force to Solenoid Volume

(b) Force to Magnet Volume

Figure 5.14: Pareto Plot Solution for 0.6mm Wire

Design 2, a 0.6mm wire diameter solenoid plunger configuration, was thereafter implemented and tested, and the results were compared to those of the analytical and FEA solutions.

## 5.6 S11: Solenoid-Plunger Implementation and Experimental Results

The optimised solenoid plunger was implemented as per Figure 5.15. The 0.6 mm copper wire was wound around a PLA bobbin, with the NdFe52 permanent magnet (part 2) encased in a PLA sleeve (part 4). The magnet sleeve ensures the protection of the magnet and is coated in silicone gel to prevent friction. The magnet is secured in the sleeve by a PLA magnet cap (part 1). The sleeve stopper, Part 5 in Figure 5.6 prevents the magnet from extending further than the height of the solenoid.

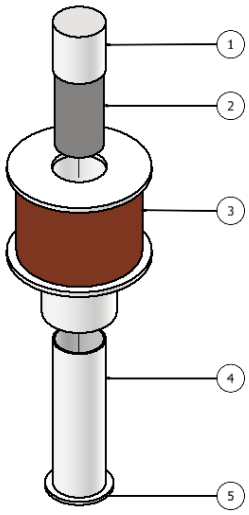


| Part | Description |
|---|---|
| 1 | Magnet cap |
| 2 | Magnet |
| 3 | Solenoid |
| 4 | Magnet Sleeve |
| 5 | Sleeve Stopper |

Figure 5.15: Solenoid-Plunger Implementation

The implemented solenoid dimensions match those of the simulations, resulting in a solenoid Length of 27 mm, Outer Radius of 17.6 mm, Inner Radius of 9.8 mm, Magnet Radius of 7 mm, and Magnet height of 24 mm. The current in the coil is 0.92 A for the 0.6 mm wire.

### 5.6.1 Power Circuit

A Dual H-Bridge DC motor driver supplied the current to the coil. The two outputs from the motor driver are attached to either end of the solenoid, enabling control of the current in both directions. An Arduino Uno controls the commands given to the two signal inputs on the H-bridge. This allows the motor to be driven forward and reverse, enabling the magnet to extend or contract depending on the current direction.

When an external voltage supply powers the H-bridge, the maximum output current is 2.5 A, which would successfully handle the current of the implemented design. To control the current in the coil, the resistance of the coil in combination with the H-bridge was measured. The coil current specification, 0.92 A, and its combined resistance determined the voltage supplied.

The solenoid plunger is driven by a dual DC H-bridge motor driver, with individual control provided through an Arduino, as illustrated in Figure 6.12. When actuated, each solenoid is driven with 0.92 A as per the specifications discussed in Chapter 5 Section 4.4.2.

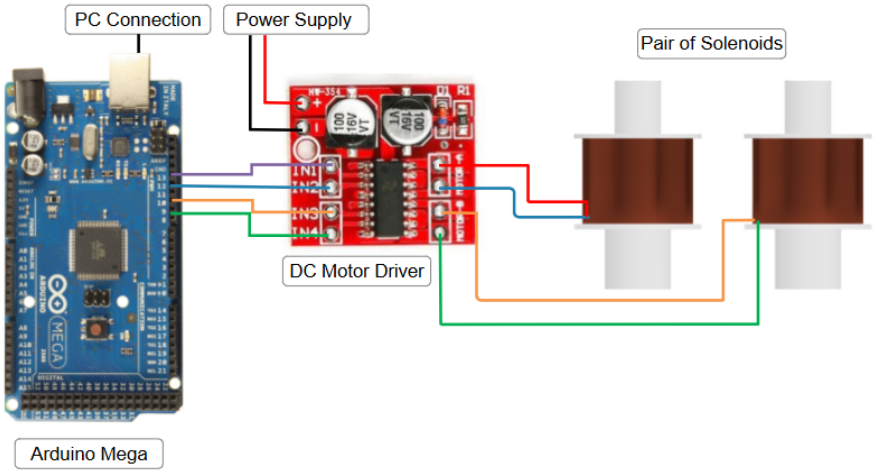


Figure 5.16: Driving Circuit for a Pair of Solenoid Plungers

The movement of the platform is controlled by an Arduino Mega that excites each solenoid as per the code shown in Appendix C.

## 5.7 System Testing

The selected design was experimentally evaluated based on thermal management, measured force, and weight. These tests correlate to system requirements SR.2. Sufficient stroke length for vertical movement larger than the magnet length, SR.6 Sufficient force to support its weight and an additional load, SR.8 A system capable of longevity, SR.9 Low power requirements, and SR.10. Thermal management. The measured results were then compared to simulation and analytical results. The design was simultaneously evaluated for the remaining system requirements, SR.1 EM System capable of three DOF, SR.3 System capable of modulation, SR.4 System capable of scalability, and SR.5 System capable of connection in a parallel configuration.

### 5.7.1 Heat Generated

The thermal analysis of the heat generated by the implemented coil indicates the system's longevity and how long it can be continually run before the heat produced affects the actuator's functionality. The ability of the coil to manage its thermal effects was analysed by driving the coil with 0.9A for 10 minutes. The coil's temperature was also evaluated at 1.4 A to observe the heat produced; this ensures that if the system required additional force, increasing the current did not compromise the coil's performance. The start and end temperature of the system and the thermal images were taken with a Testo 882 Thermal imager. The test procedure was conducted as follows.

1. The starting temperature and current within the coil were measured and recorded.
2. The coil was excited with 0.92 A and 1.4A for 10 minutes.
3. After every minute, the temperature was recorded, and a thermal image was taken

Table 5.5 shows the results of the measured thermal analysis for the design at 0.9 A and 1.4 A. The table summarises the temperatures of each design recorded by the Thermal Imager marked by (T.C) and

Icepak simulations (S), as well as the difference between the two (Δ°C). Throughout the experimental measurement, the current was maintained to ensure accurate comparison with the simulations.

Table 5.5: Coil Temperature Measurements

| **T (min)** | **0.92A S (°C)** | **0.92A T.C (°C)** | **(Δ°C)** | **1.4A S(°C)** | **1.4A T.C(°C)** | **(Δ°C)** |
|---|---|---|---|---|---|---|
| 0 | 22 | 22 | 0 | 24 | 24 | 0 |
| 1 | 23.7 | 24 | -0.2 | 26.7 | 27 | 0.3 |
| 2 | 25.5 | 26 | -0.47 | 30.4 | 32.2 | 1.8 |
| 3 | 27.2 | 28.1 | -0.88 | 33.9 | 35.7 | 1.8 |
| 4 | 28.8 | 29.2 | -0.44 | 37.4 | 38.8 | 1.45 |
| 5 | 30.4 | 30.8 | -0.35 | 40.7 | 42.1 | 1.43 |
| 6 | 31.9 | 32.8 | -0.81 | 43.9 | 45.3 | 1.31 |
| 7 | 33.4 | 33.5 | -0.01 | 46.9 | 47.8 | 0.9 |
| 8 | 34.9 | 34.9 | 0.02 | 49.9 | 49.6 | -0.39 |
| 9 | 36.3 | 36 | 0.33 | 52.9 | 51.8 | -1.1 |
| 10 | 37.7 | 37 | 0.68 | 55.7 | 53.6 | -2.1 |
| (Δ°C) | 15.6 | 15 | NA | 31.7 | 29.6 | NA |

It is evident from Table 5.5 that the current increase affects the temperature increase of the coil. The maximum measured temperature (T.C) was 37° at 0.9A, and 53.6° at 1.4A, an increase of 16.6° for a 0.48 A increase. With the simulated results (S) correlating to the measured results (T.C). Despite the expected increase in temperature, the system manages the thermal effects as the rise in temperature did not influence the system's functionality. However, the increase suggests that the solenoid plunger system should operate at a nominal 0.92 A and only, when necessary, increase the current for greater force. The thermal images after the 10-minute test period are shown in Figure 5.17

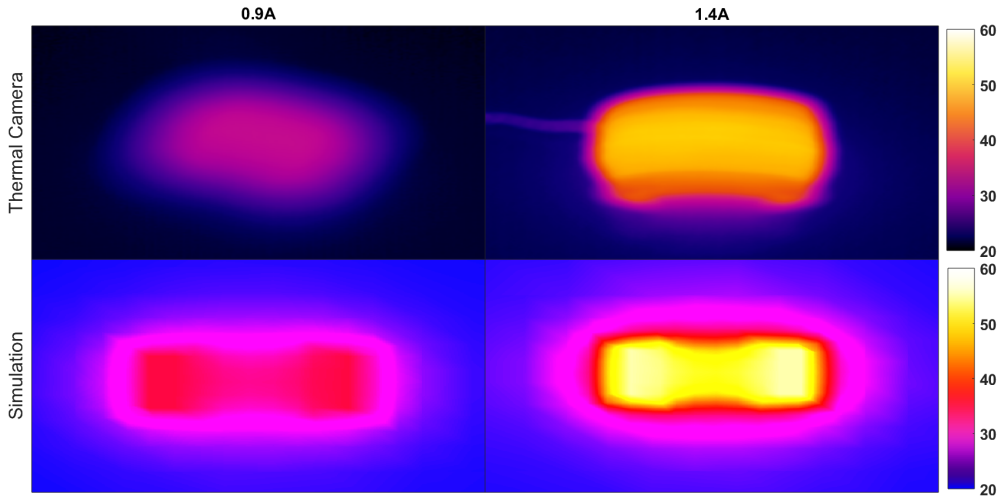


Figure 5.17: Thermal Imager and Icepak Thermal Images

Figure 5.17 temperatures are summarised in Table 5.5. The images show the heat distribution and maximum temperature similarities between the measured and simulated results for both currents. The

colour bar associated with the thermal camera and the simulations highlights that the heat produced is distributed evenly across the coil and dissipates quickly away from the coil.

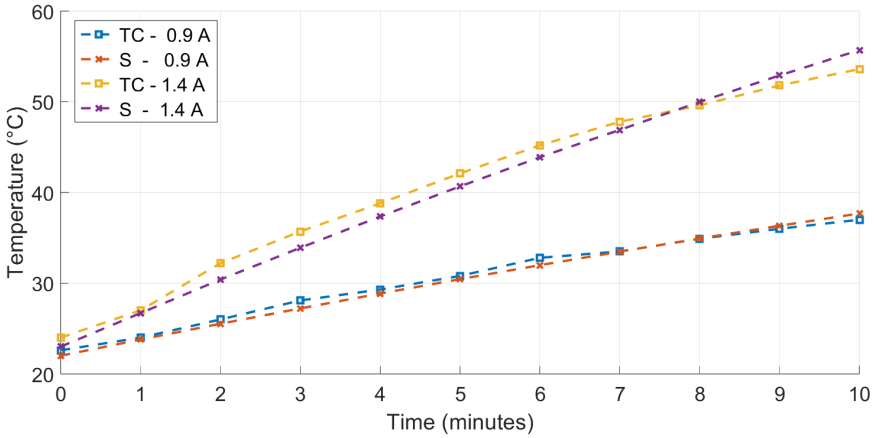


Figure 5.18: Measure and Simulated Thermal Results

Figure 5.18 shows the increase in temperature of the solenoid-plunger system over the 10-minute testing. The measured temperature results from the thermal camera (TC) closely match the ANSYS Icepak simulations (S), with the simulations showing a more linear approach to the ohmic heat production than the measured results.

The thermal analysis showed that the coil temperature increased to 37° over the 10 minutes at 0.9 A, with a total change in temperature of 15°. During the experiment, a voltage was supplied to the coil, resulting in the desired 0.9 A; the current did not change throughout the 10 minutes, indicating that the resistance did not increase due to the temperature rise. Therefore, the 15° rise did not affect the functionality of the coil, confirming the configuration manages thermal effects meeting SR.10. Thermal management is an essential factor in maintaining the optimal performance of the coil, as overheating results in the coil's resistance increasing, which decreases the current, affecting the force produced and power loss. The ability of the coil to dissipate heat effectively is due to both the current adhering to the current capacity of the coil and the geometry of the coil design, ensuring a large enough surface area to dissipate heat. The thermal analysis concludes that the design met system requirements SR.8, SR.9, and SR.10. The coil driven with 1.4 A experienced a larger total temperature increase of 29.6°, with a final temperature of 53.6°. The coil was not designed to operate continuously for 10 minutes at 1.4 A; therefore, a temperature rise was expected. Despite the increase in temperature, the functionality of the coil was not compromised, and it was demonstrated that in instances where the solenoid plunger required a larger force, driving the coil for short bursts would not result in wires burning or suboptimal performance. The temperature increase when driven with 0.9 A and 1.4 A, maintained a high conductivity of copper compared to Figure 3.1 The temperature-dependent electrical conductivity of copper, in Section 3.2.1, where the maximum temperature after the 10 minutes was 53.6°, which correlates to $5 \times 10^7 [S/m]$. Demonstrating that the increase in temperature did not reduce the conductivity significantly.

### 5.7.2 Force

The force of the solenoid-plunger system was measured with a Vernier Dual-Range Force Sensor. The testing configuration is shown in Figure 5.19.

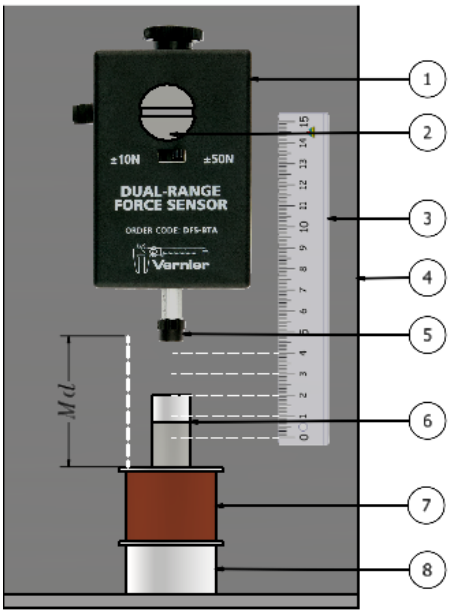


| Part | Description |
|---|---|
| 1 | Vernier Force Sensor |
| 2 | Height adjustment Screw |
| 3 | Ruler |
| 4 | Sensor Mount |
| 5 | Bumper Attachment |
| 6 | Magnet Cap |
| 7 | Solenoid |
| 8 | Base Extension |

Figure 5.19: Force Testing Experimental Setup

To record the force over the stroke length of the magnet, the force was measured at 5mm increments from 0mm to 45mm out of the solenoid. At each increment, the force was measured three times, and the average of the forces were recorded for that measurement. The force sensor was secured to a support stand to ensure no movement in the system other than the magnet. The solenoid structure was also adapted to include a base extension, Part 8 in Figure 5.19. The base extension was secured to the base of the support stand, which ensured that the solenoid-plunger system did not tilt during the force measurements.

Figure 5.20 summarises the experimental force results. The Measured force results validate the ANSYS simulation results, and the analytical results confirm that the equations used in Section 5.2 can be used to model the force experienced by the magnet. The validation of the analytical calculations enables the dynamic movement of the magnet and system to be modelled and parameterised outside of the simulation environment.

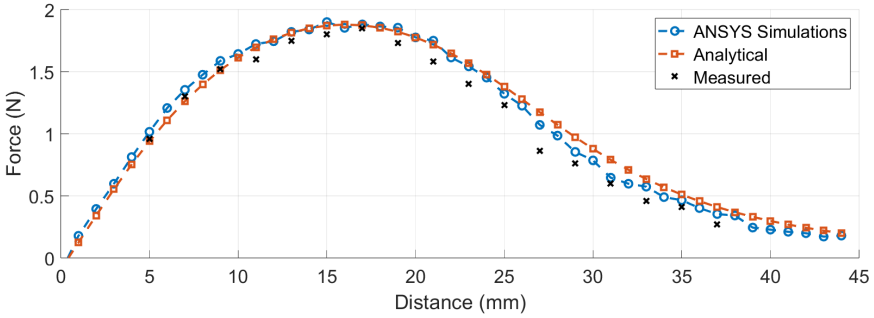


Figure 5.20: Force Over Magnet Stroke: 0.92 A

Figure 5.20 shows the Measured, Analytical and Simulated forces over the 45 mm stroke. The force that the magnet reaches peaks between 12 mm and 17 mm at 1.87 N and decreases to a negligible point at 45 mm. The force that the magnet experiences resembles a sinusoidal waveform, highlighting that the force generated is highly dependent on the position of the magnet, which confirms the Sensitivity Analysis. Since the solenoid plunger system did not experience overheating, the force experienced by the magnet was investigated for current 1.4 A, 1.8 A and 2 A.

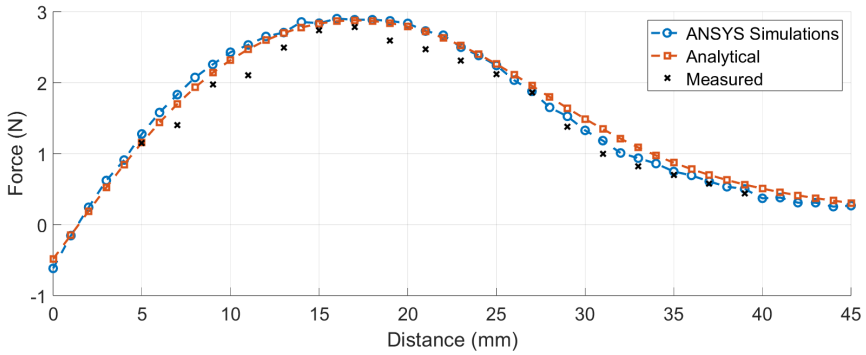


Figure 5.21: Force over Magnet Stroke: 1.4 A

Figure 5.21 mimics Figure 5.20, with the main difference being the greater peak force of 2.9 N. Both figures closely match the ANSYS simulations and analytical results, which validate the Measured results and the implementation process.

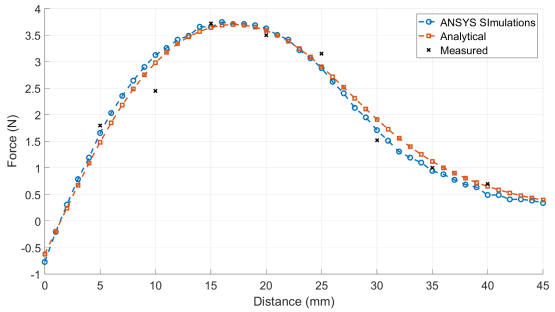


Figure 5.22: Force Over Magnet Stroke: 1.8 A

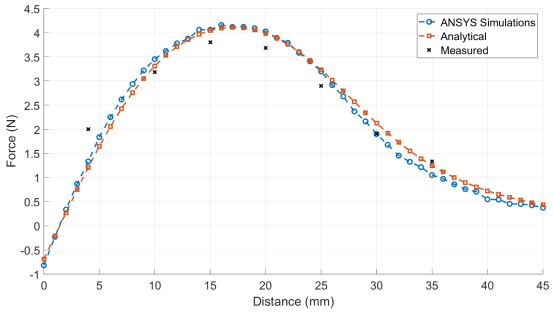


Figure 5.23: Force Over Magnet Stroke: 2 A

Figures 5.22 and 5.23 showcase the force experienced by the magnet reaching 3.68 N and 4.09 N, respectively. This shows that an increase in the current in the coil results in an increase in the force produced, which can be used intermittently when the system requires a larger force. From this, the solenoid plunger system can operate at a nominal 0.92 A and, when necessary, increase the current to 2 A for short periods to prevent overheating. 2.5 A is the H-bridge DC motor driver output current limit, and therefore, 2 A was deemed the limit to prevent high switching losses and potential damage to the power circuit.

The force results of the magnet demonstrate that the plunger is capable of a stroke length of 4.5 cm, with additional force available through a current increase to facilitate an additional load. Therefore, the results conclude that the design meets requirements SR.2 sufficient stroke length for vertical movement of 4.5 cm, and SR.6 Force is necessary to support its weight and provide an additional load.

### 5.7.3 Weight

The importance of conserving the system's weight has been emphasised as an optimisation variable throughout the design process through the system's volume. Table 5.6 shows the weight of each component in the system.

Table 5.6: Mass of System Element

| Item | Mass (g) |
|---|---|
| Nd52 Magnet | 28 |
| PLA Componenets | 12 |
| Copper Coil | 120 |
| System Total | 160 |

Table 5.6 confirms the Sensitivity Analysis and Simulated results, which showed that the majority of the system volume was made up of the solenoid copper coil. Despite the volume of Configuration 2 being the second highest, its force-to-volume ratio and thermal effects validated its mass, ensuring that the volume was minimised relative to the force that the design produced. Its ability to produce sufficient force and manage thermal effects validates its volume and concludes system requirement SR.7. Minimising volume was achieved.

## 5.8 LEMA: Solenoid Plunger Conclusion

The chosen and implemented solenoid plunger achieved three DOF due to the universal joints that support the solenoid and permanent magnet end effector. Through optimisation the most suitable design configuration was identified, enabling the system to minimise its volume whilst maximising the force produced. The resulting design can produce sufficient linear force to move the magnetic plunger 4.5 cm and carry an additional load. The simulated and implemented results closely resemble one another, further validating the accuracy of the implemented system. Whilst the thermal analysis of the design enabled its ability to manage thermal effects and maintain low power consumption, which supports longevity. Due to the simple design, the system is capable of scalability and modulation in the form of multiple solenoid plungers in a parallel connection. The design of the linear electromagnetic actuator, solenoid plunger, achieved its design requirements, reflecting a successful design and optimisation procedure. The modularity and capability of the system to be extended to a parallel mechanism highlights its potential use in the spinal actuator. This is due to the system's ability to produce high, controllable forces, where each solenoid actuator has 3 DOF. The DOF available when multiple actuators are combined in parallel can facilitate the motion requirements of an electromagnet spinal actuator.

# Chapter 6

# Electromagnetic (EM) Spinal Segment Actuator

Chapter 5 presented a linear electromagnetic solenoid actuator capable of 3 DOF. This chapter builds upon the optimised solenoid plunger model, extending it to a system capable of achieving 6 degrees of freedom (DOF) that can be integrated as a segment in a spinal actuator. Additionally, it reviews the existing literature on the current 6 DOF platforms and adapts their configurations to design the segment actuator. Finally, the chapter presents the implementation of the EM Spinal Segment Actuator.

## 6.1 6 DOF Parallel Actuators

Most robotic spine structures, such as the ones described in Table 2.2: Summary of Quadruped Robots and Table 2.3: Summary of Humanoid Robots, are actuated by motors and servo motors interlinked in serial and parallel configurations [19] [23].

The typical representation of a serial spinal structure, shown in Kotaro, Kenta and ERMIS, mimics the physiological structure of human spines, including tendons and a central structure representing the spinal column [9] [40]. Serial configurations enable a large workspace and offer high manoeuvrability. However, they cannot support significant loads and have reduced precision [99]. As demonstrated in Kotaro, the serial linkage relies on multiple artificial muscles, limiting the degrees of freedom (DOF) to the number of motors and tendons [9]. This results in Kotaro's inability to achieve substantial rotation due to the complex control required for the 16 motors attached to the tendons. Similarly, ERMIS, another serial configuration with disk-ball-disk joints, offers increased flexibility [52]. However, it suffers from low repeatability and lacks the ability to absorb shocks effectively [52] [9].

On the other hand, parallel structures offer greater stiffness, lighter weight, larger load capacity, and higher velocities compared to their serial counterparts [19] [9]. The parallel kinematic systems are made of linear actuators arranged in parallel, allowing for a range of movements in MDOF [99]. Despite the parallel assembly not resembling the human torso, it achieves many functions of the human torso [4]. These systems outperform serial mechanisms' dynamic performance and reduce the number of actuators required, resulting in a structure with a compact size, improved stiffness and payload capacity [9].

A parallel manipulator is a mechanical system that employs serial chains to support a single platform or end effector [5]. The parallel structure provides numerous advantages, including higher payload capacity, stiffness, and precise motion [100]. These benefits stimulate their use in precise manufacturing,

medical science, and space exploration equipment [5] [100]. The Stewart Platform with 6 DOF is the most popular parallel manipulator, proposed initially as a flight simulator [101]. The Stewart or Stewart-Gough platform is widely used in vibration isolation, optical satellites, and aerospace control [102] [29] [103] [104] [105]. These platforms consist of three to six actuator legs connected by combinations of the joints illustrated in figure 6.1.

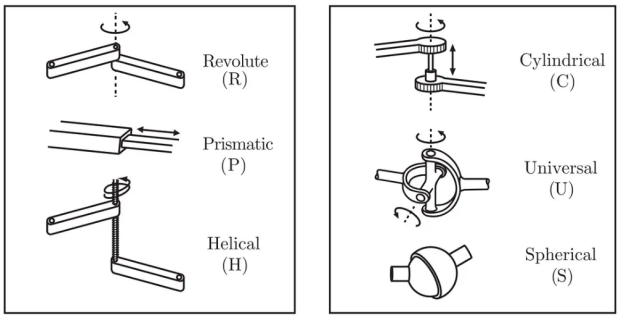


Figure 6.1: Joint Types [3]

The joints demonstrated in Figure 6.1 enable movement in multiple directions, with universal and spherical joints offering the highest DOF [106].

The serial chain of parallel actuators enables increased dexterity and high dynamic response, making this structure highly suitable for a spinal actuator [9] [101]. However, the parallel mechanism has drawbacks such as small workspaces, design difficulties, complex kinematics and dynamic analysis [4] [102]. Due to this, only a few spinal-like robots have been designed by combining serial actuators into parallel structures [107] [28]. An example is a waist-trunk system proposed by Liang, which uses a three and six-legged Universal-prismatic-Universal (UPU) platform connected in a serial chain, effectively designing a hybrid humanoid torso [4]. By controlling each actuator leg, the waist-trunk system demonstrates the advantages of parallel mechanisms: high payload, stiffness and dynamic response. Figure 6.2 illustrates the parallel system, with the stick elements representing linear actuators [4].

Figure 6.2: UPU parallel System [4]

Figure 6.2 demonstrates the increased stability parallel systems offer, as their weight is evenly distributed around interlinked platforms.

The standard actuators for Stewart platforms are piezoelectric, pneumatic, hydraulic, voice coil and electric linear actuators [103] [108]. Figure 6.3 shown an example of a piezoelectric Stewart Platform in Figure 6.3a, and pneumatic and hydraulic Stewart platforms in Figures 6.3b and 6.3c.

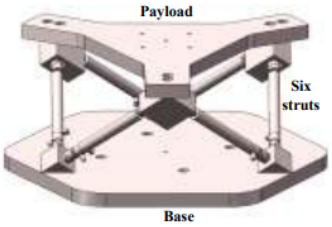


(a) Piezoelectric [109]

(b) Pneumatic [110]

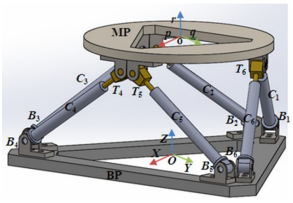


(c) Hydraulic [111]

Figure 6.3: 6 DOF Stewart Platforms: (a) Piezoelectric, (b) Pneumatic, (c) Hydraulic.

Some Stewart Platforms utilise pneumatic or hydraulic actuation, substituting electric actuators to provide positional accuracy and high force, illustrated in Figures 6.3b and 6.3c [110] [111] [109]. Although pneumatic and hydraulic actuators have many advantages, their actuation systems are bulky, complex, and require dedicated infrastructure for operation. Additionally, controlling pneumatic joints to intermediate positions is difficult due to the compressibility of air and its nonlinear behaviour, limiting their application in a spinal robot segment [19] [106] [106]. In contrast, electromagnetic actuators have a simpler structure, faster response, no additional structures and easy integration with control systems [19] [103] [112].

The literature suggests that combining Stewart Platforms' parallel mechanism with linear solenoid plunger actuators would result in a system that benefits from high accuracy, fast response, low cost, and scalability [19]. These characteristics are advantageous in the design of a spinal actuator segment for use in a humanoid robot.

## 6.2 EM Spinal Segment Actuator Design

The following sections describe the implementation of the 6 DOF spinal actuator segment using the configuration of Stewart Platforms and electromagnetism as the actuation. The design of the 6 DOF spinal actuator segment builds off Chapter 5 by extending the single leg of the solenoid plunger into a six-legged platform.

The design requirements and limitations of the 6 DOF spinal actuator segment are based on the thoracic part of a human spine which can achieve 26° flexion, 22° extension, 30° lateral bending and 47° axial rotation, with each joint having 5 or 6 DOF [1] [40] [8]. The design requirements are listed below.

DR.1 Capable of Lateral Bending, Flexion and Extension of 25°.

DR.2 Capable of rotation of 47°.

DR.3 Capable of movement in 6 DOF.

DR.4 Stability: Ability to support its weight. Sufficient force to support its weight and maneuver.

DR.5 Fast response.

DR.6 Closed loop control is out of scope.

The design requirements for the EM actuator segment originate from the ROM of the thoracic and lumbar spine discussed in Section 2.3 Table 2.1. The movement of the thoracic spine was emulated. Since in the implemented system, the lateral bending and flexion/extension are achieved similarly on different axes, the flexion/extension and lateral bending angles were combined. Therefore, to mimic the human thoracic spine, the system required a lateral bending and flexion/extension of $22° - 30°$ and a rotation of $47°$. These requirements are stipulated in DR.1 and DR.2. DR.3 ensures that the spinal segment actuator has 6 DOF, which mimics a typical human vertebra, whilst DR.4 requires the system to support its weight and provide stability. DR.5 ensures that the system responds to inputs quickly and efficiently, a desirable characteristic in robotic actuators. Exciting individual solenoids control the system to perform various movements in an open-loop configuration. DR.5 reiterates that closed-loop control is out of the project's scope, as achieving the motion of a human spine, in terms of DOF, with simplicity is the main objective of the thesis.

### 6.2.1 Structural Design

The linear solenoid plunger in Chapter 5 is extended to a Stewart Platform, enabling 6 DOF of a top platform. The solenoids are arranged around the platform's base in pairs, orientated $120°$ apart. To achieve top plate rotation, the solenoid pairs are angled oppositely to one another, as shown in figure 6.4. Figure 6.4a and 6.4b show a 3D CAD assembly and a drawing of the system with the six solenoid plungers arranged around the base platform, which are attached to the top platform. Figure 6.4c shows the isometric or angled view of the system, highlighting that the solenoid plungers are tilted at opposite angles in each pair.

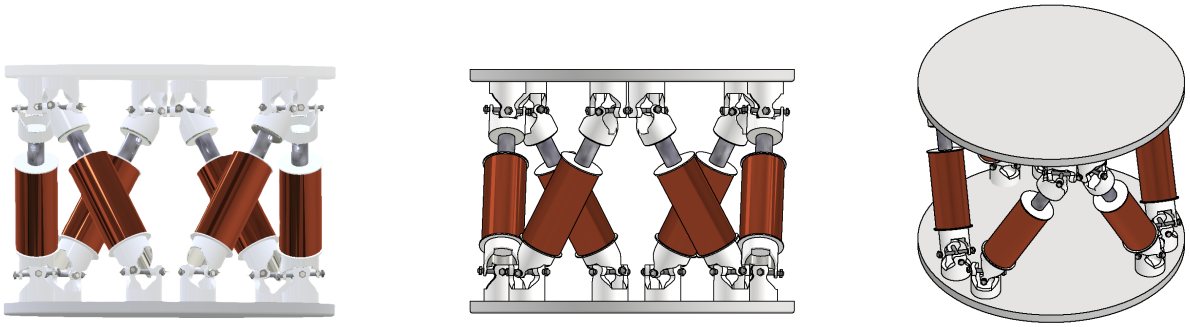

(a) Realistic View (b) Side View (c) Angled View

Figure 6.4: Assembly Drawing

A single solenoid plunger has 3 DOF and can translate along the Z-axis and rotate about the X and Y-axis. Controlling the input current in the six solenoid plungers results in 6 DOF, which allows various motions to be realised. The extent of each solenoid's translation and rotation in the X, Y, and Z directions depends on the magnet displacement out of the coil and the angle at which the solenoid plunger is positioned.

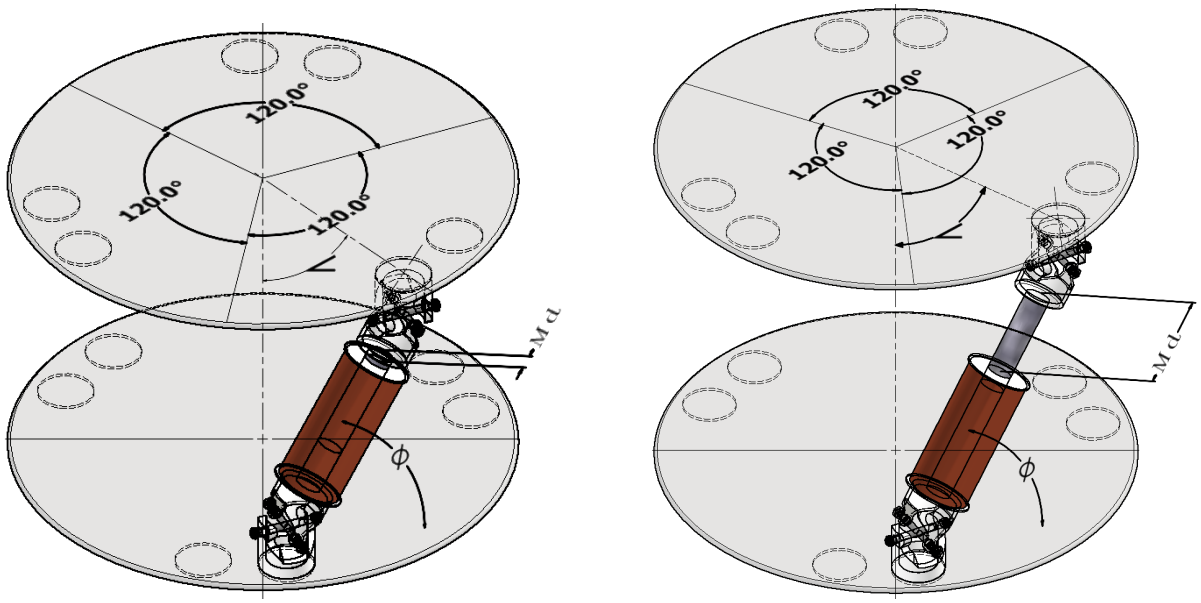


(a) Non-Extended Solenoid (b) Extended Solenoid

Figure 6.5: Plunger Extension and Plate Rotation

Figure 6.5 shows the extension of the magnet from the solenoid and the placement of the solenoid pairs around the plate, illustrated by the dotted circular pattern. Each solenoid pair is positioned 120° apart, with the top plate offset by 60°. $Md$ represents the distance the magnet travels out of the solenoid, $\phi$ represents the angle at which the solenoid is tilted, and $<$ represents the top plate's rotation angle.

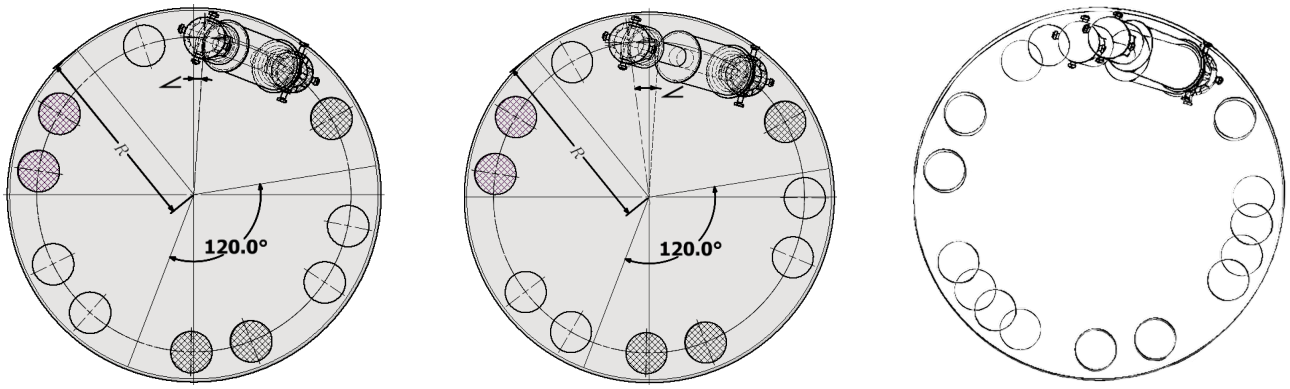


(a) Non-Extended Solenoid (b) Extended Solenoid (c) Image Overlap

Figure 6.6: Top View of Solenoid Extension and Plate Rotation

Figure 6.6 shows the rotation of the top plate as the magnet extends from the solenoid, $R$, is the radius of the top plate and $<$, is the angle of rotation about the centre of the plate. Figure 6.6a shows the non-extended magnet, Figure 6.6b shows the extended magnet and Figure 6.6c shows the overlap of the two movements. As shown in Figures 6.6 and 6.5, the extension of the magnet from the solenoid determines the rotation angle of the top plate. Therefore, this relationship must be analysed and designed to meet the specified requirements.

Universal joint connectors fix the solenoid to the base platform and the magnet's end effector to the top platform. The universal joints provide the freedom to move about the yaw and pitch axis, ensuring that when the solenoid plunger is extended or contracted, all the actuators in the configuration can

adjust their position, enabling smooth movement of the top platform. This is illustrated in Figure 6.7, where when one solenoid is extended, the freedom of movement at the joints enables the complementary solenoid to adjust its angle to ensure that the top plate moves accordingly.

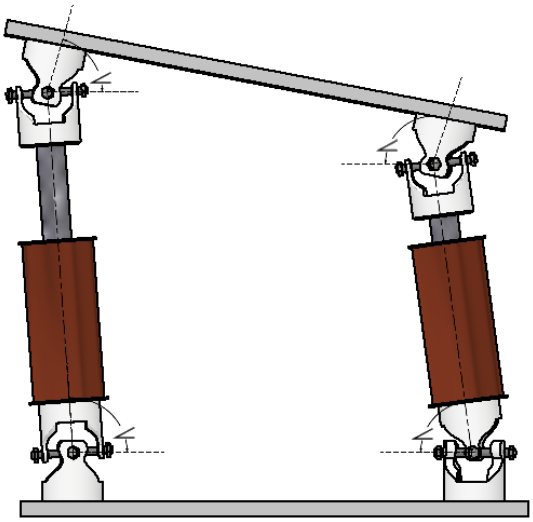

Figure 6.7: Connector adjustments

Six solenoid plungers arranged around the base plate provide stability and 6 DOF for the platform. The platform's movement capabilities include vertical translation by extending all solenoid plungers simultaneously, clock-wise (CW) and counter-clockwise (CCW) rotation by extending one solenoid in each pair, and extension/ flexion and bending by exciting one or two pairs of solenoids. To ensure the desired position of the top platform is achieved, the platform's dynamic movement is analysed.

## 6.3 System Dynamic Equation

The dynamic behaviour of a single solenoid plunger is derived based on the interactions between the actuation force elaborated on in Chapter 5 Section 5.2, the gravitational force, and the resulting displacement of the magnet and platform. The dynamic parameters include the force exerted by the solenoid, the mass, the radius of the top platform, and the solenoid's tilt angle. The following dynamic equations are simplified with the full solution shown in Appendix D Inverse Dynamic Modelling of 6 DOF parallel Actuator. Figure 6.8 and Figure 6.9 show the free body diagrams of the full and simplified solenoid plunger system.

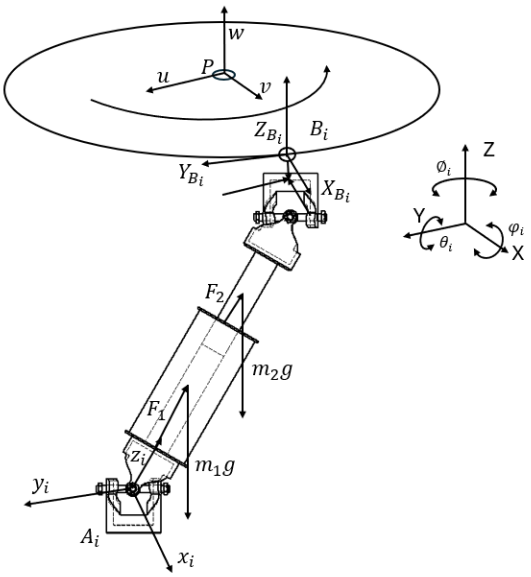


Figure 6.8: Free Body Diagram: Full Version

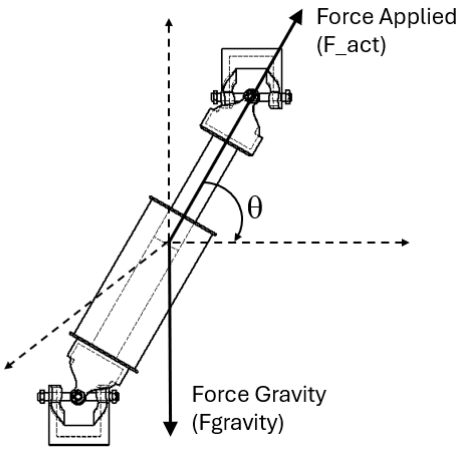


Figure 6.9: Free Body Diagram: Simplified Version

Based on Figure 6.9, the simplified analysis begins by considering the actuation force on the platform by the solenoid denoted by $F_{act}$, and the mass of the plunger and plate $m$. When the solenoid is tilted at an angle $\theta$ from the horizontal base, the gravitational force on the plunger system is

$$F_{\text{gravity}} = mgsin(\theta) \tag{6.1}$$

Where $g$ is the acceleration due to gravity, let $F_{act}$ be the actuation force of one solenoid, and the friction against the vertical displacement of the solenoid be $F_{fric}$. The net force acting on the plunger and the subsequent acceleration are shown in the Equations 6.2 and 6.3

$$F_{\text{net}} = F_{\text{act}} - F_{\text{fric}} - F_{\text{gravity}} \tag{6.2}$$

$$a = \frac{F_{\text{net}}}{m} \tag{6.3}$$

Since the PLA sleeve has a clearance from the magnet and silicone lubricant is applied, friction is ignored. From equations 6.2 the solenoid system's force needs to overcome the weight of the magnet and the end effector to extend and accelerate. The PLA stopper attached to the magnet shown in figure 5.15 Part 5 prevents the magnet from ejecting from the bobbin structure. Therefore, the length of the magnet extension is restricted by the magnet length. Using the kinematic equation for displacement, the time, $t$, required for the plunger to travel a specified maximum displacement, $d$, is derived as,

$$t = \sqrt{\frac{2d}{a}} \tag{6.4}$$

The displacement of the plunger in the horizontal (X) and vertical (Z) directions are determined:

$$x_{displacement} = 0.5 \times a \times t^2 \times cos(\theta) \tag{6.5}$$

$$z_{displacement} = 0.5 \times a \times t^2 \times sin(\theta) \tag{6.6}$$

When the solenoid plunger exerts a force on the top plate, with radius $r$, a torque, $\tau$ is induced, causing the rotational motion.

$$\tau = F_{net} r cos(\theta) \tag{6.7}$$

The angular acceleration, $\alpha$ of the top plate and its moment of inertia, $I$, is,

$$\alpha = \frac{\tau}{I}, and, \;\; I = \frac{1}{2} m_p r^2 \tag{6.8}$$

Where $m_p$ is the mass of the top plate. The angular displacement is, therefore,

$$\phi = 0.5 \alpha t^2 \tag{6.9}$$

The platform's tilt angle also corresponds to the extension of the magnet plunger through the Equation 6.10.

$$Tilt = \arctan \frac{y}{2r} \tag{6.10}$$

The dynamic equations for the single solenoid plunger system provide the foundation for understanding the motion of a single leg. These equations emphasise the significance of the magnet extension (or stroke length) in facilitating both rotational and bending movements, as well as the impact of the solenoid plunger tilt angle. From this, the relationships between the components can be analysed, providing valuable insights for designing the platform configuration.

### 6.3.1 Actuator Leg Position an Angle

As mentioned, one solenoid plunger was optimised and extended into the 6-legged parallel actuator. Each actuator in the parallel system works together to achieve movement; therefore, duplicating an optimised design ensures that all actuators function optimally. The importance of the magnet stroke length was highlighted in the dynamic equations, and its relationship between the rotation and

extension of the top plate was established. Using the optimised solenoid plunger with a height of 30 mm and magnet length of 24 mm, the extension of the magnet from the solenoid was observed in Chapter 5 Section 5.3.2. As shown, the magnet can extend beyond its length due to the electromagnetic forces from the coil, reaching a maximum of 4.5 cm. Therefore, by controlling the input current, the stroke length of the magnet can be adjusted depending on the desired rotation and extension of the top plate.

The dynamic analysis and movement of the platform require solutions from the electromagnetic force and the relationship between the solenoid plunger and the platform. Where each solenoid produced a force of 1.87N, 2.9N, 3.68N and 4.09N at currents 0.92A, 1.4A, 1.8A and 2A, respectively.These forces' vertical and horizontal components are summed in the spinal segment, and are dependent on the tilt angle of the solenoid. Complexities in characterising the movement of the platform arise as the force produced from the solenoid plunger is not linear but sinusoidal. Using the force created from the single solenoid plunger system and the analytical solutions of the system in chapter 5, the relationship between the absolute distance the magnet travels, its vertical displacement, the angle in which the solenoid plunger is positioned, and the rotation that this extension would cause on the top plate is established. The angle at which the solenoids are tilted (Solenoid_Angle in the Z-direction) determines the top platform's rotation and vertical and horizontal displacement. Table 6.1 shows the solutions to the dynamic analysis of the platform and provides the Horizontal displacement (H_Displacement), the Vertical displacement (V_Displacement), the Rotation of the platform (Theta), and the Lateral Bending (Tilt). The Matlab code for the dynamic equations is shown in Appendix A.

Table 6.1: Vertical and Horizontal, Rotational and Tilt Displacement of the Top Platform

| **Solenoid_Angle** | **Time** | **H_Displacement** | **V_Displacement** | **Theta** | **Tilt** |
|---|---|---|---|---|---|
| 15 | 0.06 | 0.046 | 0.012 | 74.33 | 8.83 |
| 20 | 0.061 | 0.045 | 0.016 | 74.57 | 11.6 |
| 25 | 0.062 | 0.044 | 0.020 | 74.17 | 14.23 |
| 30 | 0.063 | 0.042 | 0.024 | 73.07 | 16.7 |
| 35 | 0.064 | 0.039 | 0.028 | 71.22 | 18.99 |
| 40 | 0.064 | 0.037 | 0.031 | 68.56 | 21.09 |
| 45 | 0.065 | 0.034 | 0.034 | 65.06 | 22.99 |
| 50 | 0.066 | 0.031 | 0.037 | 60.70 | 24.68 |
| 55 | 0.067 | 0.028 | 0.039 | 55.49 | 26.17 |
| 60 | 0.068 | 0.024 | 0.042 | 49.43 | 27.46 |
| 65 | 0.068 | 0.020 | 0.044 | 42.59 | 28.54 |
| 70 | 0.069 | 0.016 | 0.045 | 35.02 | 29.42 |
| 75 | 0.069 | 0.012 | 0.046 | 26.85 | 30.09 |

As shown in Table 6.1, the H_Displacement and the V_Displacement determine the rotation, Theta, and the tilt angle, Tilt. In which the horizontal and vertical displacement of the platform depends on the angle at which the solenoid-plunger is tilted, Solenoid_Angle.

Figure 6.10 depicts the relationship between the solenoid plunger angle and the resulting horizontal and vertical displacements over the length of the magnet extension (4.5 cm).

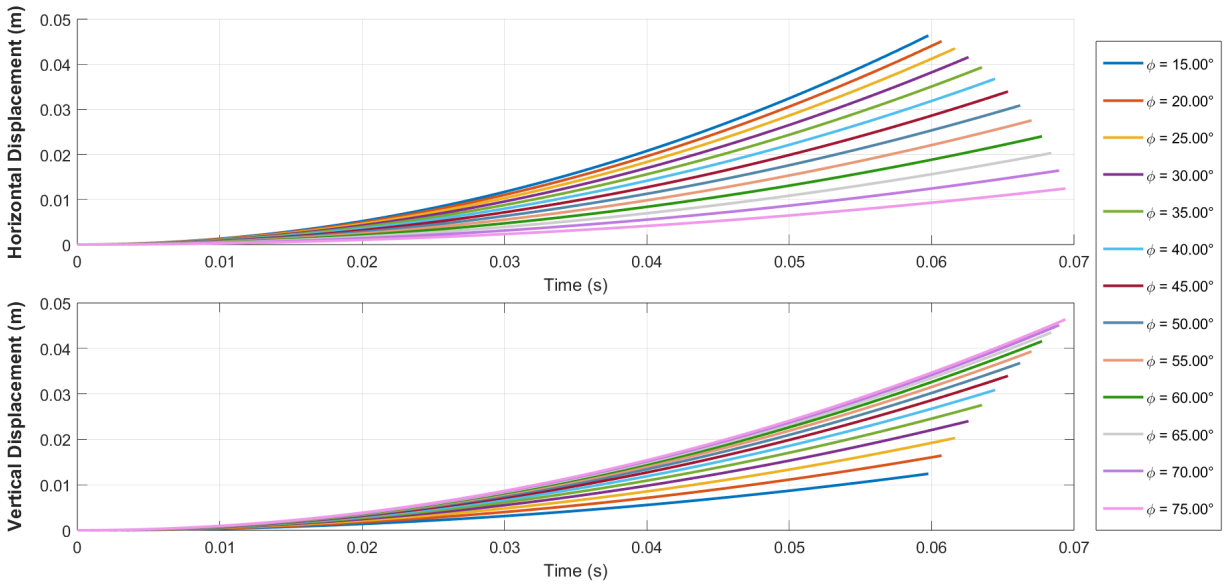


Figure 6.10: Horizontal and Vertical Displacement of the Platform at Different Solenoid-Plunger Angles

As seen in Figure 6.10, the horizontal and vertical displacement of the platform and, consequently, the magnet are inversely related. This is expected as the length of the magnet is fixed. Therefore, the total displacement of the magnet is always constant, resulting in an inversely proportional vertical or horizontal displacement depending on the angle of tilt as a result of gravity. It can also be seen that the solenoid plungers that are tilted at smaller angles, such as 15°, reach their maximum absolute displacement faster than those that are inclined at larger angles, such as 75°, which is attributed to gravitational force in the vertical direction slowing down the extension. Similarly, Figure 6.11 depicts the relationship between the angle of the solenoid plunger with the rotation and lateral tilt of the top plate.

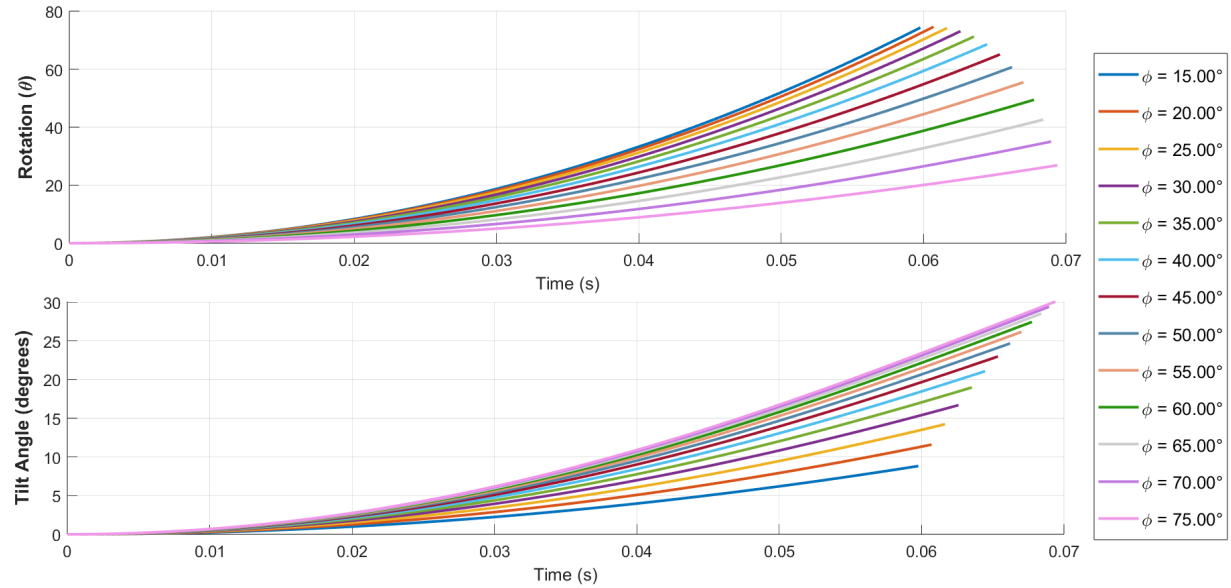


Figure 6.11: Rotational Angle and Tilt Angle of the Platform at Different Solenoid-Plunger Angles

Figures 6.11 and 6.10 show the same inverse relationship, where a more considerable rotational angle

results in a smaller Tilt angle, due to the relationship between vertical and horizontal displacement of the solenoid plunger. Therefore, the design of the 6-legged platform needs to compromise between tilt angle and rotation. Referring to the design requirements in Section 6.2 and Figures 6.11 and 6.10, to achieve a minimum tilt of 25° and rotation of 47° each solenoid-plunger needs to be angled at 60°.

## 6.4 EM Spinal Segment Implementation and Testing

The designed and optimised solenoid plunger in Chapter 5 is implemented according to Figure 6.4. Six solenoid plungers are arranged around the circular base plate in pairs that are 120° apart and are angled and 60° from the base of the platform. Each pair is oppositely tilted, with the top platform connecting each solenoid plunger at their respective angles. The top platform is rotated by 60° to accommodate the angled solenoid plunger pairs. Each solenoid plunger pair is driven by a dual DC H-bridge motor driver, with individual control provided through an Arduino, as illustrated in Figure 6.12. When actuated, each solenoid is driven with 0.92 A as per the specifications discussed in Chapter 5 Section 4.4.2.

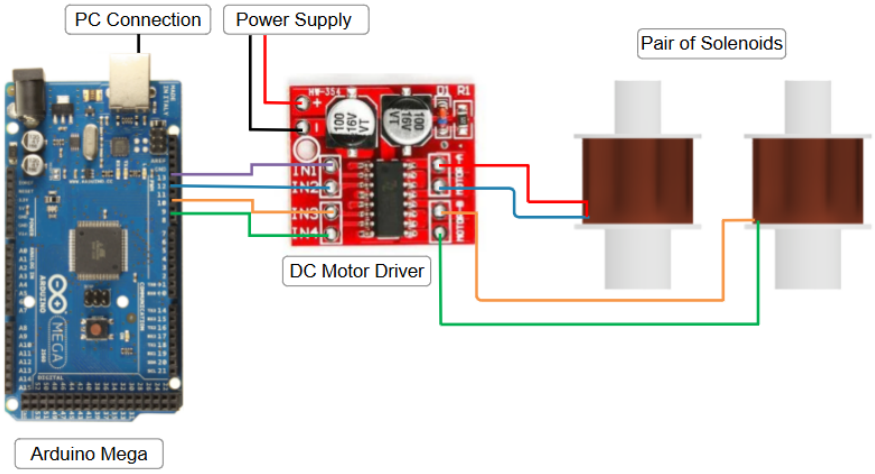


Figure 6.12: Driving Circuit for a Pair of Solenoid Plungers

The movement of the platform is controlled by an Arduino Mega that excites each solenoid as per the code shown in Appendix C. To accurately observe the tilt and rotational angle of the platform, an Inertial Measuring Unit (IMU) MPU-6050 is attached to the top platform to record the movement when different solenoid plunger pairs are excited. The MPU-6050 is an integrated six-axis motion processing component that uses a three-axis gyroscope and a three-axis accelerator to measure movement. The platform's tilt and rotational angles are then compared to the analytical results in Section 6.3. Each movement was repeated three times, and the average results were recorded. Experimentally verifying the tilting and rotation movement of the platform ensures that the system can achieve the desired flexion/extension, lateral bending and rotation.

## 6.5 Results: Platform Movement

Based on the design requirements and the analytical solutions, the platform should be capable of rotating 47° about the Z-axis and a minimum tilt angle in 3 DOF of 25°. These movements satisfy the platform's requirement of mimicking the range of motion of a human spine.

### 6.5.1 Rotation Results

The rotation of the top platform is achieved by exciting solenoid plungers 1, 3, and 5, resulting in clockwise (CW) rotation. Similarly, exciting solenoid plungers 2, 4, and 6 produce counterclockwise (CCW) rotation. Figure 6.13 illustrates the solenoids and their corresponding numbers.

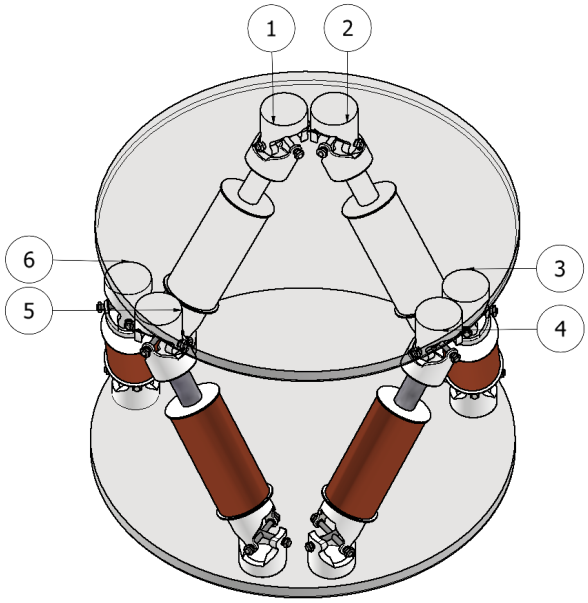


Figure 6.13: Rotational Actuation Numbered Diagram: Solenoids 1 to 6.

Figure 6.14 shows the measured and analytical results for the CW and CCW rotation of the top plate.

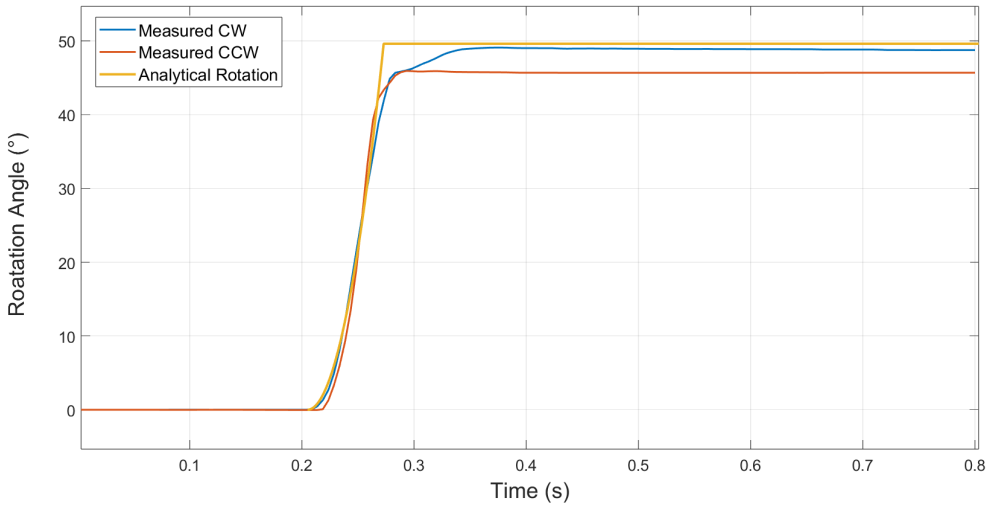


Figure 6.14: Measured and Analytical Results for Rotation of the Top Plate

Figure 6.14 shows that the measured results closely follow the analytical results. The CW rotation, however, demonstrates a slower rise time, reaching a rotational angle of 48.9°. The CCW movement, on the other hand, achieved a smoother rise time; however, it did not reach the rotation angle of the CW movement, resulting in a maximum rotation of 47°. The analytical response shows a smoother and faster rise time than the measured results, reaching a maximum rotation of 49.43°. The discrepancies between the analytical and measured results are attributed to the variable stiffness in the connectors

of the top platform and the minor differences between the actuators, resulting in one direction of motion being more effective than the other. Figure 6.14 further demonstrates that their position is maintained once the solenoid plungers have reached their maximum displacement. This shows the system's stability, where the non-actuated solenoid plungers support the actuated solenoid plungers in holding a desired position. The platform's stability and actuator adaptability are due to the parallel mechanisms' ability to distribute weight evenly, demonstrating that parallel systems effectively produce MDOF.

### 6.5.2 Lateral Bending (Tilt) Results

Exciting pairs of solenoid plungers result in the lateral bending and flexion/extension angle (Tilt). Due to the configuration of six equally distributed solenoid plungers, the tilt of the top plate can occur in three directions. Lateral bending and flexion/extension are achieved by exciting pairs of solenoids, such as 1 & 2, 3 & 4, and 5 & 6; the bending caused by the extension of the solenoid pairs is referred to as bending A, B and C, with the actuator numbers correlating to Figure 6.13.

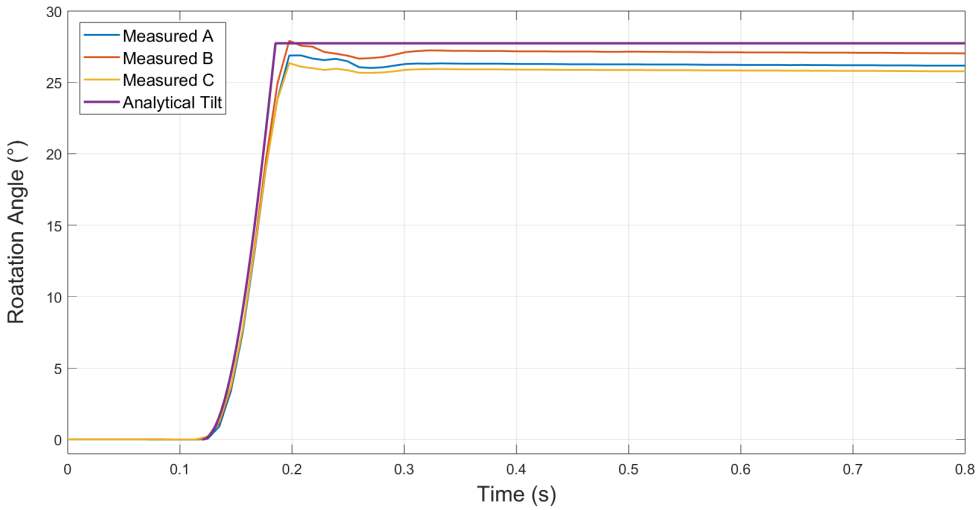


Figure 6.15: Measured and Analytical Results for the Bending of the Top Plate in 3 DOF

Figure 6.15 highlights that the analytical solutions mimic the results collected from the IMU for all three tilts, A, B and C. Some discrepancies can be noted as there is an overshoot and a slower rise time in each tilt compared to the analytical solution. Further, solenoid plunger pair B outperformed A and C, reaching a tilt angle of 27.2°, 26.3° and 25.9° respectively, recorded at steady state. The overshoot movement of the platform suggests that the plunger system accelerates and abruptly stops due to the PLA stopper causing the overshoot.

Figures 6.15 and 6.14 show that the platform achieved design requirements DR.1 and DR.2 reaching a tilt angle of greater than 25° and a rotation of 47°. The system achieved these movements through simple control and demonstrated its quick response of 0.1 s.

### 6.5.3 6 Degree-of-Freedom (DOF) Results

The platform achieves 6 DOF through three translations and three rotational movements, as described below.

**Rotation**:

1. Torsion: Achieved by exciting solenoid plungers that tilt in the same direction. Therefore, three excited solenoid plungers enable the rotation of the top plate in both clockwise and counter-clockwise directions.
2. Flexion-Extension: Achieved by exciting two pairs of adjacent solenoid plungers for flexion and exciting the remaining solenoid plunger for extension.
3. Lateral Bending: Achieved by exciting either one or two pairs of adjacent solenoid plungers, resulting in lateral bending.

**Translation**:

4. Axial Extension/Compression: Achieved by exciting all solenoid plungers in the system.
5. Lateral shear: Achieved by exiting adjacent solenoid plunger pairs with different currents (one higher) to achieve a lateral shift.
6. Lateral Translation: Repeat Lateral shear movement with another solenoid plunger pair.

Figure 6.16 and Figure 6.17 illustrate the 6 DOF movement achieved by the platform.

(a) Resting

(b) CW

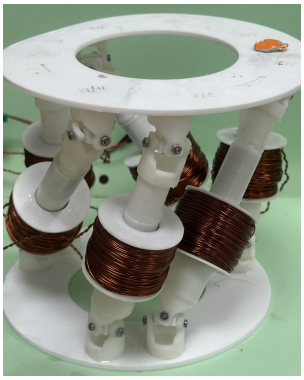

(c) CCW

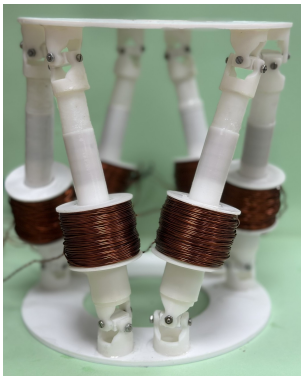

(d) Vertical Translation

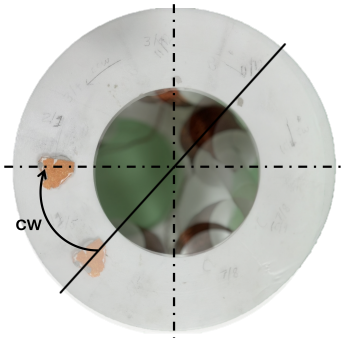


(e) CW Superposition

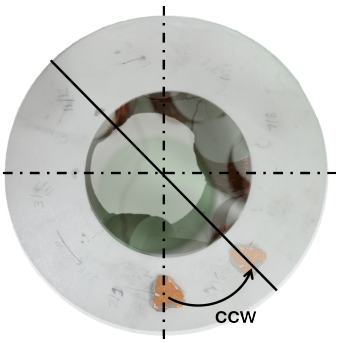


(f) CCW Superposition

Figure 6.16: Images of various states of the robot: (a) Resting; (b) CW; (c) CCW; (d)Vertical Translation; (e) CW Superposition; (f) CCW Superposition.

Figure 6.16a shows the platform at rest; each solenoid plunger has two wires protruding from the solenoid connected to the respective H-Bridges fed to the Arduino and power supply. Figures 6.16b and 6.16c show the CW and CCW movement, respectively, highlighting how the non-actuated solenoid plungers move to accommodate the movement of the actuated solenoid plungers, enabling the rotation. Figure 6.16d shows the fully extended platform, where it is evident that the magnet encased in the PLA sleeve has fully translated out of the solenoid and is held in the extended position. Figures 6.16e and 6.16f correspond with Figures 6.16b and 6.16c showing the top view of the rotation, with the original position superimposed on the final rotated position.

Similarly, Figure 6.17 demonstrates the remaining movements of the structure. Figures 6.17a, 6.17b, and 6.17c show the tilting movement of the platform in all three directions, with the actuated solenoid plungers holding their end position. At the same time, the non-actuated pairs adjust their connector angles to accommodate the movement. Lastly, the lateral translation of the platform is shown in Figures 6.17d and 6.17e. Lateral translations within human and animal spines are minimal; however, Figures 6.17d and 6.17e illustrates the platform's ability to replicate this movement individually.

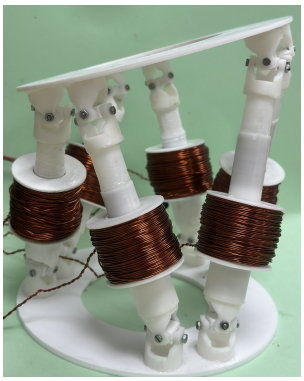

(a) Tilt A: Bending

(b) Tilt B: Bending

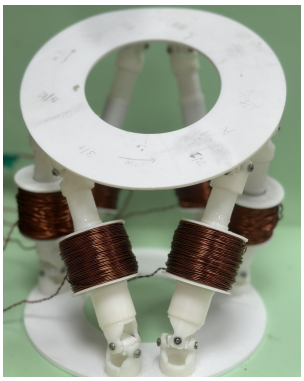

(c) Tilt C: Flexion/Extension

(d) Lateral Translation 1

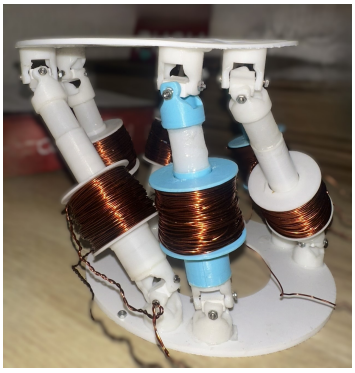

(e) Lateral Translation 2

Figure 6.17: Images of various states of the robot: (a) Tilt A: Bending; (b) Tilt B:Bending ; (c) Tilt C: Flexion/Extension; (d) Lateral Translation 1; (e) Lateral Translation 2

Figure 6.16 and Figure 6.17 confirms that the system has met the design requirement DR.4 stability, as it can support its weight throughout various movements, as well as achieve 6 DOF as per DR.3. The simple control of actuating individual solenoids simultaneously was suitable for achieving the design requirements of the spinal actuator segment, in which implementation of closed-loop control was out of the project's scope.

The movement achieved by the EM spinal segment can be seen in the following videos:

1. Vertical Translation1,Vertical Translation2
2. Rotation,Rotation (CW & CCW)
3. Extension
4. Bending,Cumulative Bending
5. Lateral Bending with a Rotation, Held Bend with Rotation
6. Lateral Translation 1, Lateral Translation 2
7. Multiple Sequenced Movements.

The vertical translation No.(1) of the EM Spinal segment mimics the ability of the spine to elongate from a compressed to a stretched state. This ability enables the segment to resist loads and translate the top platform, potentially lifting or moving an object to another plane. While the rotational movement No.(2) of 47° mimics the spine's ability to twist while the base remains stationary. A feature that is difficult to replicate in robots as shown in Section 2.6.2 Table 2.4. The extension of the platform shown in No.(3) serves a similar purpose as the lateral bending No.(4), but contributes to a different DOF. The platform's lateral bending, flexion and extension are critical characteristics as they mimic the motion of a spine that enables greater locomotion speed in quadruped and humanoid spines. The lateral translation No.(6) of the spine is minor, as this movement is observed in human spines as small cumulative bending motions laterally and transversely. However, lateral translation is also evident in how individual linear actuator legs adjust their position to accommodate the active bending. Finally, the combined movement of lateral bending and rotation, shown in No.(5), demonstrates the spinal section's ability to adjust its movement from one DOF to another. The ability to rotate whilst bending further mimics a human's spine capability and shows that the segment is capable of cumulative movement.7 shows all the movements in a sequence. The movements demonstrated above in Section 6.5.3 verify that the EM spinal segment achieved design requirement DR.1: capable of lateral bending, flexion and extension in 25°, DR.2: capable of rotation of 47°, DR.3: Capable of movement in 6 DOF and DR.4: Stability, ability to support its weight as well as DR.5 a fast response.

## 6.6 Matlab-Simulink Simulation and Closed-Loop Control

Implementing closed-loop control of the EM spinal segment actuator was beyond this project's scope; however, a virtual (twin) model was explored to demonstrate possible configurations and validate the open-loop movements. Incorporating closed-loop control into the EM actuator would necessitate the placement of six IMUs—one on each leg, one on the top platform, and six variable current controllers. This is due to the legs requiring feedback on their positional placement to achieve closed-loop control. Due to the thesis's objective of reproducing the motion of a spine with simplicity, closed-loop control was not implemented.

The simulated platform's closed-loop control enables the system to track a reference trajectory, whereas, in the implemented system, the platform follows a manual trajectory without sensory feedback. The following control system is an adapted Matlab-Simulink model Stewart Platform Example. The

simulation validates the implemented system and reiterates the rotations and translations achievable within the 6 DOF system. Further, it provides insights into the actuator leg positioning, displacement, and the force required by each leg to produce the various movements. The reference trajectories serve as inputs into the system, and the displacements and force require to meet the angular displacements and recorded and compared to the implemented system.

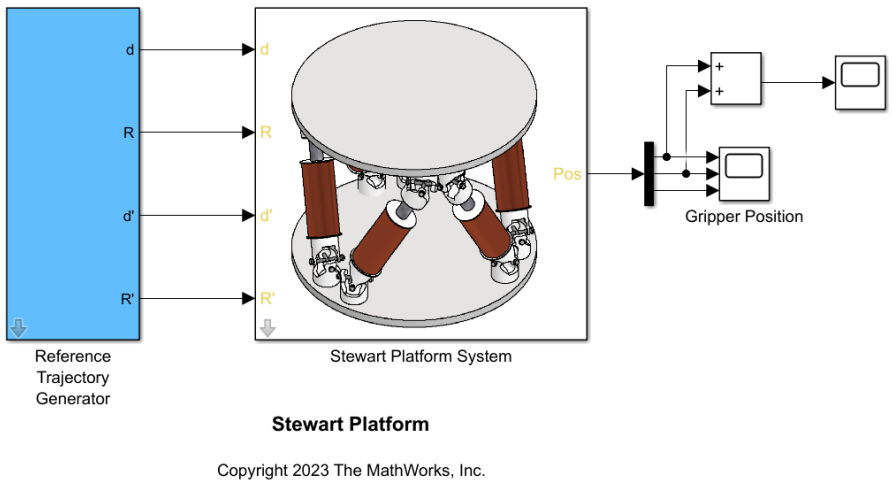


Figure 6.18: Simulink Platform

Figure 6.18 shows the overview of the Simulink model, in which, within the System Platform, the leg dimensions, masses, composition and system geometry are defined. The desired trajectory for the platform is input into the Reference Trajectory Generator, which represents the displacement and rotation in the X, Y and Z directions and the phase and frequency of the desired movement.

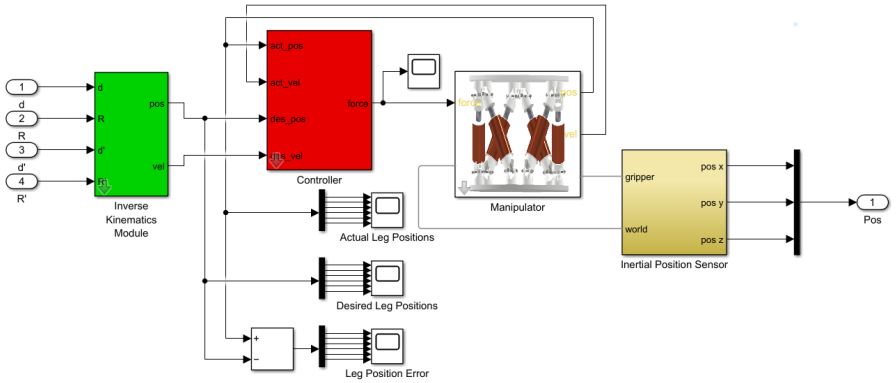


Figure 6.19: Inverse Kinematics and Dynamics

Figure 6.19 demonstrates the internal blocks of the Stewart Platform System from Figure 6.18. The desired trajectory becomes an input into the inverse kinematic model, with the system's controller ensuring the manipulator reaches the desired trajectory with a fast rise time, no oscillation and overshoot.

Using inverse kinematics, a lower-level PID controller commands each leg to correspond with the desired trajectory. The input to the controller is the actual leg position, velocity, and desired leg position. The error between the positions creates a force based on the error's gain and integral. The model's variables were adjusted to resemble those of the EM spinal segment actuator, therefore creating

a close approximation of the implemented system. The PID controller configuration in the system can be seen in Figure 6.20.

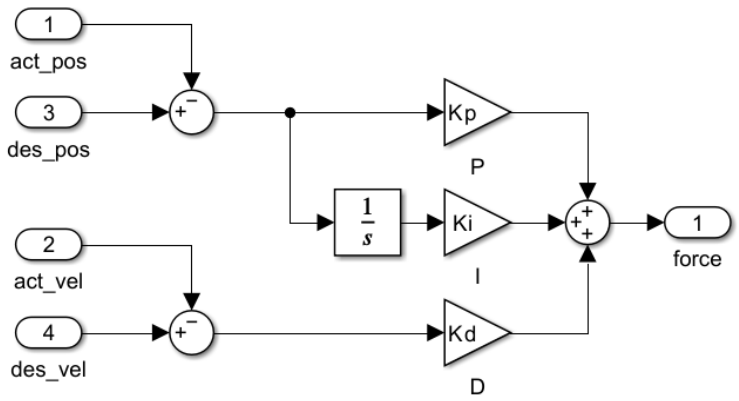


Figure 6.20: PID Controller

The PID values were established by tuning the controller, observing the overshoot, and settling time in the Simulink Control System Design Toolbox for the platform's vertical translation. Figure 6.21 shows the results from the Control System Design toolbox, where a reference trajectory of 4.5 cm was set for the top platform. The figure shows the rise and settling time of the response and produces the optimal values for the PID controller.

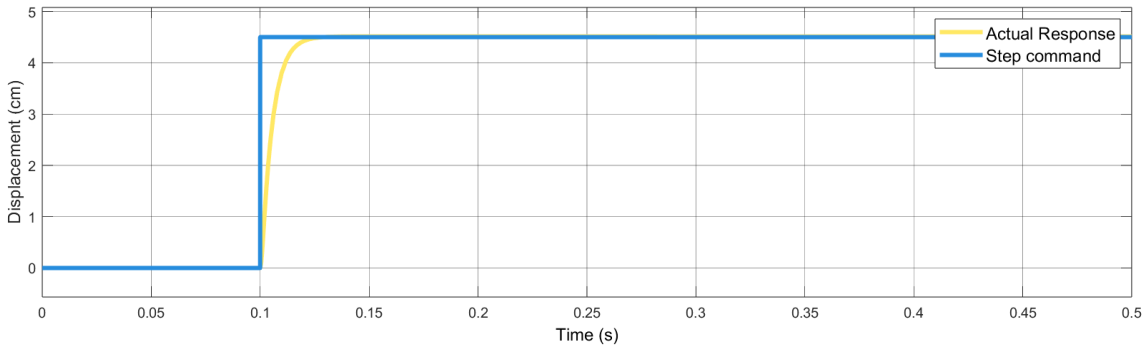


Figure 6.21: Vertical Translation Step Response

The values $Kp = 300$, $Ki = 50$, and $Kd = 2$ were then used to control other movement in the system. The simulation video (Vertical Step), demonstrates the response of the system to the step input.

The step input was initially used to determine the controller values for the Stewart Platform. However, to observe and evaluate the dynamic performance of the system, the step functions were replaced by sinusoidal inputs. Sinusoidal reference trajectories simulate cyclic motion, which tests the platform's ability to control dynamic movements. By using sinusoidal functions, the following simulations demonstrate the platform's stability and accuracy over time. Further, the sinusoidal input provides a smooth and continuous motion, which verifies the platform's ability to track a trajectory accurately. As a result, the leg position and force graphs for each actuator leg reflect the platform's response to a sinusoidal reference trajectory, showcasing its dynamic control capabilities.

### 6.6.1 MATLAB-Simulink Simulations

The following movements were created to mimic the implemented EM actuator movements. The first movement observed was vertical translation. Figures 6.22 and 6.23 are the results from the displacement and force scope in the Simulink system showing the vertical displacement of the top platform and the required force in each actuator leg, from leg 1 to leg 6. Each leg has its own controller, which controls the force required to meet the reference trajectory; the controller on the corresponding leg is shown in the legend.

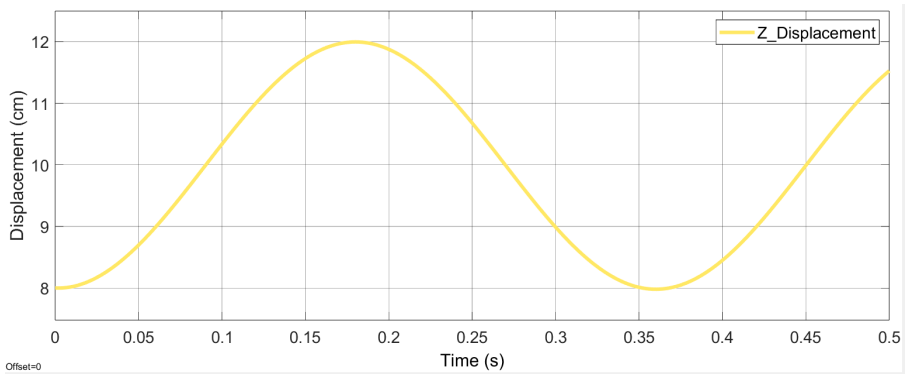


Figure 6.22: Z_displacement of the Top Platform

Figure 6.22 highlights that the platform moves to the reference trajectory vertically and then retracts cyclically. The cyclical movement of the platform is due to the sinusoidal reference trajectory input, which demonstrates the platform's ability to control dynamic movements. Figure 6.23 shows the force required to move the platform.

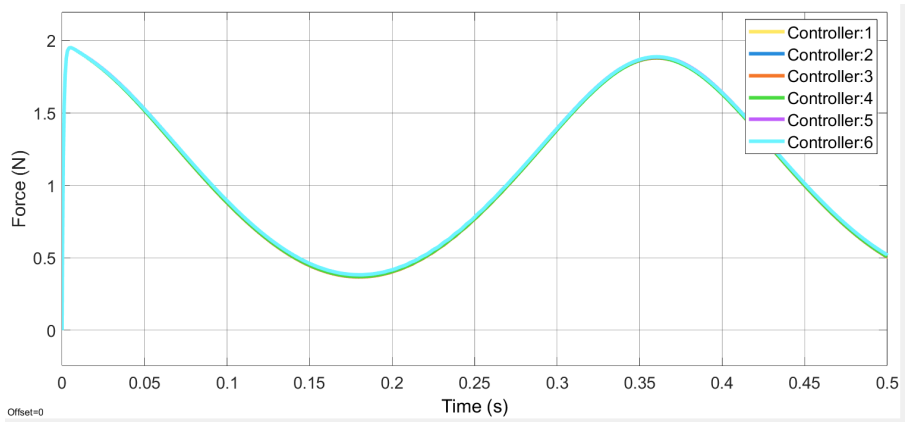


Figure 6.23: Force Corresponding to the Z_displacement for Each Leg

Figure 6.23 shows the force that each leg in the system requires to meet the reference trajectory; the control of each leg's force is shown in the legend. The vertical movement simulation video can be seen in (Vertical Movement) of the platform. The simulated force requirements for each leg correspond to the force results shown in the implemented system in Section 5.6 Solenoid-Plunger Implementation and Experimental Results, with a force of just under 2 N producing the 4 cm displacement. Figure 6.24 shows the error between the desired leg position from the reference trajectory and the actual leg position for each actuator leg in the system.

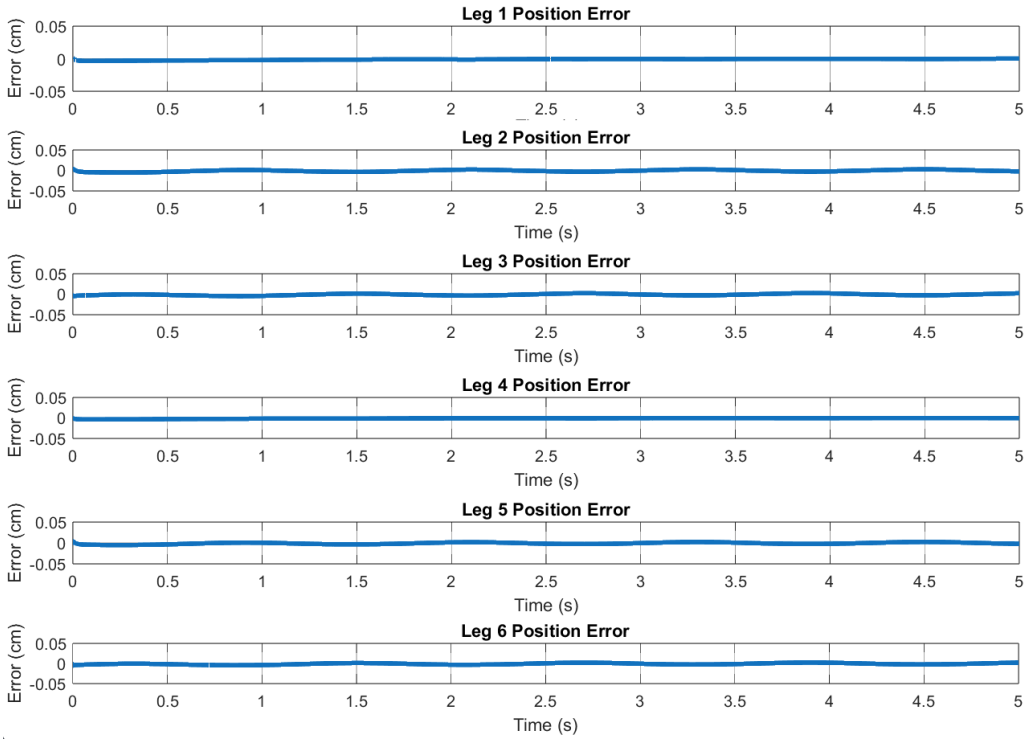


Figure 6.24: Leg Position Error

From Figure 6.24, it is clear that the controller values optimised successfully as the error in the position of each leg is less than 0.05 cm throughout the movement. Figure 6.24 demonstrates that the system achieved closed-loop control with minimal error.

### 6.6.2 Lateral Bending

To achieve lateral bending, the reference trajectory was set to 25° about the Y-Axis. Figure 6.25 shows the corresponding force required for lateral bending, and Figure 6.26 shows each actuator's actual leg position. The actual leg position of the actuator demonstrates how the control of each leg results in the desired movement. From Figures 6.25 and 6.26, the legs dominating lateral bending movement are Legs 1,2,3 and 4 as they alternate between extending and contracting each side of the platform, while legs 5 and 6 produce minimal movement but contribute to stability seen in their actuation force. Further, it can be seen that both the forces and the actual leg position are paired with two legs following the same trajectory and requiring the same force; the pairs are identified as Leg 1 and Leg 4, Leg 2 and Leg 3, and Leg 5 and Leg 6.

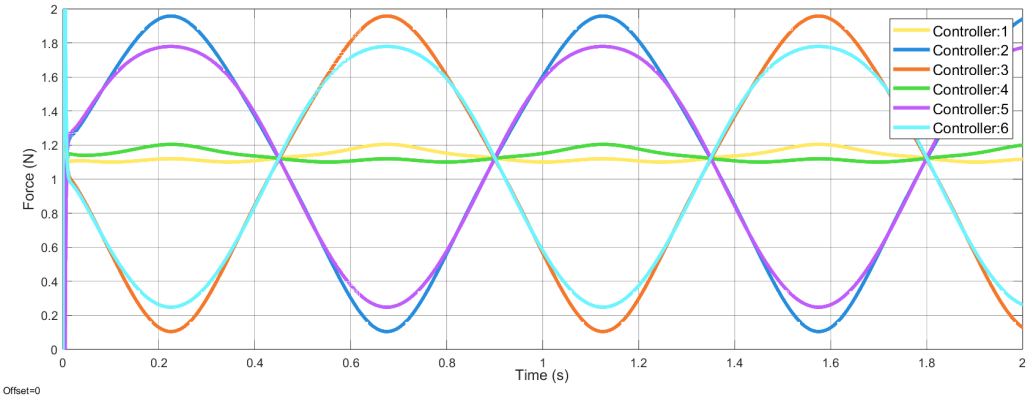


Figure 6.25: Lateral Bending Force per Leg Over Time

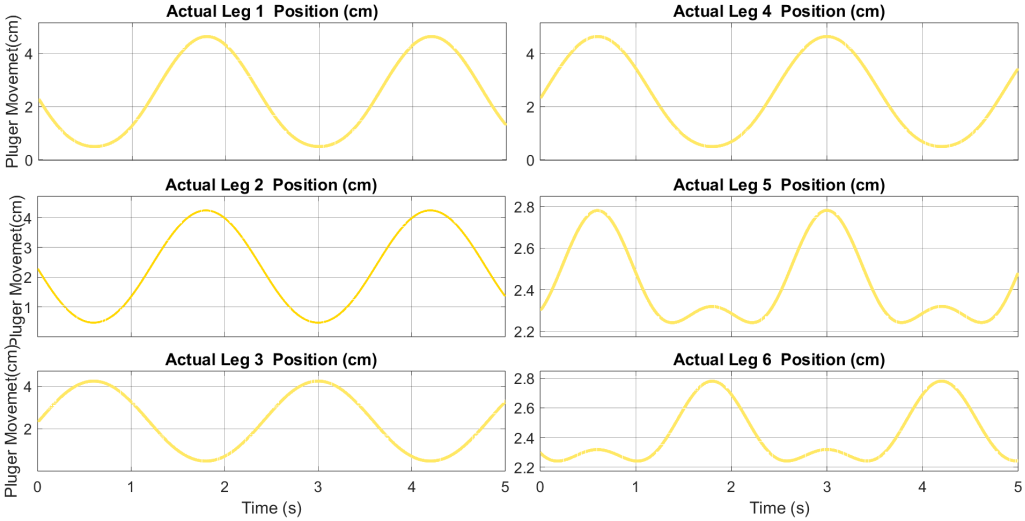


Figure 6.26: Lateral Bending Leg Position Over Time

Figure 6.25 and Figure 6.26 show that Leg 5 and Leg 6 produce minimal displacement; this is due to their placement along the Y axis, and therefore do not dominate the movement in lateral bending. The contribution of each leg is evident in the simulation video (Lateral Bending).

### 6.6.3 Flexion/Extension

Figures 6.27 and 6.28 show the force requirements and actual leg position, respectively, highlighting the difference between lateral bending and flexion/extension. Lateral bending involves two pairs of legs, whereas flexion and extension require all three: two for flexion and one for an extension. This is demonstrated through the simulation video (Flexion/Extension).

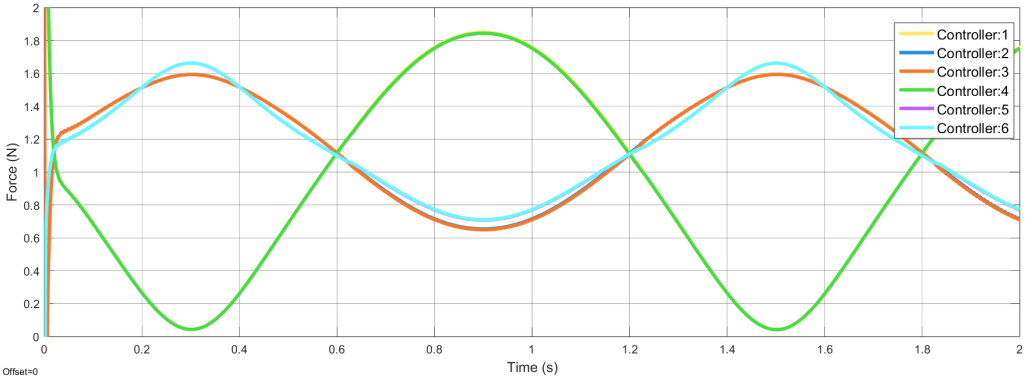


Figure 6.27: Flexion/Extension Force per Leg Over Time

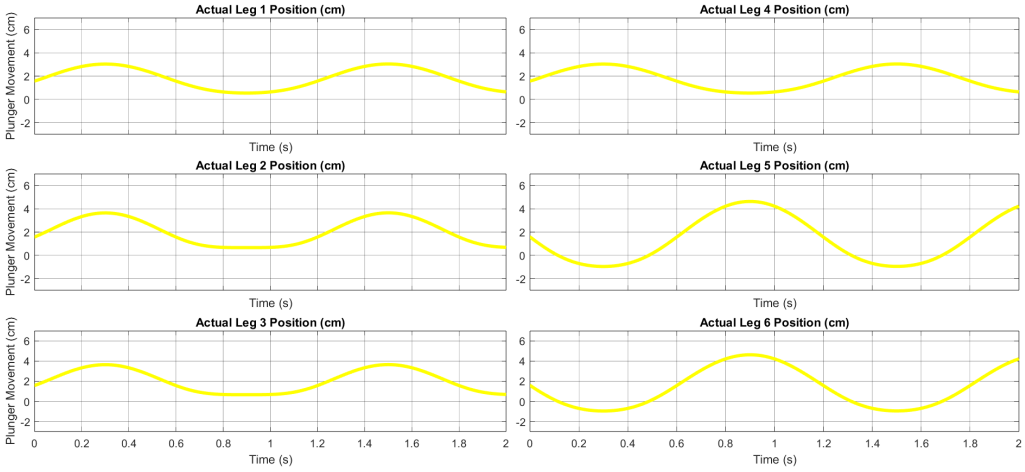


Figure 6.28: Flexion/Extension Leg Position Over Time

The force required shown in Figure 6.27 for flexion and extension is more consistent than the lateral bending, demonstrating how all the actuator legs are required for this movement. However, the movement is still achieved through leg pairs, with Leg 1 and 4, Leg 2 and 3, and Leg 5 and 6 following the same movement trajectory. The flexion/extension reference trajectory was 25° about the X-axis.

### 6.6.4 Rotational Movement

The rotational movement, force and actuator leg position for a 47° rotation are shown in Figures 6.29 and 6.30. From Figure 6.29, it is evident that the rotational movement requires a more significant force than the later bending and extension, with the force just over 2 N. Figure 6.30 highlights the actuator legs that contribute to CW and CCW movement, with Leg 1, Leg 3 and Leg 5 forming a rotation, and Leg 2, Leg 4 and Leg 6 forming the alternating rotation. The groups are distinguished by the line colours yellow and blue, highlighting how their leg positions follow one another, with the second group being 90° of out phase from the first.

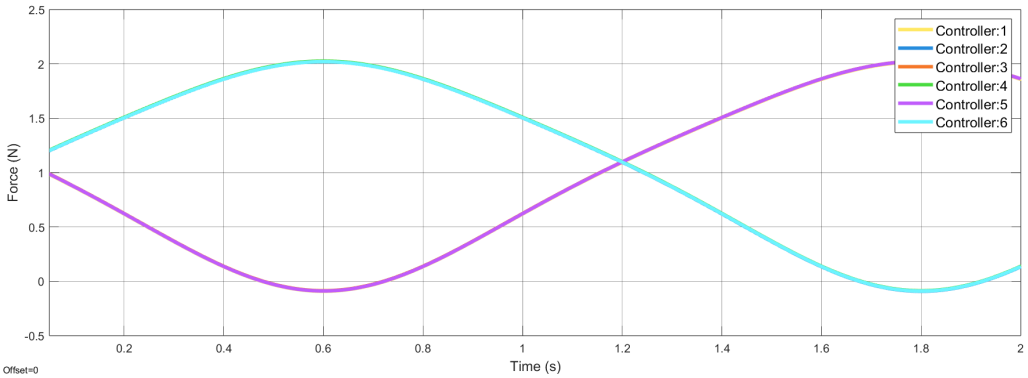


Figure 6.29: CW and CCW Force per Leg Over Time

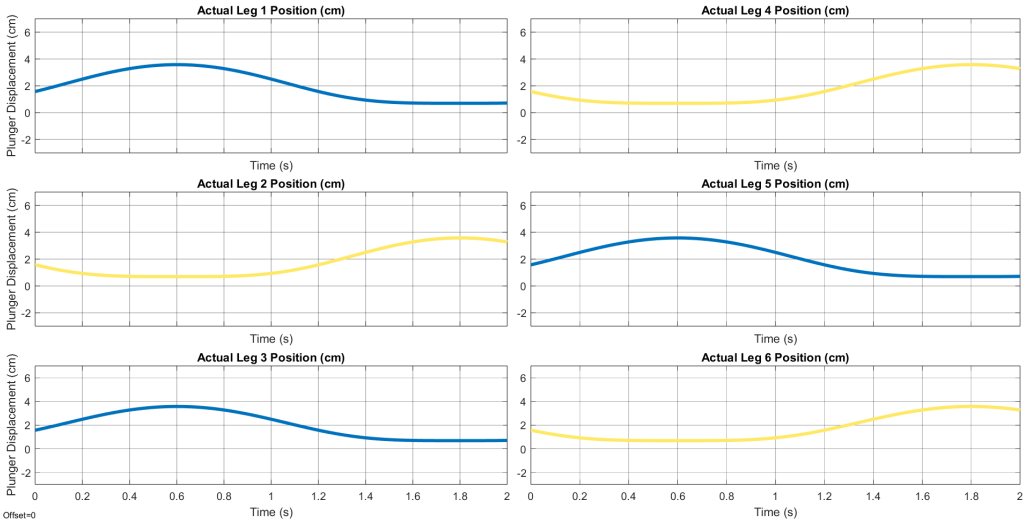


Figure 6.30: CW and CCW Leg Position Over Time

The CW and CCW rotation simulation video is demonstrated in (Rotational Movement).

### 6.6.5 Lateral Translation

Finally, lateral translation is achieved, with the forces and actuator leg positions shown in Figure 6.31 and Figure 6.32. The force required to produce the lateral translations is higher than that of other movements, with each actuator leg requiring different forces to produce the lateral translation. Once again, the leg positioning is achieved through pairs moving along the same trajectory, as shown in Figure 6.32.

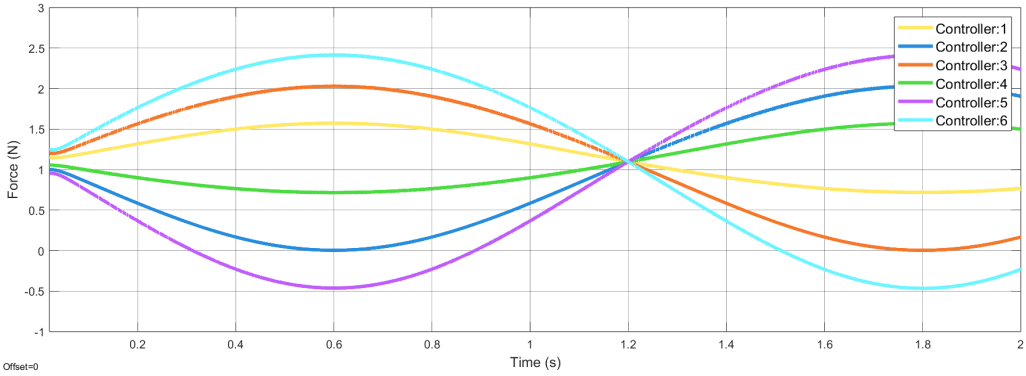


Figure 6.31: Lateral Translation Force Per Leg Over Time

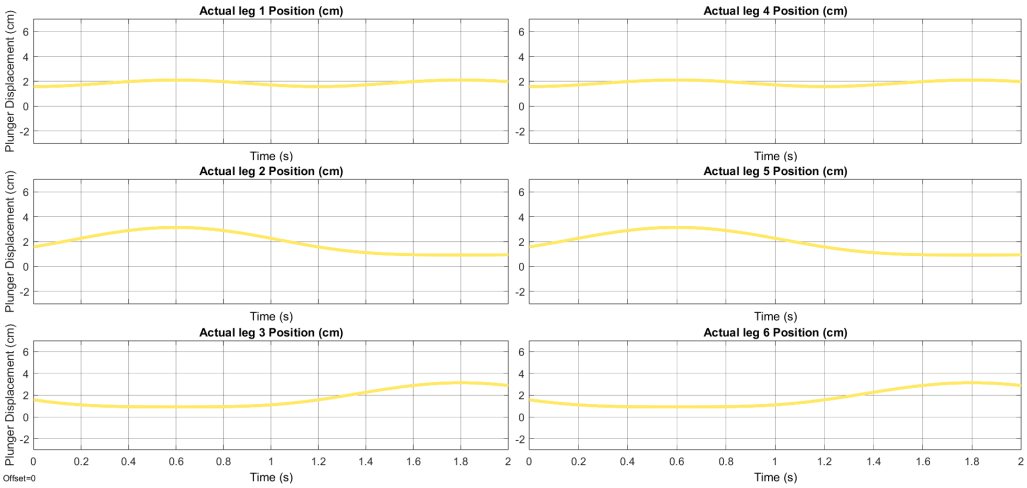


Figure 6.32: Lateral Translation Leg Position Over Time

The lateral translations simulation movement is shown in (Lateral Translations), where it is evident that all actuator legs contribute to the movement.

The virtual model of the EM spinal actuator is controlled to achieve the same DOF and range of motion as the implemented EM spinal actuator. It demonstrates how the actuators can be controlled through a reference trajectory instead of manually coding the excitement of individual solenoids. In addition, it provides a platform where environmental and sensor feedback in the actuator can be explored and observed. Through the control of the force, and therefore current supplied to each leg in the actuator, more complex movements can be achieved as shown in the following video of the simulation (Complex Movement). The Complex Movement video demonstrates the platform's ability to move in MDOF smoothly and efficiently.

## 6.7 Conclusion

The EM spinal segment actuator successfully achieved 6 DOF by utilising the optimised solenoid plunger in Chapter 5 and the benefits of parallel systems. The system's design mimics a Stewart platform, enabling its dynamic performance and stability. Through the individual excitation of solenoid plungers in each leg of the actuator, the platform achieved the desired movements of lateral bending, flexion, extension and rotation, effectively achieving the basic movements of a human spine segment. The segment further demonstrated that this movement can be achieved through open-loop control,

with the MATLAB Simulink model verifying the platform's ROM and providing insights into the force required by each actuator leg. However, the simulation achieved smoother rise times and displacements, indicating that a buffering zone can be included in the plunger's design in future systems to ensure smooth displacement and shock absorption. Despite this, the analytical solutions closely matched the IMU results, indicating that the actuators and plunger acted accurately and at high speeds.

The EM spinal segment actuator achieved its design requirements and enabled dynamic movement in 6 DOF with simple open-loop control. Its ability to mimic these complex motions contributes to research on electromagnetic spinal actuators. The success of the actuator is attributed to the design and optimisation methodology carried out in Chapter 5, which ensures that the system performs optimally, is adaptable, replacement and configurable.

Table 6.2 demonstrates the movement of the implemented system and the MATLAB Simulink model.

Table 6.2: Implemented EM actuator Movement compared to MATLAB Simulink Model

| **Movement** | **Implemented** | **MATLAB** |
|---|---|---|
| Vertical Translation | Vertical Translation1,Translation2 | Vertical Translation1,Translation2 |
| Lateral Bending | Bending, Bending2 | Bending |
| Flexion/Extension | Extension/Flexion | Extension |
| Rotation | Rotation1, Rotation2 | Rotation |
| Bending & Rotation | Rotation & Lateral Bending | Rotation & Lateral Bending |
| Lateral Translation | Lateral Translation 1 ,Lateral Translation 2 | Lateral Translation |
| Complex Movement | Multiple Sequenced Movements. | Multiple Sequenced Movements |
| Prototype 1 | The First Prototype | - |

## 6.8 Commercial Comparison

Table 6.3: Comparison of Custom Solenoid Plunger with Commercial Linear Actuators

| **Metric** | **Custom Solenoid Plunger (C2)** | **Commercial Tubular Solenoid** | **High Performance Solenoid** | **Commercial Electro-Mechanical** |
|---|---|---|---|---|
| **Core Functionality** | **3 DOF/Leg** (Linear + Roll + Pitch) integrated via Universal Joints | 1 DOF (Pull/Push Only) | 1 DOF (Fast Pull/-Push Only, Square Form) | 1 DOF (High Force Linear, Screw/Belt Driven) |
| **Max Force ($F_{max}$)** | **4.09** N (at 2.0 A peak) | Up to **80** N (Intermittent Duty at short stroke) | Up to **160** N (Short-stroke, high-power density) | Up to **15,000** N (Requires bulky motor/gearbox) |
| **Stroke Length ($d_{max}$)** | **45** mm (4.5 cm), large stroke relative to solenoid length | Up to **30** mm, typical range is **5** mm to **10** mm | Up to **20** mm, optimized for rapid short distance | Up to **1,200** mm, designed for large industrial displacements |
| **Linear Speed (v)** | $\approx$ **661** mm/s (for full 45 mm stroke) | Response Time $\approx$ 10 ms $-$ 50 ms (for short stroke activation) | Pull-in time $<$ **30** ms (Very fast activation) | Max Speed $\approx$ **160** mm/s (Slower due to mechanics) |
| **Force/Volume (F/V)** | $8.25 \times 10^{-2}$ N/cm$^3$ (Optimized for balance and continuous duty operation trade-off) | Optimized for size, generally higher F/V at **short** actuation distance | High F/V ratio due to square form factor and high current density | Lower ratio per unit length due to gear and motor volume |
| **Thermal Management** | **Optimized** for continuous operation and low temperature rise ($\Delta T = 15°$C at 0.92 A) | Requires specific heat sinking or low duty cycle for thermal management | Designed to manage high heat with thermal class F materials | Duty cycle limits often dictated by system heat generation |
| **Links** | ThesisImplemented | Geeplus Tubular Solenoids | Kendrion LHP Series | LINAK LA36 Series |

The comparison clearly demonstrates that while commercial options offer either extreme force/stroke (linear actuators) or simple, fast on/off operation (standard solenoids), none integrate the required 3 DOF functionality nor are they specifically optimized for the unique, tight volumetric constraints and dynamic force/heat balance necessary for the spinal segment.

# Chapter 7

# Conclusions, Research Contributions and Future Recommendations

The use of electromagnetism in the actuators throughout this thesis has proven its effectiveness in providing actuation across multiple degrees of freedom (MDOF). The DH actuator in Chapter 4 explored the use of a single coil as an actuator for magnetic devices, focusing on its ability to generate multidirectional motion through simple control. The ability of the DH actuator to produce both perpendicular and parallel magnetic fields provides significant improvements over traditional single-axis coil systems, which have limited DOF. The experimental and simulation results confirmed that the DH structure can move a magnetic block in both vertical and horizontal directions by controlling the input current, meeting the design requirement of a versatile actuator. The effect of the tilt angle of the DH was highlighted through the optimisation and sensitivity analysis, demonstrating that at 60° the strongest dipole forces were generated whilst minimising the solenoid field interference. Further, the sensitivity, thermal and optimisation analysis emphasised the importance of variable selection and the interactions between the system components.

Despite the DH producing bidirectional motion of a magnetic block and effectively generating forces in multiple directions, its application in the spinal actuator system was not realised due to insufficient stroke length. The coil's compact design restricts large displacements, which must be addressed in future designs. The displacement the actuator achieves limits its application to close proximity magnetic movement, suggesting its application lies in micro-magnetic device manoeuvrability. Large-scale applications, such as a spinal actuator requiring extended displacement, necessitate enhancing the capabilities of the Double Helix (DH) actuator and integrating it into a 6-DOF system. Despite this, using a single coil to produce motion in multiple directions demonstrated that MDOF can be achieved through simplicity.

The benefits of electromagnetism discovered in Chapter 4, such as fast response, simple control, and modularity, stimulated the design of the solenoid plunger. The solenoid plunger in Chapter 5 forms a solution to the limited stroke length of the DH actuator in Chapter 4. The solenoid plunger aimed to achieve 3 DOF in the system while being capable of integration into the 6 DOF parallel spinal segment manipulator. The mechanical design and system integration of material and geometry proved critical in providing movement in multiple directions, effectively meeting the modularity and scalability design requirements. Notably, the use of universal joints to connect the magnet to the end effector facilitated both roll and pitch movements. Likewise, using neodymium magnets housed within the solenoid produced vertical motion with a considerable stroke length and high forces, allowing the

system to overcome its weight.

The analytical and FEA solutions of the electromagnetic forces within the solenoid plunger made significant contributions by establishing a framework for modelling the movement of the magnet within the solenoid through the control of the current. The analysis highlights the key variables affecting the system's performance, enabling their isolation and optimisation. Unlike most robotic designs, the actuator in the system is thoroughly optimised, highlighting the significance of the variables that contribute to the overall performance of the actuator. The FEA simulation and Sensitivity analysis in ANSYS quantified the contributions of the variables discovered in the analytical solutions. The key parameters identified, current, wire diameter, and solenoid dimensions, enabled the effective optimisation and the subsequent thermal management of the system. Therefore, using analytical and simulation tools to supplement one another is highlighted as an effective validation method and an enhanced method of exploring design variables trade-offs. Further, the multi-objective optimisation of maximising force while minimising volume and managing thermal effects led to identifying optimal configurations that met the requirements for a compact and efficient actuator.

Another significant contribution was the thermal analysis, which addressed the standard limitation of electromagnetic actuation - thermal management. By simulating and experimentally validating the system's temperature increase, the operational limits and maximum driving current were established, ensuring the system's longevity and continued optimal performance. This contribution provides insights into the design of actuators with known limits and operating ranges. The force measurements accurately validated the simulations and analytical solutions, demonstrating the effectiveness of the design, with the system producing a sufficient stroke length of 4.5 cm. Overall, the solenoid plunger demonstrates the effectiveness of optimisation and simple control in achieving MDOF motion, high force output, and thermal management. The design's precision, speed, and simplicity provide a foundation for its extension into a parallel system capable of 6 DOF.

Building on Chapters 4 and 5, the electromagnetic spinal segment actuator in Chapter 6 successfully extends the linear solenoid plunger system into a parallel platform capable of achieving 6 DOF. One contribution of the electromagnetic spinal segment actuator is its ability to create complex motions through simple current control. The design effectively utilises the stroke length of the magnet to enable its movement, removing the need for additional structures such as cables and tendons. Furthermore, the ability of the solenoid plunger to create movement in two directions within a plane enables the control of individual solenoids, providing additional movement capabilities.

A key research contribution is the use of the Stewart configuration in the application of an electromagnetic spinal segment actuator, which deviates from traditional spinal design and actuation methodologies. The system combines the advantages of electromagnetic actuation with the precision and stability of parallel mechanisms, forming an efficient spinal actuator base. The parallel system overcomes the limitations of serial spinal actuators and enables the system to achieve the desired flexibility and precision whilst maintaining stability.

The dynamic analysis of the system provided insights into the relationship between the gravitational forces, actuation forces and the resulting displacement of both the magnet and the platform. Through the system's dynamic analysis, the solenoid plunger's tilt angle was highlighted as a key factor determining the rotation and bending of the top platform, with the design requirements enabling the

successful selection of a 60° tilt. By adjusting the tilt angle of the solenoid plunger and controlling the input current, the system was able to generate the desired rotational and translational movements of the top platform. Further, the use of the universal joints improved the system's adaptability and response, enabling the platform to adjust to various movements without collapsing. The system's dynamic modelling, including the solenoid plunger's behaviour, was validated by the measurements on the IMU, showcasing the system's precision and fast response.

The implementation of the serial actuators in the parallel Stewart system enabled the spinal actuators' range of motion, configurable stiffness, and stability. The configuration allowed the system to achieve the required flexibility and precision for spinal segment movements, such as lateral bending, flexion, extension and rotation, whilst maintaining compactness and high operational performance. The ability to perform the movement in six directions with minimal complexity in the control algorithms highlights the advantages of electromagnetism in spinal manipulators and humanoid movement.

The six solenoid plungers arranged in pairs around the platform facilitated all the necessary motions for robotic spines, including vertical displacement, with a focus on rotation and lateral bending. An added benefit from the design is that each leg can be changed on-line, with the system still capable of performing the same movement with one leg disabled. The system's ability to achieve this movement with minimal complexity in control is a significant contribution to spinal actuation in humanoid robots.

The successful implementation of the EM spinal actuator also involved extensive testing and validation. Experimental results demonstrated that the platform achieved the design specifications of 25° lateral bending and flexion/extension, 47° rotation, as well as a combination of the two movements and 4.5 cm vertical displacement, with fast response times and stability during operation. The ROM achieved by the EM spinal segment mimics those of the human thoracic spine, highlighting the effectiveness of electromagnetic actuation in realising dynamic movement. The results from the experimental testing were closely aligned with the analytical predictions, confirming the accuracy and reliability of the design and its capability to support its weight. The experimental validation confirms that the designed system is functional and adaptable to various real-world applications, particularly in spinal robotics.

Additionally, the research utilised simulation tools such as MATLAB and Simulink to develop a virtual model of the 6-DOF platform, enhancing the understanding of the actuator legs and their role in enabling real-time dynamic movements. The Simulink model enabled the simulation of complex movements, providing a foundation for future work on the actuator's performance.

A future recommendation would be to design different-sized EM spinal segments for implementation in different-sized robots. The structure of the EM spinal segment is versatile, enabling its use in large humanoid robots, smaller quadruped robots, and even insect-like robots. Including increased ROM and DOF in these robots would enable movement versatility and task availability from explorative research to manufacturing tasks.

Implementing the EM spinal segment into a humanoid would require the segments to be stacked on one another, elongating the spine and doubling the achievable ROM. The stack of EM spinal segments could decrease in size, with the largest at the base, mimicking animal vertebrae. From this, the tiered system would ensure stability and a stable centre of mass whilst enabling more considerable bending and flection angles. In cases where the spinal segment is used to bear a large load, a future recommendation

is to utilise carbon fibre as the material surrounding the magnet, binding the coil and the base and top platform. Carbon fibre would ensure the system remains lightweight and agile and withstand larger loads.

In future work, a spring or cushioning mechanism will be introduced into the base of the EM linear actuator to ensure the movement of the plunger is smooth and that shocks can be effectively absorbed. Other future work includes limb attachment to the segment, beginning with a gripper arm, and utilising the platform's bending, flexion and rotational capabilities to accurately move the gripper arm to move objects nearby. Furthermore, the EM segment will be fitted with a central column running through the middle of the platform, enabling limb and other extensions to attach to the system. The central column will be a flexible tubing that bends and turns with the platform.

Overall, the research presented in this thesis contributes to spinal robotics by proposing a unique solution using electromagnetic actuation in a parallel mechanism. Integrating solenoid-plunger actuators into a 6 DOF spinal segment offers a simple and efficient alternative to traditional actuator technologies, demonstrating the potential for scalability, quick response, and precision in applications such as humanoid robot spines. These contributions represent a significant step forward in developing spinal robots capable of performing complex, multi-directional movements with high accuracy and low power consumption.

# Bibliography


[1] J. Savlovskis. (2022) Anatomy standard. [Online]. Available: https://www.anatomystandard.com/biomechanics/spine/rom-of-spine.html

[2] P. Gas, "Behavior of helical coil with water cooling channel and temperature dependent conductivity of copper winding used for mfh purpose," *IOP Conference Series Earth and Environmental Science*, vol. 214, pp. 1–11, 01 2019.

[3] K. Lynch, *Modern Robotics*. Cambridge University Press, 2017.

[4] C. Liang and M. Ceccarelli, "Design and simulation of a waist–trunk system for a humanoid robot," *Mechanism and Machine Theory*, vol. 53, pp. 50–65, 2012.

[5] T. X. Tien and D. Cirkl, "Solution of inverse dynamics of stewart–gough platform using substructure technique," *Journal of Theoretical and Applied Mechanics*, vol. 59, no. 3, pp. 329–342, 2021. [Online]. Available: https://doi.org/10.15632/jtam-pl/136057

[6] M. Expert. (2025) Magnetic properties of ferrite magnets. ellis mather group. [Online]. Available: https://www.magnetexpert.com/magnetic-properties-of-ferrite-magnets

[7] M. Singh, S. Chatterjee, G. Bhandari, and H. Singh, "Design and simulation of an improved structure of spine for humanoid," in *2023 International Conference on IoT, Communication and Automation Technology (ICICAT)*, 2023, pp. 1–6.

[8] I. Mizuuchi, T. Yoshikai, Y. Nakanishi, and M. Inaba, "A reinforceable-muscle flexible-spine humanoid 'kenji'," in *2005 IEEE/RSJ International Conference on Intelligent Robots and Systems*, 2005, pp. 4143–4148.

[9] Q. Zhang, T. Li, M. Luo, and P. Yao, "From human spine to humanoid robot torso," in *2016 IEEE International Conference on Mechatronics and Automation*, 2016, pp. 1161–1166.

[10] M. Penčić, B. Borovac, D. Kovacevic, and M. Čavić, "Development of the multi-segment lumbar spine for humanoid robots," *Thermal Science*, vol. 20, 08 2016.

[11] M. H. H. Kani, M. Derafshian, H. J. Bidgoly, and M. N. Ahmadabadi, "Effect of flexible spine on stability of a passive quadruped robot: Experimental results," in *2011 IEEE International Conference on Robotics and Biomimetics*, 2011, pp. 2793–2798.

[12] H. G. Marques, M. Jäntsch, S. Wittmeier, O. Holland, C. Alessandro, A. Diamond, M. Lungarella, and R. Knight, "Ecce1: The first of a series of anthropomimetic musculoskeletal upper torsos," in *2010 10th IEEE-RAS International Conference on Humanoid Robots*, 2010, pp. 391–396.

[13] Q. Zhao, H. Sumioka, K. Nakajima, X. Yu, and R. Pfeifer, "Spine as an engine: effect of spine morphology on spine-driven quadruped locomotion," *Advanced Robotics*, vol. 28, no. 6, pp. 367–378, 2014.

[14] K. Weinmeister, P. Eckert, H. Witte, and A.-J. Ijspeert, "Cheetah-cub-s: Steering of a quadruped robot using trunk motion," in *2015 IEEE International Symposium on Safety, Security, and Rescue Robotics (SSRR)*, 2015, pp. 1–6.

[15] B. Ku, Y. Tian, S. Wang, E. Libbos, S. Agrawal, and A. Banerjee, "A distributed and scalable electromechanical actuator for bio-inspired robots," in *2019 IEEE International Electric Machines and Drives Conference (IEMDC)*, 2019, pp. 2180–2187.

[16] C. Cibert and V. Hugel, "Compliant intervertebral mechanism for humanoid backbone: Kinematic modeling and optimization," *Mechanism and Machine Theory*, vol. 66, pp. 32–55, 2013. [Online]. Available: https://www.sciencedirect.com/science/article/pii/S0094114X13000645

[17] B. Ku, Y. Tian, S. Wang, E. Libbos, S. Agrawal, and A. Banerjee, "A distributed and scalable electromechanical actuator for bio-inspired robots," in *2019 IEEE International Electric Machines and Drives Conference (IEMDC)*, 2019, pp. 2180–2187.

[18] A. Heya, T. Mototsuji, and K. Hirata, "Experimental verification and analysis of six-degree-of-freedom electromagnetic actuator with short-stroke," *IEEE Transactions on Energy Conversion*, vol. 39, no. 2, pp. 795–804, 2024.

[19] C. Wang, S. Lu, C. Zhang, J. Gao, B. Zhang, and S. Wang, "Design and dynamic modeling of a 3-rps compliant parallel robot driven by voice coil actuators," *Micromachines*, vol. 12, no. 12, 2021. [Online]. Available: https://www.mdpi.com/2072666X/12/12/1442

[20] C.-W. Chang Song and S.-Y. Lee, "Design of a solenoid actuator with a magnetic plunger for miniaturized segment robots," *Applied Sciences*, vol. 5, no. 3, pp. 595–607, 2015. [Online]. Available: https://www.mdpi.com/2076-3417/5/3/595

[21] C.-W. Song, D.-J. Lee, and S.-Y. Lee, "Bioinspired segment robot with earthworm-like plane locomotion," *Journal of Bionic Engineering*, vol. 13, no. 2, pp. 292–302, 2016. [Online]. Available: https://www.sciencedirect.com/science/article/pii/S1672652916603025

[22] A. Fukuhara, M. Gunji, and Y. Masuda, "Comparative anatomy of quadruped robots and animals: a review," *Advanced Robotics*, vol. 36, pp. 1–19, 06 2022.

[23] L. Wu and Y. Tadesse, "Musculoskeletal system for bio-inspired robotic systems based on ball and socket joints," p. V04AT05A020, 11 2016.

[24] S. Seok, A. Wang, M. Y. Chuah, D. J. Hyun, J. Lee, D. M. Otten, J. H. Lang, and S. Kim, "Design principles for energy-efficient legged locomotion and implementation on the mit cheetah robot," *IEEE/ASME Transactions on Mechatronics*, vol. 20, no. 3, pp. 1117–1129, 2015.

[25] C. Lytridis, V. G. Kaburlasos, T. Pachidis, M. Manios, E. Vrochidou, T. Kalampokas, and S. Chatzistamatis, "An overview of cooperative robotics in agriculture," *Agronomy*, vol. 11, no. 9, p. 1818, 2021.

[26] A. Bonci, P. D. Cen Cheng, M. Indri, G. Nabissi, and F. Sibona, "Human-robot perception in industrial environments: A survey," *Sensors*, vol. 21, no. 5, p. 1571, 2021.

[27] T. P. Huck, C. Ledermann, and T. Kroger, "Testing robot system safety by creating hazardous human worker behavior in simulation," *IEEE Robotics and Automation Letters*, vol. 7, no. 2, pp. 770–777, 2021.

[28] C. Liang, M. Ceccarelli, and G. Carbone, "Experimental characterization of operation of a waist-trunk system with parallel manipulators," *Chin. J. Mech. Eng*, vol. 24, no. 5, pp. 713–722, 2011.

[29] Z. Mchedlishvili, D. Tavkhelidze, T. Mchedlishvili, and J. Uplisashvili, "Geometry and kinematics of tripod mechanisms," *IHJVT< B*, 2017.

[30] Y. Tong, H. Liu, and Z. Zhang, "Advancements in humanoid robots: A comprehensive review and future prospects," *IEEE/CAA Journal of Automatica Sinica*, vol. 11, pp. 301–328, 02 2024.

[31] D. Chen, Q. Liu, L. Dong, H. Wang, and Q. Zhang, "Effect of spine motion on mobility in quadruped running," *Chinese Journal of Mechanical Engineering*, vol. 27, pp. 1150–1156, 11 2014.

[32] Z. Qian, E. Benjamin, S. Hidenobu, S. Timothy, and P. Rolf, "The effect of spine actuation and stiffness on a pneumatically-driven quadruped robot for cheetah-like locomotion," in *2013 IEEE International Conference on Robotics and Biomimetics (ROBIO)*, 2013, pp. 1807–1812.

[33] S. Shield, N. Muramatsu, Z. Silva, and A. Patel, "Chasing the cheetah: how field biomechanics has evolved to keep up with the fastest land animal," *The Journal of experimental biology*, vol. 226, 04 2023.

[34] B. Kim, D. Kim, J. Jung, and J.-O. Park, "A biomimetic undulatory tadpole robot using ionic polymer–metal composite actuators," *Smart Materials and Structures*, vol. 14, pp. 1579–1585, 2005.

[35] V. K. Venkiteswaran, L. F. P. Samaniego, J. Sikorski, and S. Misra, "Bio-inspired terrestrial motion of magnetic soft millirobots," *IEEE Robotics and Automation Letters*, vol. 4, no. 2, pp. 1753–1759, 2019.

[36] J. Rossiter and H. Hauser, "Soft robotics - the next industrial revolution?" *IEEE Robotics and Automation Magazine*, vol. 23, no. 3, pp. 17–20, 2016.

[37] M. P. Nemitz, P. Mihaylov, T. W. Barraclough, D. Ross, and A. A. Stokes, "Using voice coils to actuate modular soft robotic: Wormbot, an example," *Soft Robtics*, vol. 3, pp. 198–204, 2016.

[38] S. Pouya, M. Khodabakhsh, A. Sproewitz, and A. Ijspeert, "Spinal joint compliance and actuation in a simulated bounding quadruped robot," *Autonomous Robots*, pp. 437—452, Feb. 2017. [Online]. Available: https://link.springer.com/article/10.1007/s10514-015-9540-2

[39] W. R. Johnson, S. J. Woodman, and R. Kramer-Bottiglio, "An electromagnetic soft robot that carries its own magnet," in *2022 IEEE 5th International Conference on Soft Robotics (RoboSoft)*, 2022, pp. 761–766.

[40] Y. Nakanishi, S. Ohta, T. Shirai, Y. Asano, T. Kozuki, Y. Kakehashi, H. Mizoguchi, T. Kurotobi, Y. Motegi, K. Sasabuchi *et al.*, "Design approach of biologically-inspired musculoskeletal humanoids," *International Journal of Advanced Robotic Systems*, vol. 10, no. 4, p. 216, 2013.

[41] T. Kamimura, K. Sato, S. Aoi, Y. Higurashi, N. Wada, K. Tsuchiya, A. Sano, and F. Matsuno, "Three characteristics of cheetah galloping improve running performance through spinal movement: A modeling study," *Frontiers in bioengineering and biotechnology*, vol. 10, 4 2022.

[42] O. Matsumoto, H. Tanaka, T. Kawasetsu, and K. Hosoda, "High-speed running quadruped robot with a multi-joint spine adopting a 1dof closed-loop linkage," *Frontiers in Robotics and AI*, vol. 10, 03 2023.

[43] Z. Qian, E. Benjamin, S. Hidenobu, S. Timothy, and P. Rolf, "The effect of spine actuation and stiffness on a pneumatically-driven quadruped robot for cheetah-like locomotion," in *2013 IEEE International Conference on Robotics and Biomimetics (ROBIO)*, 2013, pp. 1807–1812.

[44] Z. Qian, N. Kohei, S. Hidenobu, Y. Xiaoxiang, and P. Rolf, "Embodiment enables the spinal engine in quadruped robot locomotion," in *2012 IEEE/RSJ International Conference on Intelligent Robots and Systems*, 2012, pp. 2449–2456.

[45] A. Ijspeert, "Amphibious and sprawling locomotion: From biology to robotics and back," *Annual Review of Control, Robotics, and Autonomous Systems*, vol. 3, pp. 1–21, 05 2020.

[46] A. Fukuhara, Y. Koizumi, S. Suzuki, T. Kano, and A. Ishiguro, "Decentralized control mechanism for body–limb coordination in quadruped running," *Adaptive Behavior*, vol. 28, p. 105971231986518, 08 2019.

[47] D. Chen, N. Li, H. Wang, and L. Chen, "Effect of flexible spine motion on energy efficiency in quadruped running," *Journal of Bionic Engineering*, vol. 14, no. 4, pp. 716–725, 2017. [Online]. Available: https://www.sciencedirect.com/science/article/pii/S1672652916604365

[48] I. Mizuuchi, T. Yoshikai, Y. Sodeyama, Y. Nakanishi, A. Miyadera, T. Yamamoto, T. Niemela, M. Hayashi, J. Urata, Y. Namiki, T. Nishino, and M. Inaba, "Development of musculoskeletal humanoid kotaro," in *Proceedings 2006 IEEE International Conference on Robotics and Automation, 2006. ICRA 2006.*, 2006, pp. 82–87.

[49] G. Runge, S. Zellmer, T. Preller, G. Garnweitner, and A. Raatz, "Actuation principles for the bioinspired soft robotic manipulator spineman," in *2015 IEEE International Conference on Robotics and Biomimetics (ROBIO)*, 2015, pp. 1329–1336.

[50] I. Mizuuchi, R. Tajima, T. Yoshikai, D. Sato, K. Nagashima, M. Inaba, Y. Kuniyoshi, and H. Inoue, "The design and control of the flexible spine of a fully tendon-driven humanoid 'kenta'," in *IEEE/RSJ International Conference on Intelligent Robots and Systems*, vol. 3, 2002.

[51] C. Cibert and V. Hugel, "Bio-inspired compliant spine for humanoid robot a degrees of freedom challenge," in *2012 IEEE RO-MAN: The 21st IEEE International Symposium on Robot and Human Interactive Communication*, 2012, pp. 1–5.

[52] I. Georgilas and V. Tourassis, "From the human spine to hyperredundant robots: The ermis mechanism," *ISRN Robotics*, vol. 2013, 01 2013.

[53] M. Inaba, I. Mizuuchi, R. Tajima, T. Yoshikai, D. Sato, K. Nagashima, and H. Inoue, "Building spined muscle-tendon humanoid," in *Robotics Research: The Tenth International Symposium*. Springer, 2003, pp. 113–127.

[54] T. Yoshikai, I. Mizuuchi, D. Sato, S. Yoshida, M. Inaba, and H. Inoue, "Behavior system design and implementation in spined musle-tendon humanoid'' kenta'','' *Journal of Robotics and Mechatronics*, vol. 15, no. 2, pp. 143–152, 2003.

[55] Y. Nakanishi, T. Izawa, M. Osada, N. Ito, S. Ohta, J. Urata, and M. Inaba, "Development of musculoskeletal humanoid kenzoh with mechanical compliance changeable tendons by nonlinear spring unit," in *2011 IEEE International Conference on Robotics and Biomimetics*. IEEE, 2011, pp. 2384–2389.

[56] F. Fries, S. Miyashita, D. Rus, R. Pfeifer, and D. D. Damian, "Electromagnetically driven elastic actuator," in *2014 IEEE International Conference on Robotics and Biomimetics (ROBIO 2014)*, 2014, pp. 309–314.

[57] B. H. Shin, K.-M. Lee, and S.-Y. Lee, "A miniaturized tadpole robot using an electromagnetic oscillatory actuator," *J Bionic Eng*, vol. 12, pp. 29–36, 2015.

[58] W. Chen, V. R. Puranam, M. Sarthak, and V. V. Kalpathy, "A snake-inspired multi-segmented magnetic soft robot towards medical applications," *IEEE Robotics and Automation Letters*, vol. 7, no. 2, pp. 5795–5802, 2022.

[59] B. Liao, Z. Li, and D. Ruxu, "Robot tadpole with a novel biomimetic wire-driven propulsor," in *2012 IEEE International Conference on Robotics and Biomimetics (ROBIO)*, 2012, pp. 557–562.

[60] B. Piotr, G. Franciszek, and P. Łukasz, "E-morph as a new adaptive actuator for soft robotics," *IEEE Robotics and Automation Letters*, vol. 7, no. 4, pp. 8831–8836, 2022.

[61] N. Ebrahimi, C. Bi, D. Cappelleri, G. Ciuti, A. Conn, D. Faivre, N. Habibi, A. Hošovský, and V. Iacovacci, "Magnetic actuation methods in bio/soft robotics," *Advanced Functional Materials*, vol. 31, no. 11, pp. 1–40, 2020.

[62] B. McIvor and J. Chahl, "Energy efficiency of linear electromagnetic actuators for flapping wing micro aerial vehicles," *Energies*, vol. 13, no. 5, p. 1075, 2020.

[63] L. Shizhou, W. Chuchao, L. Ansheng, L. Yu, G. Gan, G. Jun, C. Zhen, and L. Xiaohan, "Dynamic and steady-state performance analysis of a linear solenoid parallel elastic actuator with nonlinear stiffness," *Nonlinear Dynamics*, vol. 111, no. 23, pp. 21 507–21 534, 2023.

[64] C. R. Underhill, *Solenoids, electromagnets and electromagnetic windings*. D. Van Nostrand Company, 1914.

[65] F. Chen and M. Y. Wang, "Design optimization of soft robots: A review of the state of the art," *IEEE Robotics and Automation Magazine*, vol. 27, no. 4, pp. 27–43, 2020.

[66] I. Yatchev, V. Gueorgiev, R. Ivanov, and K. Hinov, "Simulation of the dynamic behaviour of a permanent magnet linear actuator," *Facta universitatis-series: Electronics and Energetics*, vol. 23, no. 1, pp. 37–43, 2010.

[67] J. Dai, J. Xia, C. Wang, and S. Xu, "Thermal analysis of an electromagnetic linear actuator," *Advances in Mechanical Engineering*, vol. 9, no. 12, p. 201–213, 2017.

[68] C. Qu, Yong-Chen, P. L. Xu, Z.-R. Xia, and Q.-Y. Xin, "A study on electromagnetic field and force for magnetic micro-robots applications," *Progress In Electromagnetics Research*, vol. 97, p. 201–213, 2020.

[69] Cloom. Chassis wiring: The sensible solution to all your automotive wiring needs. Mechanical Engineering Department, University of Texas at San Antonio. [Online]. Available: https://www.wiringo.com/chassis-wiring.html

[70] L. Metrics. (2023) Copper wire resistance calculator + wire resistance chart (4/0 to 40 awg). LearnMetric. [Online]. Available: https://learnmetrics.com/wire-resistance-calculator-formula/

[71] N. Ebrahimi, P. Schimpf, and A. Jafari, "Design optimization of a solenoid-based electromagnetic soft actuator with permanent magnet core," *Sensors and Actuators A: Physical*, vol. 284, pp. 276–285, 2018.

[72] C. Marchio. (2045) Neodymium magnets vs ferrite magnets. Standford Magnets. [Online]. Available: https://www.stanfordmagnets.com/neodymium-magnets-vs-ferrite-magnets.html

[73] A. Yadav, "Effect of temperature on electric current, magnets and electromagnet," *International Journal of Advancements in Technology*, vol. 7, pp. 1–4, 2016.

[74] H. Choi, K. Cha, J. Choi, S. Jeong, S. Jeon, G. Jang, J. oh Park, and S. Park, "Ema system with gradient and uniform saddle coils for 3d locomotion of microrobot," *Sensors and Actuators A: Physical*, vol. 163, no. 1, pp. 410–417, 2010. [Online]. Available: https://www.sciencedirect.com/science/article/pii/S0924424710003729

[75] T. Xu, J. Yu, X. Yan, H. Choi, and L. Zhang, "Magnetic actuation based motion control for microrobots: An overview," *Micromachines*, vol. 6, no. 9, pp. 1346–1364, 2015. [Online]. Available: https://www.mdpi.com/2072-666X/6/9/1346

[76] R. Chen and D. Folio, "Electromagnetic actuation microrobotic systems," *Current Robotics Reports*, vol. 3, 08 2022.

[77] Z. Yang and L. Zhang, "Magnetic actuation systems for miniature robots: A review," *Advanced Intelligent Systems*, vol. 2, no. 9, p. 2000082, 2020. [Online]. Available: https://onlinelibrary.wiley.com/doi/abs/10.1002/aisy.202000082

[78] S. Salmanipour and E. Diller, "Eight-degrees-of-freedom remote actuation of small magnetic mechanisms," in *2018 IEEE International Conference on Robotics and Automation (ICRA)*, 2018, pp. 3608–3613.

[79] W. Zehao, Z. Yuting, C. Ziqiang, and X. Qingsong, "Design and development of a new rotating electromagnetic field generation system for driving microrobots," *IEEE Transactions on Magnetics*, vol. 58, no. 1, pp. 1–8, 2022.

[80] S. Yuan, Y. Wan, and S. Song, "Rectmag3d: A magnetic actuation system for steering milli/microrobots based on rectangular electromagnetic coils," *Applied Sciences*, vol. 10, no. 8, 2020. [Online]. Available: https://www.mdpi.com/2076-3417/10/8/2677

[81] H. Sun and S. S. Cheng, "A cylindrical halbach array magnetic actuation system for longitudinal robot actuation across 2d workplane," *IEEE Robotics and Automation Letters*, vol. 9, no. 6, pp. 5847–5854, 2024.

[82] K. Cha, S. Jeong, J. Choi, L. Qin, J. Li, J.-O. Park, and S. Park, "Electromagnetic actuation methods for intravascular locomotive microrobot," *Conference proceedings : ... Annual International Conference of the IEEE Engineering in Medicine and Biology Society. IEEE Engineering in Medicine and Biology Society. Conference*, vol. 2010, pp. 1962–5, 08 2010.

[83] M. P. Kummer, J. J. Abbott, B. E. Kratochvil, R. Borer, A. Sengul, and B. J. Nelson, "Octomag: An electromagnetic system for 5-dof wireless micromanipulation," *IEEE Transactions on Robotics*, vol. 26, no. 6, pp. 1006–1017, 2010.

[84] H. Choi, J. Choi, S. Jeong, C. Yu, J. oh Park, and S. Park, "Two-dimensional locomotion of a microrobot with a novel stationary electromagnetic actuation system," *Smart Materials and Structures*, vol. 18, no. 11, p. 115017, sep 2009. [Online]. Available: https://dx.doi.org/10.1088/0964-1726/18/11/115017

[85] B. H. Shin, S.-W. Choi, Y.-B. Bang, and S.-Y. Lee, "An earthworm-like actuator using segmented solenoids," *Smart Materials and Structures*, vol. 20, no. 10, p. 105020, aug 2011. [Online]. Available: https://dx.doi.org/10.1088/0964-1726/20/10/105020

[86] J. Alonso, A. Soleilhavoup, A. Wong, A. Guiga, and D. Sakellariou, "Double helix dipole design applied to magnetic resonance: A novel nmr coil," *Journal of Magnetic Resonance*, vol. 235, pp. 32–41, 2013. [Online]. Available: https://www.sciencedirect.com/science/article/pii/S1090780713001730

[87] A. Dominguez, Gonzalo, K. Mitsuhiro, and S. Shigeki, "Proposal and preliminary feasibility study of a novel toroidal magnetorheological piston," *IEEE/ASME Transactions on Mechatronics*, vol. 22, no. 2, pp. 657–668, 2017.

[88] E. Perez-Guagnelli, J. Jones, and D. D. Damian, "Hyperelastic membrane actuators: Analysis of toroidal and helical multifunctional configurations," *Cyborg and Bionic Systems*, vol. 2022, 2022. [Online]. Available: https://spj.science.org/doi/abs/10.34133/2022/9786864

[89] T. N. Do, H. Phan, T.-Q. Nguyen, and Y. Visell, "Miniature soft electromagnetic actuators for robotic applications," *Advanced Functional Materials*, vol. 28, no. 18, p. 1800244, 2018. [Online]. Available: https://onlinelibrary.wiley.com/doi/abs/10.1002/adfm.201800244

[90] F. Carpi, N. Kastelein, M. Talcott, and C. Pappone, "Magnetically controllable gastrointestinal steering of video capsules," *IEEE Transactions on Biomedical Engineering*, vol. 58, no. 2, pp. 231–234, 2011.

[91] R. Chen, D. Folio, and A. Ferreira, "Analysis and comparison of electromagnetic microrobotic platforms for biomedical applications," *Applied Sciences*, vol. 12, no. 1, 2022. [Online]. Available: https://www.mdpi.com/2076-3417/12/1/456

[92] R. Meinke, C. Goodzeit, and M. Ball, "Modulated double-helix quadrupole magnets," *IEEE Transactions on Applied Superconductivity*, vol. 13, no. 2, pp. 1369–1372, 2003.

[93] C. Goodzeit, M. Ball, and R. Meinke, "The double-helix dipole - a novel approach to accelerator magnet design," *IEEE Transactions on Applied Superconductivity*, vol. 13, no. 2, pp. 1365–1368, 2003.

[94] H. Witte, T. Yokoi, S. L. Sheehy, K. Peach, S. Pattalwar, T. Jones, J. Strachan, and N. Bliss, "The advantages and challenges of helical coils for small accelerators—a case study," *IEEE Transactions on Applied Superconductivity*, vol. 22, no. 2, pp. 4 100 110–4 100 110, 2012.

[95] L. Quéval and R. Gottkehaskamp, "Analytical field calculation of modulated double helical coils," *IEEE Transactions on Applied Superconductivity*, vol. 25, no. 6, pp. 1–7, 2015.

[96] C. Goodzeit, R. Meinke, and M. Ball, "A superconducting induction motor using double-helix dipole coils," *IEEE Transactions on Applied Superconductivity*, vol. 13, no. 2, pp. 2235–2238, 2003.

[97] Y. Chen, W. Wu, B. Wu, E. Mei, and Y. Liang, "Design, fabrication, and test of a 2-t superconducting dipole prototype by using tilted solenoids," *IEEE Transactions on Applied Superconductivity*, vol. 29, no. 4, pp. 1–5, 2019.

[98] R. Meinke, J. Lammers, P. Masson, and G. Stelzer, "Direct Double-Helix Magnet Technology," in *Particle Accelerator Conference (PAC 09)*, 2010, p. MO6PFP041.

[99] O. Ulucay, "Design and control of stewart platform," Aug 2018. [Online]. Available: https://acikbilim.yok.gov.tr/handle/20.500.12812/217788

[100] S.-H. Lee, J.-B. Song, W.-C. Choi, and D. Hong, "Position control of a stewart platform using inverse dynamics control with approximate dynamics," *Mechatronics*, vol. 13, no. 6, pp. 605–619, 2003. [Online]. Available: https://www.sciencedirect.com/science/article/pii/S0957415802000338

[101] Z. Bingul and O. Karahan, *Dynamic Modeling and Simulation of Stewart Platform*, 03 2012.

[102] B. Beach, W. Chapin, S. Chapin, R. Hildebrand, and E. Komendera, "Force-controlled pose optimization and trajectory planning for chained stewart platforms," *Frontiers in Mechanical Engineering*, vol. 9, 2023. [Online]. Available: https://www.frontiersin.org/journals/mechanical-engineering/articles/10.3389/fmech.2023.1225828

[103] W. Min, H. Yingyi, S. Yi, D. Jiheng, P. Huayan, Y. Shujin, Z. Jinglei, P. Yan, X. Shaorong, and L. Jun, "An adjustable low-frequency vibration isolation stewart platform based on electro-

magnetic negative stiffness," *International Journal of Mechanical Sciences*, vol. 181, p. 105714, 2020.

[104] J. Jiao, Y. Wu, K. Yu, and R. Zhao, "Dynamic modeling and experimental analyses of stewart platform with flexible hinges," *Journal of Vibration and Control*, vol. 25, no. 1, pp. 151–171, 2019.

[105] Z. He, X. Feng, Y. Zhu, Z. Yu, Z. Li, Y. Zhang, Y. Wang, P. Wang, and L. Zhao, "Progress of stewart vibration platform in aerospace micro–vibration control," *Aerospace*, vol. 9, no. 6, 2022. [Online]. Available: https://www.mdpi.com/2226-4310/9/6/324

[106] T. Peterson, "Design and implementation of stewart platform robot for robotics course laboratory," p. 14, 03 2020.

[107] H. Hulin, M. Ceccarelli, Z. Weimin, H. Qiang, Y. Zhangguo, and C. Xuechao, "Biomimetic inspiration for pkm torso design in humanoid robots," in *2015 IEEE International Conference on Mechatronics and Automation (ICMA)*, 2015, pp. 1138–1143.

[108] D. Thayer, M. Campbell, J. Vagners, and A. von Flotow, "Six-axis vibration isolation system using soft actuators and multiple sensors," *Journal of Spacecraft and Rockets*, vol. 39, no. 2, pp. 206–212, 2002.

[109] C. Wang, X. Xie, Y. Chen, and Z. Zhang, "Active vibration isolation through a stewart platform with piezoelectric actuators," *Journal of Physics: Conference Series*, vol. 744, no. 1, p. 012006, sep 2016. [Online]. Available: https://dx.doi.org/10.1088/1742-6596/744/1/012006

[110] J. H. Machiani, M. T. Masouleh, A. Kalhor, M. G. Tabrizi, and F. Sanie, "Control of a pneumatically actuated 6-dof gough-stewart platform," in *2014 Second RSI/ISM International Conference on Robotics and Mechatronics (ICRoM)*, 2014, pp. 166–171.

[111] S. D. Mahapatra, D. Saha, R. Saha, D. Sanyal, D. Lahiri, and J. P. Singh, "Analysis of 6-dof motion with pi controller in electrohydraulic stewart platform," *2016 IEEE First International Conference on Control, Measurement and Instrumentation (CMI)*, pp. 186–190, 2016. [Online]. Available: https://api.semanticscholar.org/CorpusID:38987520

[112] X. Fan, J. Ma, and R. Ji, "Integrated dynamic modeling for a stewart platform," in *2018 37th Chinese Control Conference (CCC)*, 2018, pp. 1844–1848.

[113] K. Harib and K. Srinivasan, "Kinematic and dynamic analysis of stewart platform-based machine tool structures," *Robotica*, vol. 21, pp. 541–554, 09 2003.

# Appendix A

# Appendix: Matlab Code

Figure A.1: Platform Dynamics Matlab Code

```
% Relationship between the force, angle of rotation and degree of tilt and
% the vertical and horisontal displacmeent of the plunger
% parameters
F = 1.5;          % Force in N
m = 0.051;        % Mass
r = 0.07;         % Magnet Radius
d = 0.048;        % Maximum displacement
g = 9.81;         % Acceleration due to gravity
mp = 0.057;       % Mass of the top plate (kg)
I = 1/2 * mp * r^2;  % Moment of inertia of the top plate
theta_deg = 15:5:75;  % Angle of inclination from 15 to 75 degrees

% Convert angle from degrees to radians
theta_rad = deg2rad(theta_deg);

% Initialize arrays for time, x-displacement, y-displacement, and angular displacement
t = zeros(size(theta_rad));
x_displacement = zeros(size(theta_rad));
y_displacement = zeros(size(theta_rad));
theta_matrix = zeros(size(theta_rad));  % Angular displacement in radians
tilt_matrix = zeros(size(theta_rad));

% Calculate the time, x and y displacements, and angular displacement for each angle of inclination
for i = 1:length(theta_rad)
    % Calculate the gravitational force component along the slope
    F_gravity = m * g * sin(theta_rad(i));

    % Calculate the net force acting on the block
    F_net = F - F_gravity;

    % Calculate acceleration (a = F_net / m)
    a = F_net / m;

    % Calculate time using the kinematic equation
    t(i) = sqrt(2 * d / a);

    % Calculate x and y displacement
    x_displacement(i) = d * cos(theta_rad(i));
    y_displacement(i) = d * sin(theta_rad(i));

    % Calculate the torque due to the pulling force
    tau = F * r * cos(theta_rad(i));  % Use theta_rad for angle of inclination

    % Calculate angular acceleration
    alpha_angular = tau / I;

    % Calculate the angular displacement (theta) in radians
    theta_matrix(i) = 0.5 * alpha_angular * t(i)^2;  % Angular displacement formula: theta = 0.5 * alpha * t^2

    tilt_matrix(i) = atan(y_displacement(i)/(0.08))*(180/pi);
end

% Convert angular displacement from radians to degrees
theta_matrix_deg = rad2deg(theta_matrix);

theta_deg_rounded = round(theta_deg, 3);
t_rounded = round(t, 3);
x_displacement_rounded = round(x_displacement, 3);
y_displacement_rounded = round(y_displacement, 3);
theta_matrix_deg_rounded = round(theta_matrix_deg, 3);
tilt_matrix_rounded = round(tilt_matrix, 2);

% Create the table with rounded values
results_table = table(theta_deg_rounded', t_rounded', x_displacement_rounded', y_displacement_rounded', theta_matrix_deg_rounded', tilt_ma
    'VariableNames', {'Angle_Degrees', 'Time_Seconds', 'X_Displacement_m', 'Y_Displacement_m', 'Theta_Degrees','Tilt'});
% Create a table with the results
% results_table = table(theta_deg', t', x_displacement', y_displacement', theta_matrix_deg', tilt_matrix', ...
%     'VariableNames', {'Angle_Degrees', 'Time_Seconds', 'X_Displacement_m', 'Y_Displacement_m', 'Theta_Degrees','Tilt'});

% Display the table
disp(results_table);
figure;
subplot(2,1,1)

hold on;  % Hold on to plot multiple lines on the same graph

% Loop through each tilt angle and plot the displacement over time
for i = 1:length(theta_deg)
    % Time vector up to the time it takes to reach max displacement
    time_vector = linspace(0, t(i), 100);
```

```
    % Calculate the displacement for this specific angle
    displacement_x = (0.5*(F - m * g * sin(theta_rad(i)))/m)*cos(theta_rad(i))*time_vector.^2;
    displacement_y = (0.5*(F - m * g * sin(theta_rad(i)))/m)*sin(theta_rad(i))*time_vector.^2;
    % Plateau the displacement after the time t(i)
    displacement_x(time_vector > t(i)) = x_displacement(i);

    % Plot the displacement
    plot(time_vector, displacement_x, 'LineWidth', 2);

end

% Add title, labels, and legend

xlabel('Time (s)');
ylabel('Horizontal Displacement (m)');
legend_entries = arrayfun(@(a) sprintf('\\phi = %.2f°', a), theta_deg, 'UniformOutput', false);
legend(legend_entries);
grid on;
hold off;

subplot(2,1,2)
  % Hold on to plot multiple lines on the same graphs
% Loop through each tilt angle and plot the displacement over time
for i = 1:length(theta_deg)
    % Time vector up to the time it takes to reach max displacement
    time_vector = linspace(0, t(i), 100);

    % Calculate the displacement for this specific angle
    displacement_x = (0.5*(F - m * g * sin(theta_rad(i)))/m)*cos(theta_rad(i))*time_vector.^2;
    displacement_y = (0.5*(F - m * g * sin(theta_rad(i)))/m)*sin(theta_rad(i))*time_vector.^2;
    % Plateau the displacement after the time t(i)
    displacement_x(time_vector > t(i)) = x_displacement(i);

    % Plot the displacement
    plot(time_vector, displacement_y, 'LineWidth', 2);
    hold on;

end

% Add title, labels, and legend

xlabel('Time (s)');
ylabel('Vertical Displacement (m)');
legend_entries = arrayfun(@(a) sprintf('\\phi = %.2f°', a), theta_deg, 'UniformOutput', false);
legend(legend_entries);
grid on;
hold off;
```

The movement of the platform is controlled by an Arduino by exciting individual solenoids through an H-Bridge DC motor driver.

# Appendix B

# Appendix: AWG Table

The wire diameters and correlating currents in Chapter 5 are according to the American Wire Gauge (AWG) Table in Figure.

**Table 1: American Wire Gauge (AWG) Cable / Conductor Sizes and Properties**

| AWG | Diameter [inches] | Diameter [mm] | Area [$mm^2$] | Resistance [Ohms / 1000 ft] | Resistance [Ohms / km] | Max Current [Amperes] | Max Frequency for 100% skin depth |
|---|---|---|---|---|---|---|---|
| 0000 (4/0) | 0.46 | 11.684 | 107 | 0.049 | 0.16072 | 302 | 125 Hz |
| 000 (3/0) | 0.4096 | 10.40384 | 85 | 0.0618 | 0.202704 | 239 | 160 Hz |
| 00 (2/0) | 0.3648 | 9.26592 | 67.4 | 0.0779 | 0.255512 | 190 | 200 Hz |
| 0 (1/0) | 0.3249 | 8.25246 | 53.5 | 0.0983 | 0.322424 | 150 | 250 Hz |
| 1 | 0.2893 | 7.34822 | 42.4 | 0.1239 | 0.406392 | 119 | 325 Hz |
| 2 | 0.2576 | 6.54304 | 33.6 | 0.1563 | 0.512664 | 94 | 410 Hz |
| 3 | 0.2294 | 5.82676 | 26.7 | 0.197 | 0.64616 | 75 | 500 Hz |
| 4 | 0.2043 | 5.18922 | 21.2 | 0.2485 | 0.81508 | 60 | 650 Hz |
| 5 | 0.1819 | 4.62026 | 16.8 | 0.3133 | 1.027624 | 47 | 810 Hz |
| 6 | 0.162 | 4.1148 | 13.3 | 0.3951 | 1.295928 | 37 | 1100 Hz |
| 7 | 0.1443 | 3.66522 | 10.5 | 0.4982 | 1.634096 | 30 | 1300 Hz |
| 8 | 0.1285 | 3.2639 | 8.37 | 0.6282 | 2.060496 | 24 | 1650 Hz |
| 9 | 0.1144 | 2.90576 | 6.63 | 0.7921 | 2.598088 | 19 | 2050 Hz |
| 10 | 0.1019 | 2.58826 | 5.26 | 0.9989 | 3.276392 | 15 | 2600 Hz |
| 11 | 0.0907 | 2.30378 | 4.17 | 1.26 | 4.1328 | 12 | 3200 Hz |
| 12 | 0.0808 | 2.05232 | 3.31 | 1.588 | 5.20864 | 9.3 | 4150 Hz |
| 13 | 0.072 | 1.8288 | 2.62 | 2.003 | 6.56984 | 7.4 | 5300 Hz |
| 14 | 0.0641 | 1.62814 | 2.08 | 2.525 | 8.282 | 5.9 | 6700 Hz |
| 15 | 0.0571 | 1.45034 | 1.65 | 3.184 | 10.44352 | 4.7 | 8250 Hz |
| 16 | 0.0508 | 1.29032 | 1.31 | 4.016 | 13.17248 | 3.7 | 11 k Hz |
| 17 | 0.0453 | 1.15062 | 1.04 | 5.064 | 16.60992 | 2.9 | 13 k Hz |
| 18 | 0.0403 | 1.02362 | 0.823 | 6.385 | 20.9428 | 2.3 | 17 kHz |
| 19 | 0.0359 | 0.91186 | 0.653 | 8.051 | 26.40728 | 1.8 | 21 kHz |
| 20 | 0.032 | 0.8128 | 0.518 | 10.15 | 33.292 | 1.5 | 27 kHz |
| 21 | 0.0285 | 0.7239 | 0.41 | 12.8 | 41.984 | 1.2 | 33 kHz |
| 22 | 0.0254 | 0.64516 | 0.326 | 16.14 | 52.9392 | 0.92 | 42 kHz |
| 23 | 0.0226 | 0.57404 | 0.258 | 20.36 | 66.7808 | 0.729 | 53 kHz |
| 24 | 0.0201 | 0.51054 | 0.205 | 25.67 | 84.1976 | 0.577 | 68 kHz |
| 25 | 0.0179 | 0.45466 | 0.162 | 32.37 | 106.1736 | 0.457 | 85 kHz |
| 26 | 0.0159 | 0.40386 | 0.129 | 40.81 | 133.8568 | 0.361 | 107 kHz |
| 27 | 0.0142 | 0.36068 | 0.102 | 51.47 | 168.8216 | 0.288 | 130 kHz |
| 28 | 0.0126 | 0.32004 | 0.081 | 64.9 | 212.872 | 0.226 | 170 kHz |
| 29 | 0.0113 | 0.28702 | 0.0642 | 81.83 | 268.4024 | 0.182 | 210 kHz |
| 30 | 0.01 | 0.254 | 0.0509 | 103.2 | 338.496 | 0.142 | 270 kHz |
| 31 | 0.0089 | 0.22606 | 0.0404 | 130.1 | 426.728 | 0.113 | 340 kHz |
| 32 | 0.008 | 0.2032 | 0.032 | 164.1 | 538.248 | 0.091 | 430 kHz |
| 33 | 0.0071 | 0.18034 | 0.0254 | 206.9 | 678.632 | 0.072 | 540 kHz |
| 34 | 0.0063 | 0.16002 | 0.0201 | 260.9 | 855.752 | 0.056 | 690 kHz |
| 35 | 0.0056 | 0.14224 | 0.016 | 329 | 1079.12 | 0.044 | 870 kHz |
| 36 | 0.005 | 0.127 | 0.0127 | 414.8 | 1360 | 0.035 | 1100 kHz |
| 37 | 0.0045 | 0.1143 | 0.01 | 523.1 | 1715 | 0.0289 | 1350 kHz |
| 38 | 0.004 | 0.1016 | 0.00797 | 659.6 | 2163 | 0.0228 | 1750 kHz |
| 39 | 0.0035 | 0.0889 | 0.00632 | 831.8 | 2728 | 0.0175 | 2250 kHz |
| 40 | 0.0031 | 0.07874 | 0.00501 | 1049 | 3440 | 0.0137 | 2900 kHz |

Figure B.1: AWG Table

# Appendix C

# Appendix: Arduino Code for Platform Movement

(a) Arduino Code for Various Platfrom Movements

```
// Define the motor control pins
int motorPin12 = 12; // Connect to the H-bridge input pin 1 (e.g., IN1)
int motorPin11 = 11;
int motorPin10 = 10;
int motorPin9 = 9;
int motorPin8 = 8;
int motorPin7 = 7;
int motorPin6 = 6;
int motorPin5 = 5;
int motorPin4 = 4;
int motorPin3 = 3;
int motorPin2 = 2;
int motorPin1 = 13;
// Variable to store the command from the Serial Monitor
String command = "";
void setup() {
  // Set the motor control pins as outputs
  pinMode(motorPin12, OUTPUT);
  pinMode(motorPin11, OUTPUT);
  pinMode(motorPin10, OUTPUT);
  pinMode(motorPin9, OUTPUT);
  pinMode(motorPin8, OUTPUT);
  pinMode(motorPin7, OUTPUT);
  pinMode(motorPin6, OUTPUT);
  pinMode(motorPin5, OUTPUT);
  pinMode(motorPin4, OUTPUT);
  pinMode(motorPin3, OUTPUT);
  pinMode(motorPin2, OUTPUT);
  pinMode(motorPin1, OUTPUT);
  // Initialize Serial communication
  Serial.begin(9600);
  Serial.println("Enter command: forward, backward, or stop");
}
```

```
void loop() {

  if (Serial.available() > 0) {

    command = Serial.readStringUntil('\n');
    command.trim();
    // Execute the command based on the input
    if (command == "F") {
      forward();
      Serial.println("Moving forward...");

    } else if (command == "B") {
      backward();
      Serial.println("Moving backward...");

    } else if (command == "END") {
      stopMotor();
      Serial.println("stop");

    } else if (command == "CW") {
      CW();

      Serial.println("CW");

     } else if (command == "CCW") {
      CCW();


      Serial.println("CCW");

     } else if (command == "A") {
      A();
      Serial.println("A Up");



     } else if (command == "b") {
      B();
      Serial.println("B Up");

     } else if (command == "C") {
      C();
      Serial.println("C Up");

    } else if (command == "dance") {
      Serial.println("Dancing");
      backward();
      delay(500); // Keep moving for 3 seconds
      stopMotor(); // Stop after 3 seconds
      forward();
      Serial.println("Forward");
      delay(4000);
      backward();
      Serial.println("Backward");
      delay(2000);
      stopMotor();
      CCW();
      Serial.println("CCW");
      delay(4000);
      CCWb();
      delay(1000);
      backward();
      Serial.println("backward");
      delay(2000);
      stopMotor();
      CW();
      Serial.println("CW");
```

```
      delay(4000);
      CWb();
      delay(1000);
      backward();
      Serial.println("backward");
      delay(2000);
      stopMotor();
      A();
      Serial.println("A");
      delay(4000);
      backward();
      Serial.println("backward");
      delay(2000);
      stopMotor();
      B();
      Serial.println("B");
      delay(4000);
      backward();
      Serial.println("backward");
      delay(2000);
      stopMotor();
      C();
      Serial.println("C");
      delay(4000);
      backward();
      Serial.println("backward");
      delay(2000);
      stopMotor();
      A();
      Serial.println("A");
      delay(3000);
      C();
      Serial.println("B");
      delay(3000);
      B();
      Serial.println("C");
      delay(3000);


      backward();
      stopMotor();
    } else {
      Serial.println("Invalid command. Please enter: forward, backward, or stop");
    }
  }
}
// Function to move the motor forward
void forward() {
  digitalWrite(motorPin12, HIGH);
  digitalWrite(motorPin11, LOW);
  digitalWrite(motorPin10, HIGH);
  digitalWrite(motorPin9, LOW);
  digitalWrite(motorPin8, HIGH);
  digitalWrite(motorPin7, LOW);
  digitalWrite(motorPin6, HIGH);
  digitalWrite(motorPin5, LOW);
  digitalWrite(motorPin4, HIGH);
  digitalWrite(motorPin3, LOW);
  digitalWrite(motorPin2, HIGH);
  digitalWrite(motorPin1, LOW);
}


// Function to move the motor backward
void backward() {
  digitalWrite(motorPin12, LOW);
  digitalWrite(motorPin11, HIGH);
  digitalWrite(motorPin10, LOW);
  digitalWrite(motorPin9, HIGH);
  digitalWrite(motorPin8, LOW);
  digitalWrite(motorPin7, HIGH);
  digitalWrite(motorPin6, LOW);
  digitalWrite(motorPin5, HIGH);
  digitalWrite(motorPin4, LOW);
  digitalWrite(motorPin3, HIGH);
  digitalWrite(motorPin2, LOW);
  digitalWrite(motorPin1, HIGH);
}
// Function to stop the motor
void stopMotor() {
  digitalWrite(motorPin12, LOW);
  digitalWrite(motorPin11, LOW);
  digitalWrite(motorPin10, LOW);
  digitalWrite(motorPin9, LOW);
  digitalWrite(motorPin8, LOW);
  digitalWrite(motorPin7, LOW);
  digitalWrite(motorPin6, LOW);
  digitalWrite(motorPin5, LOW);
  digitalWrite(motorPin4, LOW);
  digitalWrite(motorPin3, LOW);
  digitalWrite(motorPin2, LOW);
  digitalWrite(motorPin1, LOW);
}
```

```
void CW() {
  //digitalWrite(motorPin12, HIGH);
  //digitalWrite(motorPin11, LOW);
  digitalWrite(motorPin10, HIGH);
  digitalWrite(motorPin9, LOW);
  //digitalWrite(motorPin8, HIGH);
  //digitalWrite(motorPin7, LOW);
  digitalWrite(motorPin6, HIGH);
  digitalWrite(motorPin5, LOW);
  digitalWrite(motorPin4, HIGH);
  digitalWrite(motorPin3, LOW);
  //digitalWrite(motorPin2, HIGH);
  //digitalWrite(motorPin1, LOW);
}
void CWb() {
  //digitalWrite(motorPin12, HIGH);
```

```
  //digitalWrite(motorPin11, LOW);
  digitalWrite(motorPin10, LOW);
  digitalWrite(motorPin9, HIGH);
  //digitalWrite(motorPin8, HIGH);
  //digitalWrite(motorPin7, LOW);
  digitalWrite(motorPin6, LOW);
  digitalWrite(motorPin5, HIGH);
  digitalWrite(motorPin4, LOW);
  digitalWrite(motorPin3, HIGH);
  //digitalWrite(motorPin2, HIGH);
  //digitalWrite(motorPin1, LOW);
}
void CCW() {
  digitalWrite(motorPin12, HIGH);
  digitalWrite(motorPin11, LOW);
  //digitalWrite(motorPin10, HIGH);
  //digitalWrite(motorPin9, LOW);
  digitalWrite(motorPin8, HIGH);
  digitalWrite(motorPin7, LOW);
  //digitalWrite(motorPin6, HIGH);
  //digitalWrite(motorPin5, LOW);
  //digitalWrite(motorPin4, HIGH);
  //digitalWrite(motorPin3, LOW);
  digitalWrite(motorPin2, HIGH);
  digitalWrite(motorPin1, LOW);
}
```

```
void CCWb() {
  digitalWrite(motorPin12, LOW);
  digitalWrite(motorPin11, HIGH);
  //digitalWrite(motorPin10, HIGH);
  //digitalWrite(motorPin9, LOW);
  digitalWrite(motorPin8, LOW);
  digitalWrite(motorPin7, HIGH);
  //digitalWrite(motorPin6, HIGH);
  //digitalWrite(motorPin5, LOW);
  //digitalWrite(motorPin4, HIGH);
  //digitalWrite(motorPin3, LOW);
  digitalWrite(motorPin2, LOW);
  digitalWrite(motorPin1, HIGH);
}
void A() {
  //digitalWrite(motorPin12, LOW);
  //digitalWrite(motorPin11, HIGH);
  //digitalWrite(motorPin10, LOW);
  //digitalWrite(motorPin9, HIGH);
  //digitalWrite(motorPin8, LOW);
  //digitalWrite(motorPin7, HIGH);
  digitalWrite(motorPin6, HIGH);
  digitalWrite(motorPin5, LOW);
  //digitalWrite(motorPin4, LOW);
  //digitalWrite(motorPin3, HIGH);
  digitalWrite(motorPin2, HIGH);
  digitalWrite(motorPin1, LOW);
}
```

```
void B() {
  digitalWrite(motorPin12, HIGH);
  digitalWrite(motorPin11, LOW);
 // digitalWrite(motorPin10, LOW);
  //digitalWrite(motorPin9, HIGH);
  //digitalWrite(motorPin8, LOW);
  //digitalWrite(motorPin7, HIGH);
  //digitalWrite(motorPin6, LOW);
  //digitalWrite(motorPin5, HIGH);
  digitalWrite(motorPin4, HIGH);
  digitalWrite(motorPin3, LOW);
  //digitalWrite(motorPin2, LOW);
  //digitalWrite(motorPin1, HIGH);
}
```

```
void C() {
 // digitalWrite(motorPin12, LOW);
 // digitalWrite(motorPin11, HIGH);
  digitalWrite(motorPin10, HIGH);
  digitalWrite(motorPin9, LOW);
  digitalWrite(motorPin8, HIGH);
  digitalWrite(motorPin7, LOW);
 // digitalWrite(motorPin6, LOW);
 // digitalWrite(motorPin5, HIGH);
 // digitalWrite(motorPin4, LOW);
 // digitalWrite(motorPin3, HIGH);
 // digitalWrite(motorPin2, LOW);
 // digitalWrite(motorPin1, HIGH);
}
```

# Appendix D

# Appendix: Inverse Dynamic Modelling of 6 DOF parallel actuator

The inverse dynamic method is used to investigate the dynamic behaviour of the 6-legged parallel manipulator [5]. A substructure technique is used to create the differential-algebraic system of equations that describes the platform's motion [113] [5]. The following dynamic analysis divided the parallel structure into substructures for kinematic and dynamic analysis with the original derivation from Truan Xuan Tien [5]. The full version of the equations can be found in 'Solution of Inverse Dynamics of Stewart-Gough Platfrom Using Substructure Technique' [5].

The parallel manipular is a Stewart-Gough platform which includes a circular platform connected to a fixed base using six limbs [5].$A_i, B_i (i = 1, 2, 3, ....6)$. Each limb is made up of a solenoid cylinder and a magnet plunger. The solenoid cylinder of each leg is connected to the fixed base by a universal joint at $A_i$. Similarly, a universal joint connects the magnetic piston to the moving platform,$B_i$. Each leg is driven by the electromagnetic force. The global coordinate system is described at $(0, x_0, y_0, z_0)$ attached to the fixed base, and the local coordinate system $(P, u, v, w)$ is attached to the moving platform. $d_i$ is the length of each leg, and $a_i$ is the distance from the center of universal joint $A_i$ to the center of the fixed base platform 0, and $b_i$ the distance from the universal joint $B_i$ to the center of the moving platform $P$. The mass of the solenoid cylinder and magnet piston of each leg are $m1$, and $m2$ respectively [5].

The position of the moving platform described in the global coordinate system is vector $r_p = \overrightarrow{OP}$, with algebraic vecotr, $\mathbf{r}\overset{(0)}{p} = \begin{bmatrix} x_P \\ y_P \\ z_P \end{bmatrix}^T$. The orientation of the moving platform is defined by the orientation of the local coordinate system in the global coordinate system and is described by the roll-pitch-yaw angles $(\varphi_x, \varphi_y, \varphi_z)$, and can be expressed by a rotational transform matrix $A_P$ [113] [5].

$$A_P = \begin{bmatrix} c_{\varphi_z} c_{\varphi_y} & -s_{\varphi_z} c_{\varphi_x} + c_{\varphi_z} s_{\varphi_y} s_{\varphi_x} & s_{\varphi_z} s_{\varphi_x} + c_{\varphi_z} s_{\varphi_y} c_{\varphi_x} \\ \varphi_z c_{\varphi_y} & c_{\varphi_z} c_{\varphi_x} + s_{\varphi_z} s_{\varphi_y} s_{\varphi_x} & -c_{\varphi_z} s_{\varphi_x} + s_{\varphi_z} s_{\varphi_y} c_{\varphi_x} \\ -s_{\varphi_y} & c_{\varphi_y} s_{\varphi_x} & c_{\varphi_y} c_{\varphi_x} \end{bmatrix} \tag{D.1}$$

Where, $c_{\varphi_i} = cos(\varphi_i), s_{\varphi_i} = sin(\varphi_i), i = x, y, z$. In the local coordinate systems the position of the universal joint $B_i$ is determined by the vector $\mathbf{b}_i = \overrightarrow{PB_i}, b_i{}^{(P)} = \begin{bmatrix} b_i u \\ b_i v \\ b_i w \end{bmatrix}^T$

The $i-th$ leg is represented by the local coordinate system $A_i, x_i, y_i, z_i$, and its orientation with respect to the base can be described by two Euler angles $\varphi_i, \vartheta_i$, where the leg can undergo a rotation $\varphi_i$ about the axis $Z_i$, and rotation $\vartheta_i$ about the axis $y_i$. Therefore, the rotation matrix of the $i-th$ limb is given by

$$A_i = \begin{bmatrix} c_{\varphi_i} c_{\theta_i} & -s_{\varphi_i} & c_{\varphi_i} s_{\theta_i} \\ s_{\varphi_i} c_{\theta_i} & c_{\varphi_i} & s_{\varphi_i} s_{\theta_i} \\ -s_{\theta_i} & 0 & c_{\theta_i} \end{bmatrix} \tag{D.2}$$

The position of the universal Joint $A_i$ in the global system can be described as:

$$a_i{}^{(0)} = \begin{bmatrix} a_i x \\ a_i y \\ a_i z \end{bmatrix}^T \tag{D.3}$$

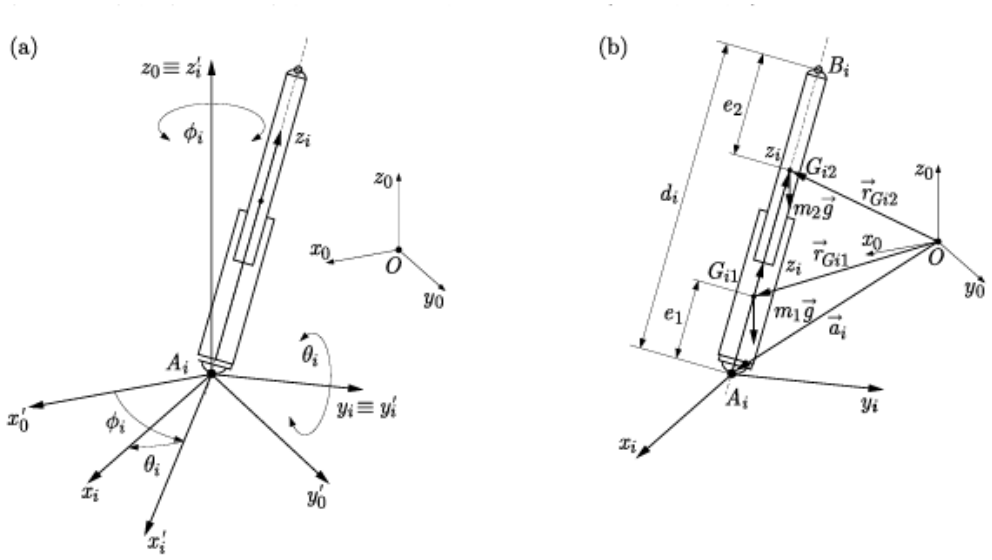


Figure D.1: (a) Two Euler angles of the limb (b) Free body diagram of a typical limb [5]

As illustrated in Figure D.1, the $e_1$ is the distance between $A_i$, and the centre of mass of the $i-th$ cylinder, $G_i1$ while $e_2$ is the distance between $B_i$ and the centre of mass of the $i-th$ piston. The vectors $c_{1i}^{(i)}$, and $c_{2i}^{(i)}$ represent the positions of the center of mass of the $i-th$ cylinder and piston, respectively.

$$c_{1i}^{(i)} = [0, 0, e_1]^T, c_{2i}^{(i)} = [0, 0, d_i - e_2]^T \tag{D.4}$$

Where the centres of mass of the cylinder and piston are $r_{G_{i1}} = a_i + c_{i1}$ and $r_{G_{i2}} = a_i + c_{i2}$. Thus, in the global coordinate system, they are given by the following

$$r_{G_{i1}}^{(0)} = \mathbf{a_i}^{(0)} + A_i c_{i1}^{(i)} = \begin{bmatrix} a_{ix} + c_{\varphi_i} s_{\theta_i} e_1 \\ a_{iy} + s_{\varphi_i} s_{\theta_i} e_1 \\ a_{iz} + c_{\theta_i} e_1 \end{bmatrix}, r_{G_{i2}}^{(0)} = \mathbf{a_i}^{(0)} + A_i c_{i2}^{(i)} = \begin{bmatrix} a_{ix} + c_{\varphi_i} s_{\theta_i} (d_i - e_2) \\ a_{iy} + s_{\varphi_i} s_{\theta_i} (d_i - e_2) \\ a_{iz} + c_{\theta_i} (d_i - e_2) \end{bmatrix} \tag{D.5}$$

The vector for each leg can be concluded,

$$\overrightarrow{OA_i} + \overrightarrow{A_iB_i} = \overrightarrow{OP} + \overrightarrow{PB_i} \Leftrightarrow \overrightarrow{a_i} + \overrightarrow{d_i} = \overrightarrow{r_p} + \overrightarrow{b_i} \tag{D.6}$$

with the corresponding matrix equation,

$$\mathbf{a_i}^{(0)} + A_i d_i^{(i)} = r_P^{(0)} + A_P b_i^{(P)} \tag{D.7}$$

$$\begin{bmatrix} a_{ix} \\ a_{iy} \\ a_{iz} \end{bmatrix} + \begin{bmatrix} c_{\varphi_i} c_{\theta_i} & -s_{\varphi_i} & c_{\varphi_i} s_{\theta_i} \\ s_{\varphi_i} c_{\theta_i} & c_{\varphi_i} & s_{\varphi_i} s_{\theta_i} \\ -s_{\theta_i} & 0 & c_{\theta_i} \end{bmatrix} \begin{bmatrix} 0 \\ 0 \\ d_i \end{bmatrix} = \begin{bmatrix} x_P \\ y_P \\ z_P \end{bmatrix} + A_P \begin{bmatrix} b_{iu} \\ b_{iv} \\ b_{iw} \end{bmatrix}, i = 1, 2, 3, ...6 \tag{D.8}$$

Therefore, the position of the $i-th$ limb can be determined by a vector of generalised coordinates,$q(i) = [\theta_i, \varphi_i, d_i]^T$

Reaction forces $X_{Bi}, Y_{Bi}, Z_{Bi}$ are the reaction forces at the plunger joint $B_i$ on the $i-th$ limb, and $T_i$ is the input force from the actuator [5].

**Motion of Each Limb**

The angular velocity of the solenoid and the plunger is denoted by $w_{i1}$, and $w_{i2}$ respectively,

$$\overset{(i)}{W}i1 = \overset{(i)}{W}i2 = \begin{bmatrix} -s\theta_i \dot{\phi}_i \\ \dot{\theta}_i \\ c\theta_i \dot{\phi}_i \end{bmatrix} \tag{D.9}$$

From D.9 the Jacobian matrices of translation for the solenoid and plunger are given in D.10

$$J_{T1} = \frac{\partial r(0)}{\partial q(i)} = \begin{bmatrix} c\phi_i c\theta_i e_1 & -s\phi_i s\theta_i e_1 & 0 \\ s\phi_i c\theta_i e_1 & c\phi_i s\theta_i e_1 & 0 \\ -s\theta_i e_1 & 0 & 0 \end{bmatrix} \tag{D.10}$$

$$J_{T2} = \frac{\partial r(0)}{\partial q(i)} = \begin{bmatrix} c\phi_i c\theta_i (d_i - e_2) & -s\phi_i s\theta_i (d_i - e_2) & c\phi_i s\theta_i \\ s\phi_i c\theta_i (d_i - e_2) & c\phi_i s\theta_i (d_i - e_2) & s\phi_i s\theta_i \\ -s\theta_i (d_i - e_2) & 0 & c\theta_i \end{bmatrix} \tag{D.11}$$

The moment of inertia for the solenoid and plunger are given by [5],

$$I(i)_{i1} = \begin{bmatrix} I_{x1} & 0 & 0 \\ 0 & I_{y1} & 0 \\ 0 & 0 & I_{z1} \end{bmatrix}, I(i)_{i2} = \begin{bmatrix} I_{x2} & 0 & 0 \\ 0 & I_{y2} & 0 \\ 0 & 0 & I_{z2} \end{bmatrix} \tag{D.12}$$

**Mass Matrix**

where the mass matrix is [5] [113],

$$M(i)(q(i)) = J_{Ti1}^T m_1 J_{Ti1} + J_{Ti2}^T m_2 J_{Ti2} + J_{Ri1}^T I_{Ri1}^{(i)} J_{Ri1}^{(i)} + J_{Ri2}^T I_{Ri2}^{(i)} J_{Ri2}^{(i)} \tag{D.13}$$

resulting in,

$$M(i)(q(i)) = \begin{bmatrix} m(i)_{11} & m(i)_{12} & m(i)_{13} \\ m(i)_{21} & m(i)_{22} & m(i)_{23} \\ m(i)_{31} & m(i)_{32} & m(i)_{33} \end{bmatrix} \tag{D.14}$$

where:
$m(i)_{11} = I_{y1} + I_{y2} + m_1 e_1^2 + m_2 (d_i - e_2)^2$
$m(i)_{22} = \left[I_{x1} + I_{x2} + m_1 e_2^1 + m_2 (d_i - e_2)^2\right] s^2\theta_i + (I_{z1} + I_{z2})\, c^2\theta_i$
$m(i)_{33} = m_2$
$m(i)_{12} = m(i)_{21} = m(i)_{23} = m(i)_{32} = m(i)_{13} = m(i)_{31} = 0$

**Centrifugal and Coriolis Matrices**

The centrifugal and Coriolis matrices are given by [5],

$$(i)(q(i), \dot{q}(i)) = \frac{\partial M(i)(q(i))}{\partial q(i)} \left(I_3 \otimes \dot{q}(i)\right)^{-1} + \frac{1}{2} \frac{\partial M(i)(q(i))}{\partial q(i)} \left(\dot{q}(i) \otimes I_3\right)^T \tag{D.15}$$

and by substituting D.13 into D.15, the matrix is obtained,

$$C(i)(q(i), \dot{q}(i)) = \begin{bmatrix} c(i)_{11} & c(i)_{12} & 0 \\ 0 & c(i)_{22} & 0 \\ c(i)_{31} & c(i)_{32} & 0 \end{bmatrix} \tag{D.16}$$

where, $c(i)_{11} = 2m_2(d_i - e_2)\dot{d}_i$

$c(i)_{12} = -s\theta_i c\theta_i \left[m_1 e_2^1 + m_2 (d_i - e_2)^2 + I_{x1} + I_{x2} - I_{z1} - I_{z2}\right] \dot{\phi}_i$

$c(i)_{22} = 2s\theta_i c\theta_i \left[m_1 e_2^1 + m_2 (d_i - e_2)^2 + I_{x1} + I_{x2} - I_{z1} - I_{z2}\right] \dot{\theta}_i + 2m_2(d_i - e_2) s^2\theta_i \dot{d}_i$

$c(i)_{31} = -m_2(d_i - e_2)\dot{\theta}_i$

$c(i)_{32} = -m_2(d_i - e_2) s^2\theta_i \dot{\phi}_i$

$c(i)_{13} = c(i)_{21} = c(i)_{23} = c(i)_{33} = 0$

**Potential Energy**

The potential energy is then,

$$\Pi(i) = m_1 g \mathrm{Tr}\, G_{i1} + m_2 g \mathrm{Tr}\, G_{i2} = m_1 g (a_{iz} + e_1 c\theta_i) + m_2 g \left[a_{iz} + (d_i - e_2) c\theta_i\right] \quad (2.20) \tag{D.17}$$

$$g(i)(q(i)) = \frac{\partial \Pi(i)}{\partial q(i)}^T = \begin{bmatrix} (-m_1 e_1 - m_2 d_i + m_2 e_2) g s\theta_i \\ 0 \\ m_2 g c\theta_i \end{bmatrix} \tag{D.18}$$

Finally, the position of the joint $B_i$ can be determined through $r_{Bi} = a_i + di$.

$$\mathbf{r(0)}\, B_i = \mathbf{a(0)}_i + A_i d(i)_i = \begin{bmatrix} a_{ix} \\ a_{iy} \\ a_{iz} \end{bmatrix} + \begin{bmatrix} c\phi_i c\theta_i & -s\phi_i & c\phi_i s\theta_i \\ s\phi_i c\theta_i & c\phi_i & s\phi_i s\theta_i \\ -s\theta_i & 0 & c\theta_i \end{bmatrix} \begin{bmatrix} 0 \\ 0 \\ d_i \end{bmatrix} = \begin{bmatrix} a_{ix} + c\phi_i s\theta_i d_i \\ a_{iy} + s\phi_i s\theta_i d_i \\ a_{iz} + c\theta_i d_i \end{bmatrix} \tag{D.19}$$

**Generalised Force**

Based on the principle of virtual work, the virtual work of non-conservative forces is expressed as $\sum \delta A^i_{np} = \tau_i \delta d_i - X_{B_i} \delta x_{B_i} - Y_{B_i} \delta y_{B_i} - Z_{B_i} \delta z_{B_i}$, by substituting the virtual displacement of the joint into the non-conservative force equation, the generalised force corresponding to the conservative force acting on the i-th limb is [5],

$$f^i_{np} = \begin{bmatrix} -d_i c\phi_i c\theta_i X_{B_i} - d_i s\phi_i c\theta_i Y_{B_i} + d_i s\theta_i Z_{B_i} \\ d_i s\phi_i s\theta_i X_{B_i} - d_i c\phi_i s\theta_i Y_{B_i} \\ \tau_i - X_{B_i} c\phi_i s\theta_i - Y_{B_i} s\phi_i s\theta_i - Z_{B_i} c\theta_i \end{bmatrix} \tag{D.20}$$

Therefore, the system of differential equations describing the motion of each limb in the system is given as

$$M(i)(q(i))\ddot{q}(i) + C(i)(q(i), \dot{q}(i))\dot{q}(i) + g(i)(q(i)) = f_{np} \tag{D.21}$$

The inverse dynamic equations are widely available and commonly used in Stewart and Stewart-Gough platforms. The inverse dynamic equations describe the movement of the individual actuator legs and the entire platform. Therefore, this enables the calculation of the required force to meet the reference trajectory. The full version of the equations can be found in 'Solution of Inverse Dynamics of Stewart-Gough Platfrom Using Substructure Technique' [5]. These equations are a variation of the inverse equations used in the MATLAB-Simulink model of the Stewart Platform used in Chapter 6.

# Appendix E

# Ethics Approval


**PRE-SCREENING QUESTIONNAIRE OUTCOME LETTER**

STU-EBE-2024-PSQ001068

2024/08/13

Dear Sigrid Aadnesgaard,

Your Ethics pre-screening questionnaire (PSQ) has been evaluated by your departmental ethics representative. Based on the information supplied in your PSQ, it has been determined that you do not need to make a full ethics application for the research project in question.

You may proceed with your research project titled:

Electromagnetic Spine Robot

Please note that should aspect(s) of your current project change, you should submit a new PSQ in order to determine whether the changed aspects increase the ethical risks of your project. It may be the case that project changes could require a full ethics application and review process.

Regards,

Faculty Research Ethics Committee

# Appendix F

# AI Contributions

AI was used to summarise sources into prompted headings and subheadings. Further, AI condensed personal summaries of papers and articles and organised the summarised information into categories with their correlating references. AI (Grammarly) was also used to aid in the flow and sentence construction of the thesis.